Dipl.-Ing. David Lindenthaler, BSc

Accurate Power Measurements in Electric Drives

Dissertation

zur Erlangung des akademischen Grades

Doktor der technischen Wissenschaften

eingereicht an der

Technischen Universität Graz

Betreuer:

Univ.-Prof. Dipl.-Ing. Dr.techn. Georg Brasseur

Institut für Elektrische Meßtechnik und Meßsignalverabeitung,
Technische Universität Graz
8010 Graz, Austria

Graz, November 2018

EIDESSTATTLICHE ERKLÄRUNG

Ich erkläre an Eides statt, dass ich die vorliegende Arbeit selbstständig verfasst, andere als die angegebenen Quellen/Hilfsmittel nicht benutzt, und die den benutzten Quellen wörtlich und inhaltlich entnommenen Stellen als solche kenntlich gemacht habe.

Graz, am..... .....

(Unterschrift)

Wem der große Wurf gelungen
Eines Freundes Freund zu sein;
Wer ein holdes Weib errungen
Mische seinen Jubel ein!

(Friedrich Schiller — An die Freude)

Acknowledgement

I thank my supervisor Univ.-Prof. Dipl.-Ing. Dr.techn. Georg Brasseur for his support in this dissertation project, the supervision of my scientific work and the freedom to set the focus of the dissertation. Furthermore, I would like to thank Ao.Univ.Prof. Dipl.-Ing. Dr.techn. Johann Ertl for writing the second opinion for the dissertation.

Additionally, I would like to express my gratitude to Ass.Prof. Priv.-Doz. Dipl.-Ing. Dr.techn. Hannes Wegleiter, Dipl.-Ing. Dr.techn. Bernhard Schweighofer and especially Dipl.-Ing. Michael Grubmüller for their support with microcontrollers and printed circuit boards.

Moreover, I am thankful for the inspiring conversations with my colleagues Dipl.-Ing. Dr.techn. Thomas Höll and Dipl.-Ing. Dr.techn. Johannes Fuchs.

I would also like to thank the State of Austria, which has made such an education possible for me.

A special thanks goes to my wife Ilga Johanna Lindenthaler-Hämmerle for the patience with me, the continuous motivation and the trust in me, especially when I did not have it.

Zusammenfassung

Für die Bestimmung der Effizienz von elektrischen Antrieben ist es notwendig die Wirkleistung zu messen. Dabei spielt die Messunsicherheit bei hocheffizienten Antrieben eine wichtige Rolle, da sich die Messunsicherheit der Wirkleistung stark auf die Unsicherheit der Effizienz auswirkt.

Bei hohen Genauigkeitsanforderungen sind Messungen an der AC-Seite eines Frequenzumrichters wesentlich anspruchsvoller als beispielsweise Messungen an der DC- Seite oder Leistungsmessungen an der mechanischen Welle. Der Grund dafür ist, dass es neben Standard-Herausforderungen in der Messtechnik wie zum Beispiel Amplitudenauflösung, Fehler in der Messkette und Messrauschen noch offene Fragen bezüglich der notwendigen Messbandbreite gibt. Bis dato gibt es keine Untersuchung, welche die notwendige Bandbreite für Messungen an der AC-Seite von Frequenzumrichtern empfiehlt. Daher analysiert die vorliegende Arbeit den Messfehler, der durch eine Bandbreitenbegrenzung hervorgerufen wird.

Zuerst wird die Beschränkung der Messbandbreite simulativ analysiert. Aus den Simulationen folgt, dass die Bandbreite des Messgerätes mögliche Resonanzeffekte im Antrieb abdecken muss. Der Grund dafür ist, dass die im Resonanzkreis umgesetzte Wirkleistung vor allem im Teillastbereich einen nicht vernachlässigbaren Beitrag zur gesamten Wirkleistung haben kann. Um die Aussagen mittels Simulation messtechnisch verifizieren zu können, wird eine Methode vorgestellt, mit welcher ein Referenzergebnis für die Wirkleistung auf der AC-Seite des Frequenzumrichters generiert werden kann. Die vorgestellte Methode funktioniert mittels Kalorimetrie und der Messung von DC-Größen. Da nur DC-Größen gemessen werden müssen, bietet sie eine geringe Messunsicherheit und aufgrund der Kalorimetrie ist sie unabhängig von einer Messbandbreite. Daher kann das so erhaltene Referenzergebnis zum Evaluieren von Messergebnissen mit einer beschränkten Bandbreite herangezogen werden.

Alle Untersuchungen und Messungen dieser Arbeit wurden für einen elektrischen Antrieb in einem Kraftfahrzeug ausgeführt. Der Antrieb beinhaltete einen permanenterregten Synchronmotor und einen Frequenzumrichter der mittels feldorientierter Regelung betrieben wird. Es können jedoch alle vorgestellten Methoden und die meisten Ergebnisse auf andere Antriebsstrukturen umgelegt werden.

Abstract

Electric power measurements are crucial for determining the efficiency of electric drives. The uncertainty of such power measurements becomes increasingly important in case of highly efficient drives, as the power measurement's uncertainty propagates to the efficiency's uncertainty.

From the viewpoint of measurement uncertainty, power measurements of the ac side of an inverter are more challenging as measurements taken on the dc side or at the mechanic part of the drive because of the switching inverter. Beside typical measurement issues like amplitude resolution, measurement chain imperfections and noise, it is unclear which measurement bandwidth is actually required for ac side power measurements. So far there is no scientific work available quantifying the required measurement bandwidth of a power analyzer. Therefore, this thesis analyzes the error stemming from a bandwidth limitation on basis of simulations and measurements.

Within the simulations, a developed lumped element model of the electric drive is utilized for evaluating the required bandwidth in the frequency domain. On basis of simulations it can be stated, that possible high frequency resonance effects have to be covered by the measurement bandwidth. If the bandwidth includes the resonance, the measurement error due to the limited bandwidth becomes negligibly.

For verifying the simulation-based findings, a combined calorimetric and dc measurement based measurement method is presented. The combined calorimetric method is free of a bandwidth limitation error and requires measurements of dc signals only. As dc signals can be measured accurately with relatively low effort, the calorimetric result provides a low level of uncertainty. Because of the low level of uncertainty and the inherently independence to bandwidth limitation errors, the combined calorimetric method is suitable as reference measurement to compare measurements from power analyzers.

All simulations and measurements in this thesis are carried out with an automotive electric drive with a permanent magnet synchronous motor and a three-phase inverter operating on the basis of field oriented control. However, most results and all methods can be transferred to other drive setups as all engineering details and parametrization routines are described in detail.

Contents

1

Introduction

The ongoing trend of electrification in all fields of society has led to the production of an enormous number of energy consuming devices. The energy consumption of the electric devices contributes to greenhouse gas emissions, because fossil resources are still the dominant feedstock for electric energy production. To reduce the emissions, all devices have to be as efficient as possible. Efficient devices waste only a small portion of the input power to fulfill the task, and most of the input power is utilized usefully.

A device's efficiency denoted by η cannot be determined by the measurement of a single quantity, as the efficiency η is defined as the ratio of the active output power P_{out} to the active input power P_{in}:

$$\eta = \frac{P_{\text{out}}}{P_{\text{in}}}. \tag{1.1}$$

As input P_{in} and output P_{out} power are measurable quantities, they include a measurement uncertainty:

$$P_{\text{in}} = \delta P_{\text{in}} + P_{\text{in,true}} \qquad P_{\text{out}} = \delta P_{\text{out}} + P_{\text{out,true}}, \tag{1.2}$$

where δP_{in} and δP_{out} denote the measurement uncertainties and $P_{\text{in,true}}$, and $P_{\text{out,true}}$ stand for the active true power of input and output. The power measurement uncertainties of the input δP_{in} and output δP_{out} are mentioned for the sake of completeness, as their value is generally unknown. In measurement technology, the uncertainty of δP_{in} and δP_{out} is typically expressed by means of a confidence interval of the probability distributions of the measurement uncertainties δP_{in} and δP_{out}. In this work, however, the power measurement uncertainties of the input δP_{in} and output δP_{out} uncertainty are quantified by an upper bound:

$$\left|P_{\text{in}} - P_{\text{in,true}}\right| \leq \Delta P_{\text{in}} \qquad \left|P_{\text{out}} - P_{\text{out,true}}\right| \leq \Delta P_{\text{out}} \tag{1.3}$$

The upper bound of the power measurement uncertainty is denoted correspondingly by ΔP_{in} for the input and ΔP_{out} for the output. For sake of simplicity, the term *upper bound* will be omitted, when referring to ΔP_{in} and ΔP_{out}.

The power measurement uncertainties of input ΔP_{in} and output ΔP_{out} result in an uncertainty $\Delta\eta$ of the computed device efficiency η:

$$\eta = \eta_{\text{true}} \pm \Delta\eta, \tag{1.4}$$

with η_{true} denoting the true device efficiency, defined by.

$$\eta_{\text{true}} = \frac{P_{\text{out,true}}}{P_{\text{in,true}}}. \tag{1.5}$$

In order to measure the device efficiency η with a high degree of accuracy, it is necessary to make active power measurements P_{in} and P_{out} with low measurement uncertainties for ΔP_{in} and ΔP_{out}. The higher the device efficiency η becomes, the lower the tolerable uncertainties of the active power measurements P_{in} and P_{out} will be.

The worst case measurement uncertainty $\Delta\eta$ of the device efficiency η can be computed by the error propagation obtained from Equation (1.1), which is shown in Appendix C.

The worst case measurement uncertainty $\Delta\eta$ of the device efficiency η results in

$$\Delta\eta = \eta \cdot \left(\frac{\Delta P_{\text{out}}}{P_{\text{out}}} + \frac{\Delta P_{\text{in}}}{P_{\text{in}}} \right). \tag{1.6}$$

In Equation (1.6), the term $\frac{\Delta P_{\text{out}}}{P_{\text{out}}}$ corresponds to the *relative* output power measurement uncertainty and $\frac{\Delta P_{\text{in}}}{P_{\text{in}}}$ to the *relative* input power measurement uncertainty. For the sake of simplicity, in the following analysis the relative input power uncertainty $\frac{\Delta P_{\text{in}}}{P_{\text{in}}}$ and the relative output power uncertainty $\frac{\Delta P_{\text{out}}}{P_{\text{out}}}$ are assumed to be equal to a relative power measurement uncertainty $\frac{\Delta P}{P}$:

$$\frac{\Delta P_{\text{in}}}{P_{\text{in}}} = \frac{\Delta P_{\text{out}}}{P_{\text{out}}} = \frac{\Delta P}{P}. \tag{1.7}$$

Figure 1.1 presents the relationship between the true efficiency η_{true}, the relative power measurement uncertainty $\frac{\Delta P}{P}$ and the resulting uncertainty bounds of the computed device efficiency $\eta \pm \Delta\eta$. The computation in Figure 1.1 is evaluated for three different power measurement uncertainties $\frac{\Delta P}{P}$ ranging from 0.1 % to 1 %, according to Equation (1.6). As mentioned above, the value of the relative power measurement uncertainty $\frac{\Delta P}{P}$ is used for both the relative power measurement uncertainty of the input $\frac{\Delta P_{\text{in}}}{P_{\text{in}}}$ and the output $\frac{\Delta P_{\text{out}}}{P_{\text{out}}}$.

As can be seen in Figure 1.1, measurements of a device with an exemplary true efficiency η_{true} of 90 % can result in a calculated efficiency $\eta \pm \Delta\eta$ of 88 % to 92 % if derived from power measurements with a relative measurement uncertainty of $\frac{\Delta P}{P}$=1 %. The smaller the relative power measurement uncertainty $\frac{\Delta P}{P}$ becomes, the smaller the resulting uncertainty in the efficiency $\Delta\eta$ is.

An issue arises if the improvement in a device's efficiency η is evaluated. To evaluate the improvement, the efficiency η has to be determined before and after making the improvement. The issue is exemplified by considering a device with a true starting efficiency of η_{true} =90 % and a power measurement uncertainty of $\frac{\Delta P}{P}$ =0.3 %, as summarized in the first example of Table 1.1. The initially measured efficiency η can range from 89.4 % to 90.6 %. After improving the efficiency, the device's true efficiency η_{true} increases. To verify the increase of the device's efficiency η, a second efficiency measurement is required. By comparing the device's efficiency η before and after the optimization, the power measurement uncertainty $\frac{\Delta P}{P}$ becomes an important

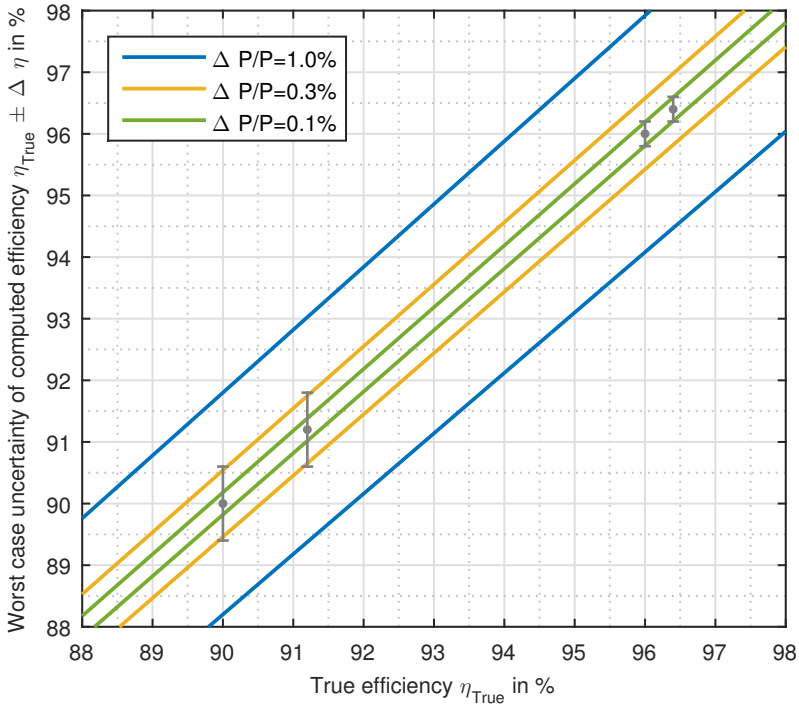

Figure 1.1.: Worst case measurement uncertainty of the efficiency $\eta \pm \Delta\eta$ as a function of the true device efficiency η_{true}. The colors denote the uncertainty range for different relative power measurement uncertainties $\frac{\Delta P}{P}$. The grey bars are operating points discussed in the text and listed in Table 1.1.

parameter. As can be seen in Figure 1.1, the smallest efficiency increase has to be at least approximately 1.2 % leading to a true efficiency η_{true} of 91.2 % for a relative power measurement uncertainty $\frac{\Delta P}{P}$ of 0.3 %. Smaller increases of the true efficiency η_{true} can get lost in the efficiency's uncertainty $\pm\Delta\eta$. Obtaining an efficiency increase of 1.2 %, however, can be a challenging task, as it implies the reduction of the device's losses by approximately 10 %, which may be hard to obtain.

A relative power measurement uncertainty $\frac{\Delta P}{P}$ of 0.1 % is considered as a second example with a true starting efficiency η_{true} of 96 %. After the improvement, the true efficiency η_{true} has to be at least 96.4 % so that the improvement can be verified, as summarized in Table 1.1. The minimum detectable efficiency improvement of 0.4 % is again equal to a reduction in all losses by 10 %. If the efficiency increase of 0.4 % cannot be achieved, the intended efficiency increase could possibly reduce the true efficiency η_{true} without affecting the measured efficiency η.

Table 1.1.: Efficiency measurement range $\eta = \eta_{\text{true}} \pm \Delta\eta$ ($\Delta\eta = \eta \cdot 2 \cdot \frac{\Delta P}{P}$, see Equation (1.6)) and true efficiency η_{true} for the improvement of a device. The two numeric examples illustrate the influence of the relative power measurement uncertainty $\frac{\Delta P}{P}$ on the true device efficiency η_{true} and the range of the measured device efficiency η before and after the improvement of the device. Both examples are shown in Figure 1.1 and discussed in the text.

		Starting efficiency		Improved efficiency	
Example	$\frac{\Delta P}{P}$	η_{true}	η	η_{true}	η
1	0.3 %	90 %	89.4 % to 90.6 %	91.2 %	90.6 % to 91.8 %
2	0.1 %	96 %	95.8 % to 96.2 %	96.4 %	96.2 % to 96.6 %

In order to compute reliable efficiency η results, it is essential to obtain knowledge of the power measurements' uncertainty $\frac{\Delta P}{P}$, as the power measurements' uncertainty $\frac{\Delta P}{P}$ determines the uncertainty of the efficiency $\Delta\eta$. Power measurements of highly efficient devices have to provide *sufficiently small* levels of uncertainty, as the tolerable level of the power measurement's uncertainty decreases along with the device's efficiency. A *sufficiently small* uncertainty of the power measurement $\frac{\Delta P}{P}$ can be defined by the requirement that the uncertainty $\Delta\eta$ of the efficiency η is much smaller than the efficiency itself or the efficiency improvement.

1.1. Power Measurements of Electric Drives

The largest group of devices among electric energy consumers are electric motors, which consume 46 % of global electric energy [1, p. 33]. Therefore, the efficiency of electric motors and drives has a strong impact on greenhouse gas emissions and their efficiency η should be as high as possible.

Electric drives are utilized in a wide field of applications ranging from industrial to residential uses. They are also increasingly used in the field of transportation and mobility. The IEEE Authoritative Dictionary [2] defines an electric drive as "a system consisting of one or several electric motors and of the entire electric control equipment designed to govern the performance of these motors." Electric drives consist typically of three components: an electric motor, an inverter and a control system, as illustrated in Figure 1.2. The motor converts electric energy into torque. The inverter applies

a switching scheme for converting dc power into ac feed signals for the motor. A superimposed control system generates control signals to adjust different variables like position, speed, or torque, depending on the design requirements.

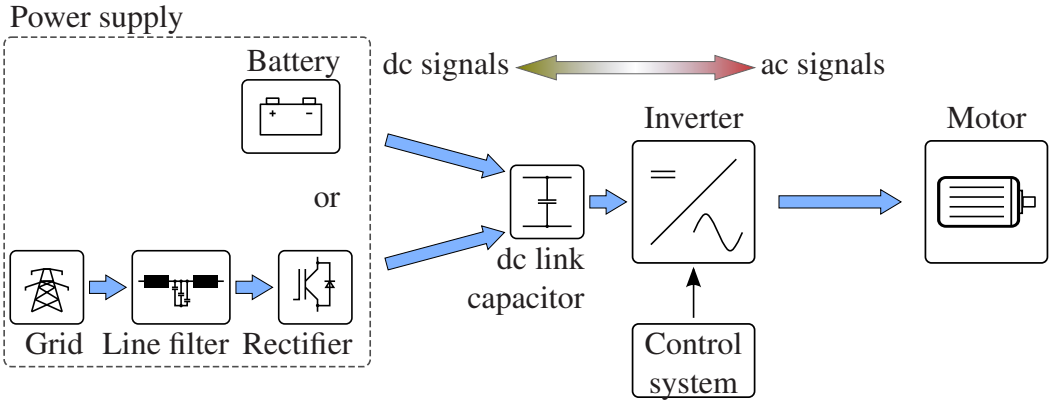

Figure 1.2.: Schematic power flow of an electric drive in motor mode from the inverter's dc to ac side. In automotive applications a battery provides the input power, whereas in industrial applications the power is typically provided by the power grid in combination with a filtering and active rectifier stage [3]. The intermediate dc voltage link is filtered by capacitors and inductors. A control system provides the switching pattern such that the motor follows a specified rotational speed, torque or position. Because of the switching, the ac side consists of voltage signals with a high slew rate.

To make electric drives as efficient as possible, the motor and inverter have to be optimized on an individual basis and, additionally, as a whole system. The optimization may range from changes in the inverter topology to mechanical and thermal design improvements to the use of optimal control strategies. To whichever extent the optimization is performed, the efficiency improvement has to be determined based on measurements to achieve reliable results. To determine the efficiency, it is necessary to take power measurements at three different sensing locations. The inverter's efficiency is determined by power measurements on its dc input and ac output sides. The motor's efficiency is characterized by the mechanical shaft power and the electrical input power (ac side power of the inverter). The overall system efficiency of the drive is determined by power measurements from the dc input to the mechanical shaft power.

The three sensing locations for the power measurements differ in the efforts required to achieving the desired uncertainty level. Basically, the effort to obtain measurements with low uncertainties depends on the signal's rate of change. Slowly changing signals can be acquired with low levels of uncertainty and relatively small efforts. In contrast,

a signal acquisition system with low measurement uncertainty for rapidly changing signals is expensive.

From a general perspective, electrical power P on the ac or dc side of the inverter is measured by calculating the arithmetic mean of the product of the voltage $u(t)$ and the current $i(t)$:

$$P = \frac{1}{T} \int_0^T u(t) \cdot i(t) \, \mathrm{d}t. \tag{1.8}$$

Measurements of the mechanical shaft power are taken by torque and rotational speed measurements. However, mechanical power measurements were not in the focus of the work presented in this thesis, as commercial torque and rotational speed sensors that offer sufficiently low levels of uncertainty for shaft power measurements are available on the market.

The primarily function of the inverter is based on its switching operation. This switching operation generates rectangular voltage pulses with fast rise times. The fast rise time is desirable, as it reduces losses in the inverter switches. However, in terms of signal acquisition and measurement uncertainty, it is harder to capture the rapidly switching signals with a low level of uncertainty than to capture slowly changing signals. For example, measurements taken on the dc side of the inverter can provide a lower uncertainty as on the ac side, as the dc link capacitor filters the switching operation on the power supply side of the drive. Because of the dc link capacitor, the signal dynamics are reduced on the power supply side. However, a ripple will remain in the dc current, but the ripple frequency is limited to the electrical fundamental frequency of the motor times the number of phases. Therefore, the signal ripple is a slowly varying signal measurable with a low level of uncertainty. The same principle applies to power measurements taken on the mechanical side of the drive: Here the rotor inertia acts as an energy storage and filters out fast signal components. In contrast to the mechanical and dc sides, the ac side of the inverter is not equipped with a reasonably large energy storage. These signals are, therefore, directly affected by the inverter switching and provide a high rate of change. To obtain accurate power measurements at the ac side of the inverter, special attention is required. A measurement system for the ac side has to be accurate and sufficiently fast to handle all the transient signals.

Being able to handle fast signals implies that the entire measurement chain of a power measurement system provides sufficient processing speed in the analog and digital domains. The analog domain includes the analog front end and amplifier and filtering stages. In this case, the processing speed requirement relates to the wide bandwidth of the corresponding electronics. In the digital domain, it is necessary that the analog-to-digital converter (ADC) uses a high sampling rate and the algorithm is executed at a high processing speed. The required speed on the ac side leads to more effort in the design of a measurement device, since the high processing speed is required *in addition to* accuracy and precision.

1.2. Problem Statement

To make accurate power measurements on the ac side of an inverter, power analyzers are typically utilized. These power analyzers stem originally from power grid applications with sinusoidal voltage and current. The voltage and current between inverter and motor, however, are not pure sinusoidal waveforms, as shown in the measurements in Figure 1.3. The three plots in Figure 1.3 show

(a) the approximately sinusoidal waveform of the motor current,

(b) the underlying switching pattern and

(c) overshoots and ringing in voltage and current signals when switching occurs.

Therefore, state–of–the–art power analyzers have a frequency range of up to 10 MHz, to guarantee the measurement of the high slew rates in electric drives. It is however unclear how the measurement bandwidth of power analyzers coheres to the measurement uncertainty. Furthermore, the power measurement uncertainty of a power analyzer is typically specified for pure sinusoidal signals only. Therefore, the open question has to be answered how the specified uncertainty of a power analyzer can be evaluated when non-sinusoidal signals form an actual inverter are applied.

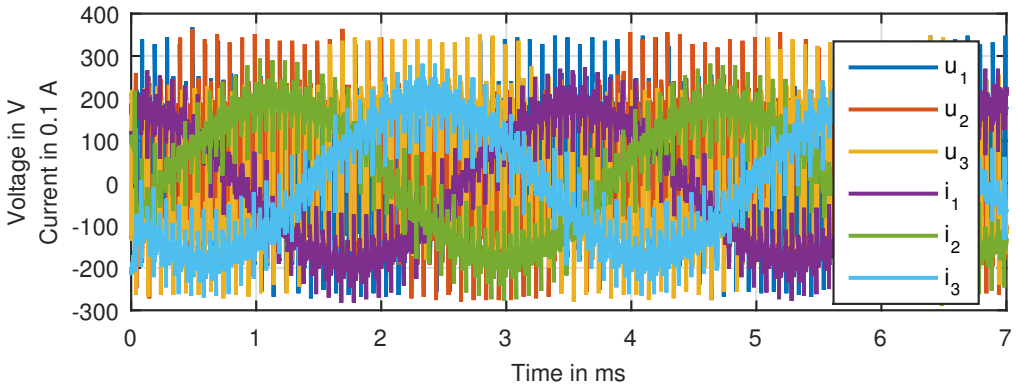

(a) Large scale waveforms with approximately sinusoidal currents.

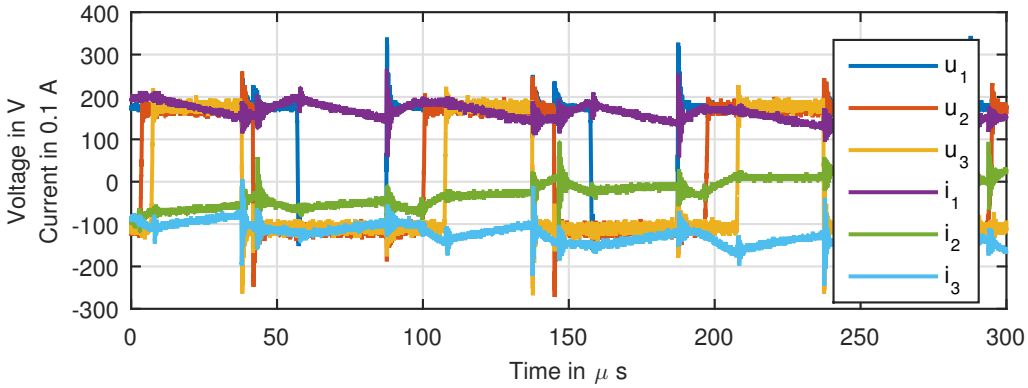

(b) Switching pattern of voltage signals.

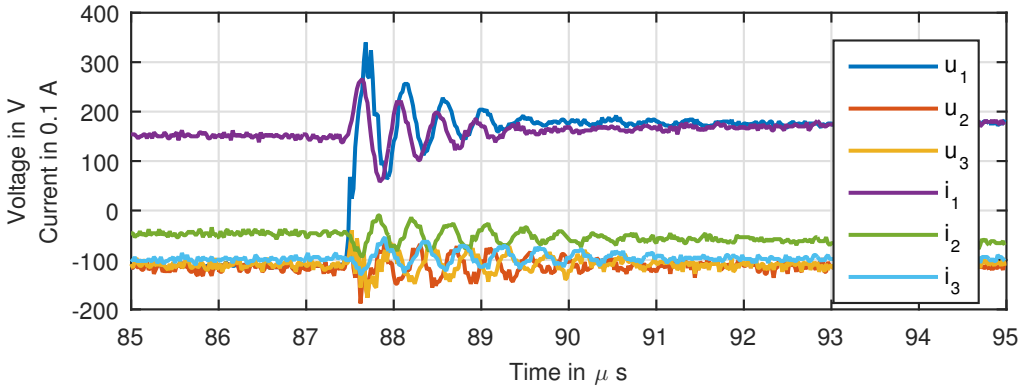

(c) Ringing in voltage and current signals.

Figure 1.3.: Measured phase voltage and current waveforms on the ac side of an inverter. All waveforms stem from an automotive drive and the three zoom levels provide a consistent time scale. The dc bus voltage is 300 V, and the operating point plotted has 2.7 kW with a root mean square (RMS) phase voltage of 145 V and a RMS current of 13 A.

Therefore, this thesis addresses the following research questions:

1. How can the electric drive be modeled to make power measurements with low uncertainty between the motor the and inverter?
2. What is the relationship between the power measurement uncertainty and the measurement bandwidth of the metering device?
3. Is it possible to perform a power measurement free of a bandwidth limitation?

1.3. Personal Contributions and Thesis Outline

The answer to the three research questions is given in five chapters with the following content. Chapter 2 presents a review of the literature about state–of–the–art commercial power analyzers and related literature.

Subsequently, Chapter 3 describes a simulation model of an electric drive for analyzing the measurement uncertainty of power measurements. The electric drive is modeled as a load impedance excited by voltage pulses form the inverter, whereby Chapter 3 focuses on load impedance modeling. Standard impedance models consist of simple resistor-inductor series circuits with a counter-electromotive force (CEMF), neglecting parasitic coupling paths within the electric drive. These simple models are not capable of capturing effects that are present in measured signals and therefore such simple models are not suitable for analyzing the power measurement uncertainty. As a result, the presented load impedance model takes parasitic coupling paths into account so that the behavior of a drive can be simulated more realistically. The author's description of the model development is documented in article [**4**]

[4] **D. Lindenthaler** and M. Neumayer, "Improved load modelling for switching power supplies in electrified vehicles," in *Industrial Electronics (ISIE), 2014 IEEE 23rd International Symposium on*, Jun. 2014, pp. 824–829

In Chapter 4, the relationship between the measurement bandwidth and the resulting uncertainty is analyzed based on simulations with the lumped element model from Chapter 3 serving as load model.

The basic idea to evaluate the effect of bandwidth limitation on power measurements is presented in article [**5**]

[5] D. Lindenthaler, "Signal-bandwidth evaluation for electric power calculation in PWM driven motors," in *Precision Electromagnetic Measurements (CPEM), 2014 Conference on*, Aug. 2014, p. 2

The proposed method in [**5**] is based on Fourier domain computations. However, a simple resistor–inductor series circuit is used to model the load impedance. Therfore, the fusion of the extended lumped element load model from [**4**] and the evaluation method from [**5**] is presented in article [**6**] at which the bandwidth limitation based on a realistic impedance model of the load is investigated. The numerical study described in the article addresses the effects of variation of cable length and discusses the sources of the bandwidth limitation.

[6] D. Lindenthaler and G. Brasseur, "Signal-bandwidth evaluation for power measurements in electric automotive drives," *IEEE Transactions on Instrumentation and Measurement*, vol. 64, no. 6, pp. 1336–1343, Jun. 2015

For verifying the simulations from Chapter 4, a reference measurement for the active power on the ac side of the inverter was required. Chapter 5 presents a method to obtain such a reference measurement result. The method is based on calorimetry, and its measurement result is compared to that of a power analyzer measurement. The main advantage of the presented measurement method is that it is inherently free of a bandwidth limitation error. To provide a fair comparison, the uncertainty of the calorimetric method is evaluated and compared to the power analyzer's measurement uncertainty. The related publication is

[7] D. Lindenthaler and G. Brasseur, "Ac power measurements of electric drives: A method incorporating calorimetry and dc measurements only," *E & i Elektrotechnik und Informationstechnik*, vol. 134, no. 2, pp. 197–202, 2017

Further Work

In [**8**], the effect of asynchronous sampling of voltage and current is investigated. The investigated setup considers power measurements taken at the line frequency. To synchronize voltage and current, different interpolation kernels are evaluated and the influence on the power measurement uncertainty is quantified.

[8] **D. Lindenthaler** and H. Zangl, "Evaluation of uncertainty in ac power calculation with asynchronously sampled data," *Journal of Physics: Conference Series*, vol. 450, no. 1, p. 012 043, 2013

2

State of the Art

This chapter reviews the setup of electric automotive drives, measurement theory of power analyzer and related literature.

2.1. Electric Automotive Drives

The general setup of the drive components and measurement system is illustrated in Figure 2.1. The illustration contains the power cabling of the components and electric measurement signals on the ac and dc side of the inverter. The interaction of motor, inverter and control within automotive environments is described in the following sections.

2.1.1. Electric motor

For automotive drives, mainly three phase-motors are used. These motors are either permanent magnet synchronous motors (PMSM), induction motors or switched reluctance motors [9]. The type of motor utilized depends on costs, efficiency, volume restrictions, torque, power and speed requirements and, behavior in case of malfunction. This work considers PMSMs. Currently, PMSMs are used in commercial hybrid and electric vehicles [10], like Volkswagen e-Golf, Toyota Prius, BMW i3 and Peugeot iOn. Nevertheless, the modeling approach presented in Chapter 3 can be applied to induction motors as well. The bandwidth limitation evaluation presented in Chapter 4 works directly for induction motors, since induction motors and PMSMs are typically fed by three phase inverters. The calorimetric measuring method of Chapter 5 can be universally applied to drives that use a voltage source inverter. In this work the iron saturation of the electric motor is not considered. With iron saturation, the motor inductance decreases and the motor current can increase until the motor is destroyed. However, if the motor is controlled by an inverter, the inverter will monitor the motor current and will limit the motor current to the permissible range.

2.1.2. Inverter DC/AC

The topology considered in this thesis is a three-phase bridge inverter. The switches are typically realized by metal–oxide–semiconductor field-effect transistors (MOSFET) or insulated-gate bipolar transistors (IGBT) with an anti-parallel diode. In comparison to MOSFETs, IGBTs have typically lower conduction losses and slower switching times and thus higher switching losses [13, p. 690]. In addition, IGBTs offer higher voltage and current capability than MOSFETs. Therefore, mainly IGBTs are used for applications with high currents at voltages above approximately 200 V [13, p. 691], such as in automotive drive systems.

2.1.3. Control

A variety of control schemes for PMSMs exists. Within the field of traction drives, all commercially relevant control schemes apply the dc supply voltage of the inverter for a

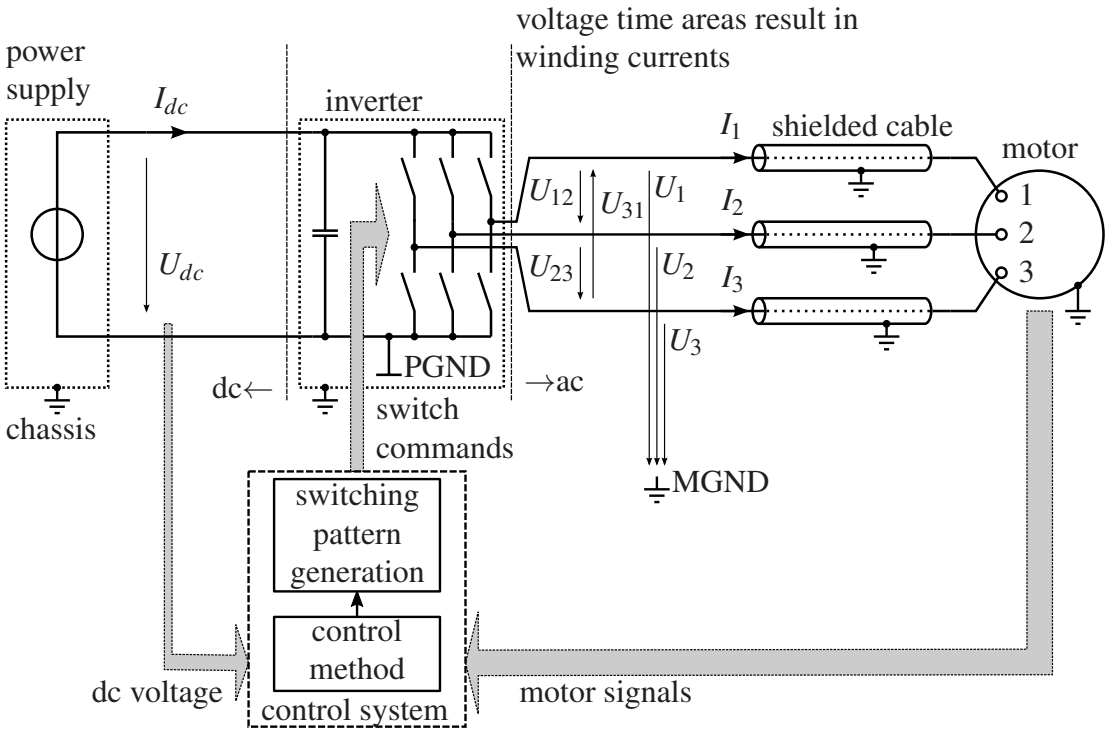

Figure 2.1.: Components and measurement signals of an electric drive. In automotive applications, the conductive housings of power supply, inverter and motor are connected to the chassis. According to the ISO standard [11], an electric vehicle with a dc bus voltage between 60 V and 1000 V is a *voltage class B* system. In this case, the power supply outputs have to be galvanically insulated from chassis for safety reasons [11], [12]. The reference potential for measurements is the measurement ground, denoted as MGND. The measurement ground MGND is typically bonded to chassis. Capacitive couping paths are shown in Figure 3.5 in Chapter 3 and in Figure 5.2 in Chapter 5.

short but variable time and variable polarity to the motor windings in order to obtain the requested current flow. Due to the variety of control schemes, only a rough classification and a short description of the relevant control methods is presented in this section. The textbooks [14] and [15] provide a comprehensive review and a detailed performance discussion.

In this dissertation the term control in connection with electric drives describes the system that controls the binary inputs for the six electronic power switches in the inverter from a control variable such as speed, current or torque. Typically, the entire control is realized fully digitally on a microcontroller with corresponding timer units. Therefore,

the control method is not limited by physical limits such as the maximum rise time of the electronic power switches. The following sections deal with the control schemes in two steps: firstly, the control method and secondly, the switching pattern generation for the inverter, as shown in Figure 2.1 and Figure 2.2.

In principle, the control method comprises all digital control elements for calculating a voltage command, so that the motor runs with the desired current or torque. The switching pattern generation block in Figure 2.2 then converts the voltage command into the actual switch commands for the inverter. The inverter executes the switching commands considering physical limitations like maximum motor currents and overtemperature and generates voltage-time areas leading to the desired motor current. The vector product of current and flux gives the torque. Therefore the variables flux, current and alignment angle between current and flux influence the generated torque. Depending on the control method different combinations of control variables are used and controlled.

Control Method

Basically, two control methods are relevant for PMSMs in automotive traction drives: scalar control (U/f) and vector control.

Within the framework of scalar control, the fundamental voltage amplitude and frequency is steered. The key concept of the scalar control is, that the voltage time area is adjusted proportionally to the frequency to keep the motor current (equal to torque) constant. A drawback of scalar control is the lack of a direct current control in contrast to the other control methods discussed further. Therefore, scalar control techniques tend to a slower control response time and the zero speed torque is significantly lower than the nominal motor torque [16].

As a result, applications with high performance requirements utilize vector control methods. Vector control schemes are based on the assumption that the magnetic field distributions and phase currents in an electric motor can be described by position and time dependent sine waves. The sine waves are represented by space vectors. These space vectors are categorized in a flux generating component and in a torque generating component. Both vector components are controlled variables within vector control. The motor's air gap torque is a function of the vector product of the current and flux. The

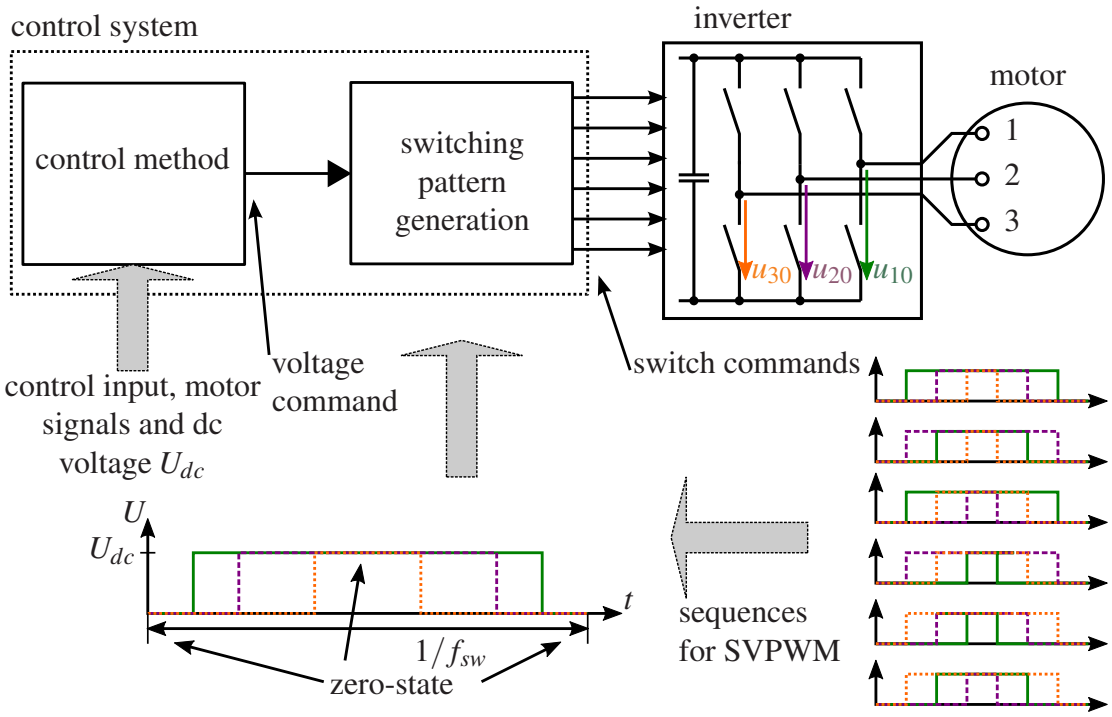

Figure 2.2.: Control of electric drives with the combination of control method and switching pattern generation. The switching commands result from the voltage command of the control method. The degrees of freedom for PWM methods include the switching frequency f_{sw}, the distribution of the zero-states and the switching state sequence. The lower right part shows the switching sequences for space-vector PWM (SVPWM). The position of the rotor determines the switching sequence, whereby the amplitude of the voltage command and the rotor position together determine the time between the switching actions. Direct torque control (DTC) combines the control method and the switching pattern generation.

associated vector control methods are direct torque control (DTC) and field oriented control (FOC). The angle between between flux and current can be either constant which yields to the classic FOC with a steered length of the current vector. Another possibility is, to keep the current vector length constant and vary the angle between flux and current. As the current vector length is always constant, fast torque response times can be realized. A disadvantage of the constant current method are the higher losses, since the motor always operates with nominal apparent power and thus the full copper losses occur permanently. A combined variation of angle and vector length is the so called maximum-torque-per-ampere control strategy. Thereby, the current vector length and angle between the current and flux space vector is controlled, such that the motor

efficiency is maximized.

Within direct torque control (DTC), discontinuous controllers are utilized for increasing and decreasing flux and torque in the motor. The controllers consist of a switching table for steering the switching pattern of the inverter. Basically, the switching table has the states *increase or decrease torque* and *increase, decrease or leave flux* as input and a corresponding switching command for the inverter as output. Due to the discontinuous nature of DTC, it is robust against parameter variations, provides a fast torque response time and requires low computational effort. However, a ripple in torque and current remains in the control response [17].

Within field oriented control (FOC), the current vector components are controlled with continuous proportional–integral (PI) controllers. Therefore, FOC provides a smaller ripple in current and torque [17]. As a high current ripple increases the motor losses, FOC is more suitable for automotive drives because of the high efficiency requirements. In comparison to DTC, FOC operates in the coordinate system of the rotor and therefore additional coordinate transforms are required for mapping the control output into stator coordinates. The coordinate transforms result in a higher computational complexity of FOC method. In this work, most considerations will concentrate on FOC but most findings can be transferred to DTC.

Switching Pattern Generation

The output of the scalar and vector control method is a voltage command within the digital control algorithm. In case of scalar (U/f) control, the voltage command is given in amplitude and frequency variables. Vector control utilizes torque and flux (d and q) variables of the voltage space vector. Independently of the control variables, the control method's output voltage command has to be processed such that it can steer the electronic power switches of the inverter.

In case of DTC, the switching pattern generation of the voltage command is included in the switching table. Therefore no explicit switching pattern generation is required.

For scalar control and FOC, the switching pattern is generated by pulse-width modulation (PWM) methods. A survey on PWM methods and their properties is given in [18]. In principle the purpose of PWM is to approximate the voltage output of the

control system by a discrete switching pattern in the inverter. The degrees of freedom of the PWM methods range from the sequence of the switching states and the switching frequency to compensation strategies of the inverter's non-idealities and modifying the harmonic content of the PWM voltage signal.

The sequence of the switching states per cycle affects mainly the switching losses, the zero sequence waveform and the current ripple [19]. The possibly most popular method for generating a switching pattern is called space-vector PWM (SVPWM). Within SVPWM, the switching period starts with *all inverter phases at negative potential*, continues with *all phases at positive potential* and ends with *all phases at negative potential*, as illustrated in Figure 2.2. When all phases are at the same potential, the state is called zero-state. All other states are so called active states, as a non-zero voltage time area is applied to the motor. At SVPWM, all zero-states are distributed equally over the switching period. The equal distribution leads to a comparable low current ripple. More advanced switching patterns leave out the central zero-state for reducing inverter losses. A drawback of advanced switching patterns is however an increased current ripple [19].

The switching frequency of the PWM affects the resulting current ripple, the switching losses and the harmonic content of the phase voltages. The current ripple increases by decreasing the switching frequency, as less control actions are performed per time interval. In contrast, the switching losses of the inverter decrease with a decreasing switching frequency, as the switching losses occur per switching action. There are multiple possibilities for steering the harmonic signal content, depending on the desired implications to the drive system. One implementation possibility of the PWM is to utilize a fixed switching frequency independently of the actual rotational speed of the motor. The fixed frequency approach leads to a simple implementation as the complete drive control operates on a fixed timing. Due to the fixed switching frequency, subharmonic frequencies may be present, as the number of switching cycles per electric period does not have to be an integer number. Subharmonic frequencies can be problematic, as they can lead to iron saturation and overcurrent of the electric motor if the control method has no current control. Therefore, the synchronized PWM is proposed in [18]. Within synchronized PWM, the number of pulses per (electrical) revolution is an integer number. However, the number of pulses per revolution has to be adopted to the rotational speed to obtain a low current ripple. This adaption yields to undesired current transients [18].

A general drawback of a fixed number of pulses or fixed switching frequency is the fixed spectrum. The fixed spectrum gives an energy concentration at the switching frequency. This concentrated energy can yield to undesirable acoustic noise. Therefore a common approach is to randomize the switching frequency for blurring the spectrum and reducing the concentrated noise amplitudes. DTC cannot be compared directly with PWM-based methods in terms of switching pattern generation, since DTC generates the switching pattern directly using the switching table. Anyway, in terms of switching frequency and pattern generation DTC belongs most likely to the group of a randomized switching frequency, as the switching actions are performed on demand on basis of the switching table.

The electronic power switches of the inverter do not behave ideally and have a limited rise and fall time. The limited rise and fall time yields to an allowed duty cycle in the range of some percent up to some 99 %. In principle, the duty cycle limitations can be compensated when they are taken into account when computing the pulse-widths within the control algorithm. If the drive is used in a closed loop control system however, the PWM limitations are compensated [18, chapter IV.] by the control loop.

2.1.4. Frequency Classification

The acquisition of ac signals at an inverter is challenging in terms of measurement uncertainty because of their non-sinusoidal waveforms. To clarify the terms related to the spectral content of a signal, the voltage and current signals are categorized in three different frequency ranges. The frequency ranges are illustrated in Figure 1.3 on page 9 and denoted as follows:

Fundamental frequency range: This range denotes the fundamental frequency of the voltage and current signals. Depending on the maximum rotational speed of the motor and the number of pole pairs, the fundamental frequency can range up to some kilo Hertz. This signal part is illustrated in Figure 1.3(a). The fundamental frequency corresponds directly to the frequency of the motor's counter-electromotive force (CEMF) and induced voltage.

Switching frequency range: The switching frequency describes the number of *on and off* switching operations per time unit. Typical values for current inverters are in

the range of 5 kHz to 30 kHz. For a typical switching pattern of the voltage see Figure 1.3(b).

High frequency range: In this thesis, the high frequency range denotes all signal components above the switching frequency range. As will be discussed in Chapter 4, ringing and overshoots are covered and illustrated in Figure 1.3(c).

2.2. Measurement Theory of Power Analyzer

2.2.1. Electric Power

From a general physical viewpoint, power describes the rate of energy transfer or conversion per time unit. In electrical engineering, the term power relates to a larger number of quantities: apparent power, active power, instantaneous power, reactive power, fundamental power and other types of power defined in the IEEE -Standard 1459 [20]. In the context of power measurements for efficiency determination, mainly two definitions are relevant: instantaneous power $p(t)$ and active power P. The instantaneous power $p(t)$ describes the rate of energy transfer $W(t)$ at an infinitesimal time unit dt and it calculates from the product of voltage $u(t)$ and current $i(t)$

$$p(t) = \frac{\mathrm{d}W(t)}{\mathrm{d}t} = u(t) \cdot i(t)\,. \tag{2.1}$$

Active power P describes the average value of energy transfer and it is defined as the average of the instantaneous power $p(t)$ over an *infinite* time interval T

$$P = \lim_{T\to\infty} \frac{1}{T} \int_{t_0}^{t_0+T} p(t)\,\mathrm{d}t = \lim_{T\to\infty} \frac{1}{T} \int_{t_0}^{t_0+T} u(t) \cdot i(t)\,\mathrm{d}t. \tag{2.2}$$

In case of periodic current and voltage signals, i.e.

$$u(t) = u(t + k \cdot T) \qquad i(t) = i(t + k \cdot T) \qquad \forall k \in \mathbb{N}, \tag{2.3}$$

the infinite interval can be reduced to a finite interval of an integer multiple k of the signal period T

$$P = \frac{1}{k \cdot T} \int_{t_0}^{t_0 + k \cdot T} u(t) \cdot i(t) \, \mathrm{d}t. \tag{2.4}$$

Power measurement devices try to determine the active power P in Equation (2.4) as accurately as possible.

Today, most measurement devices operate in the digital domain. Therefore, the active power is computed on basis of samples of the voltage $u[n]$ and current $i[n]$. The true active power P from Equation (2.4) is approximated by a discrete summation, denoted by $\bar{P}$

$$\bar{P} = \frac{1}{N} \sum_{n=N_0}^{N+N_0-1} u[n] \cdot i[n]\,. \tag{2.5}$$

By comparing the continuous power Equation (2.4) with the discrete equivalent Equation (2.5), three sources of measurement uncertainty are evident:

1. The integral is approximated by a discrete summation.
2. The range for taking the average value N has to be determined such that it corresponds to an integer multiple of the continuous signal period $k \cdot T$.
3. The sampled values of voltage $u[n]$ and current $i[n]$ are used for the computation instead of the analog signals $u(t)$ and $i(t)$. Therefore imperfections of the measurement chain have to be considered.

Integral Approximation

In terms of approximating the integral from Equation (2.4) by a discrete sum in Equation (2.5), it can be shown that both results, the discrete power $\bar{P}$ and the continuous power P, are equal if the quasi-synchronous sampling [21] condition is fulfilled. One possible proof of conformance is shown in Appendix D. Basically, quasi-synchronous sampling means that both, the discrete and analog signal, are periodic, but with the

relaxation that the discrete and analog period can be different. Within quasi synchronous sampling, the voltage $u(t)$ and current $i(t)$ are sampled with the sampling frequency f_S, such that the sample period of the discrete signals $u[n]$ and $i[n]$ matches an integer multiple k of the continuous signal period T, i.e.:

$$u[n] = u[n+N] \qquad i[n] = i[n+N] \qquad \frac{N}{f_S} = k \cdot T \qquad N,k \in \mathbb{Z}. \tag{2.6}$$

In practice, quasi-synchronous sampling is a special case, as the signal's period T is generally unknown and the signals are sampled with a fixed sampling frequency f_S independently of the signal's period T. The sampled signals are not necessarily periodic. consequently, the integral approximation by a discrete summation needs not yoield to the same result as the integral. The sampling power meter has to find therefore a suitable integration interval N, such that the error is as small as possible.

Averaging Interval

The difference between the averaging interval in discrete domain over N samples and the continuous counterpart $k \cdot T$ results from the fact, that the averaging interval N has to be determined from the voltage and current samples. As voltage and current result from the inverter's switching operation, simple zero crossing algorithms or spectral analysis yields to large deviations between the true averaging interval $k \cdot T$ and the corresponding digital interval N. Although a large deviation of the true integration interval can lead to considerable errors in the active power, this error can be reduced by increasing the integration interval to multiple periods. From a theoretic viewpoint, the error relates to the sinc function, as shown in Appendix E. Therefore, the error decreases proportional with the integration time, i.e. $\frac{1}{N}$, and it can be made arbitrarily small by choosing the interval suitably large. However, it has to be noted, that a long averaging interval requires stationary operating conditions.

Measurement Chain Imperfections

The third difference between the continuously defined power Equation (2.4) and the digital equivalent of Equation (2.5) stems from differences between the samples $u[n]$, $i[n]$ and continuous instances $u(n/f_s)$, $i(n/f_s)$ of the signals. The difference results

from imperfections in the analog part of the measurement chain. The thereby involved components include probes and sensor, analog prepossessing electronics, filtering stages and the ADCs. Random and uncorrelated imperfections like white noise cancel out in the mean, whereas systematic imperfections like a bandwidth limitation results in an error in the active power. Therefore this thesis investigates which measurement bandwidth is actually required for accurate power measurements.

2.2.2. Current Power Analyzer

The one phase formulas Equation (2.4) and Equation (2.5) are extended to three phases to cover electric drives. From theoretic viewpoint, the power on the ac side P of the inverter is the sum of the three individual phase powers and it is defined as:

$$p(t) = \sum_{k=1}^{3} u_k(t) \cdot i_k(t) \qquad P = \frac{1}{T} \int_{t_0}^{t_0+T} p(t)\,\mathrm{d}t \tag{2.7}$$

$$\bar{p}[n] = \sum_{k=1}^{3} u_k[n] \cdot i_k[n] \qquad \bar{P} = \frac{1}{N} \sum_{n=N_0}^{N_0+N-1} \bar{p}[n]\,. \tag{2.8}$$

Therefore, a power analyzer has to capture the phase voltages $u_1(t)$, $u_2(t)$, $u_3(t)$ and phase currents $i_1(t)$, $i_2(t)$, $i_3(t)$ for computing the power $\bar{P}$.

Signal Acquisition

The voltage input is realized by a differential input stage including frequency compensated voltage dividers. The differential input stage is required as the power electronics ground (PGND) of an automotive drive has to be galvanically isolated from chassis, which is typically used as measurement ground (MGND), as illustrated previously in Figure 2.1 on page 15. Chassis and PGND are typically tapped by a voltage surveillance system which is mandatory for *voltage class B systems*, as defined in [11]. The voltage surveillance system permanently checks the isolation barrier between chassis and PGND to detect isolation faults that can pose a danger to humans. Basically, the drive is classified as voltage class B system, if the voltage level is above 60 $\mathrm{V_{dc}}$ or 30 $\mathrm{V_{ac}}$. The common mode input resistance of the differential voltage inputs has to be suitably high

such that the voltage surveillance system does not trigger an insulation fault. Therefore, power analyzer manufacturer are currently developing isolated voltage dividers with galvanic insulation in the analog or digital domain.

Typically, power analyzers capture the current signal either by an internal current shunt or by an external current sensor. The external sensor can be realized by an external shunt or a hall effect based sensor [22], [23]. The hall effect based sensors are mainly of closed-loop type with a hall element or a fluxgate magnetometer as zero-flux detector. Hall effect based sensors provide an insulated output but their measurement bandwidth is limited such that the high frequency content can possibly not be captured accurately. Current shunts provide a high bandwidth down to dc, but they suffer from galvanic insulation. Additionally, the power electronics cabling has to be modified for inserting the shunt.

Measurement Issues

Most electric devices are directly powered by the power grid. Even if the device includes an inverter, like electric drives, the device as a whole is typically supplied by the power grid, as illustrated in the lower part in Figure 1.2 on page 6. Therefore, sampling power meter have been optimized especially for application at the power grid. In terms of measurement accuracy, power grid signals provide desirable properties: sinusoidal waveforms, low frequency jitter and by regulations limited harmonic content. The left part in Figure 2.3 below illustrates typical signal curves for sinusoidal conditions. The sinusoidal measurement conditions lead to the fact, that almost all modern off-the-shelf power analyzer have the lowest uncertainty level at the mains frequency of 50 Hz/60 Hz.

Optimization of electric drives requires accurate power measurements between inverter and motor at the ac side of the inverter. The signals on the ac side of the inverter differ substantially from power grid signals as illustrated in Figure 2.3. Voltage and current do not provide a sinusoidal shape as they stem from the switching operation of the inverter. The voltage signal is almost rectangularly shaped with fast rise and fall times and the switching pattern determines the motor current. Depending on the control strategy and the type of electric motor, the current shape can range from approximate sinusoidal to nearly trapezoidal. Independently of the actual control strategy, the current includes less

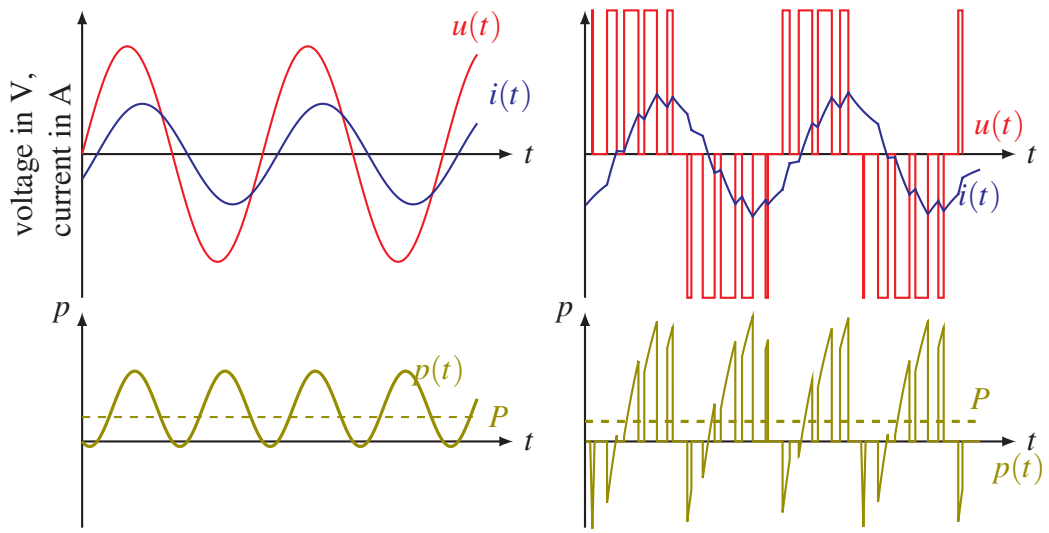

Sinusoidal conditions. Non-sinusoidal conditions.

Figure 2.3.: Illustrative comparison of sinusoidal and non-sinusoidal conditions for power measurements. Voltage $u(t)$, current $i(t)$ and instantaneous power $p(t)$ are more smooth in the sinusoidal case, making it more easy to accurately measure the active power P, as the bandwidth of the signals is low. In the non-sinusoidal case, the switching pattern is slightly different for each voltage cycle as the switching frequency can be unsynchronized to the rotational speed of the motor. The asynchronous run of the signals complicates the determination of a suitable integration interval N.

switching dynamics than the voltage. The lower dynamics in the current result from the resistive inductive behavior of the motor acting as lowpass filter for the rectangular voltage pulses. The non-sinusoidal voltage and current yield two power measurement issues in an electric drive:

The first measurement issue for the power is the limited bandwidth of a power analyzer. The rectangular voltage pulses produce a theoretically infinite spectrum and in practice the power analyzer requires a wide bandwidth for capturing the waveforms. The current provides reduced dynamics and therefore, most active power comes from the fundamental frequency f_{M} of the motor current. As a result, the analog measurement bandwidth has to include the motor's fundamental frequency range. The range from the switching frequency up to some ten times the switching frequency is roughly 5 kHz to 300 kHz. This switching frequency range includes the inverter's switching losses and the motor losses due to eddy-current and hysteresis. Therefore the switching frequency

range has still a considerable contribution to the total power and it has to be included in the power analyzer's measurement bandwidth. Above the switching frequency range, mainly HF effects dominate the behavior due to stray impedances within the electric drive. The contribution of the HF losses to the total power is small compared to the switching and fundamental power. Depending on the uncertainty requirements of the measurement and the operating point of the motor, the HF losses can have a non-negligible contribution to the total power as will be shown later in this thesis. However, it is not specified how large the measurement bandwidth has to be to comply with a predefined level of measurement uncertainty of the active power.

The second measurement issue relates to the uncertainty specifications of a power analyzer. Commercial power analyzer specify the power measurement accuracy as a function of the frequency, because primary electric power standards for calibration are realized with sinusoidal signals [24]–[27]. The signals on the ac side of an inverter are however not single-frequency signals. The current and voltage signals consist of mainly two parts: the switching operation of the inverter and the fundamental. The majority of commercial power analyzer manufacturers does not specify which frequency has to be used [28]–[33]. Some manufacturers provide measurement systems particularly for electric drives [34], [35]. However, these electric drives measurement systems do not provide an uncertainty specification for the active power. Furthermore, most power analyzer manufacturers state that the uncertainty specification holds only for sinusoidal signals [28]–[33]. As the signals on the ac side are non-sinusoidal, such specifications do not allow for uncertainty evaluations. Therefore, it is unclear how the result of the power measurement of a power analyzer that measures, evaluates or verifies switching inverter signals can be evaluated, since the author is not aware that a power measurement standard for switching inverter signals exists.

The difference between the continuous integral in Equation (2.7) and the digital counterpart in Equation (2.8) plays from a theoretic viewpoint a minor role in the power analyzer's uncertainty. If the measurement setup is designed such that aliasing can not occur, then the samples $u_k[n]$ and $i_k[n]$ can be interpreted as weighs of shifted sinc functions (Whittaker–Shannon interpolation formula [36]). Inserting voltage and current as infinite sum of shifted and scaled sinc functions in the original integral Equation (2.7) results in the discrete summation of Equation (2.8), as is shown in Appendix D. Current power analyzer can however be configured such that aliasing can occur, as can be seen

in Table 2.1. The table shows the sampling frequency and bandwidth for current power analyzer and almost all power analyzer suffer from aliasing if the full bandwidth is selected. However, the configuration of the power analyzer is up to the user and most models can be set up such that the bandwidth is limited and aliasing can not occur.

Table 2.1.: Comparison of current off-the shelf power analyzer. Data is collected on basis of the user manuals.

Power analyzer	Maximum sampling frequency	Maximum bandwidth	Reference
ZES LMG670	1.2 MSample/s	10 MHz	[28]
Yokogawa WT3000E	200 kSample/s	1 MHz	[29]
N4L PPA5500	2.2 MSample/s	2 MHz	[30]
DEWESoft Sirius	1 MSample/s	2 MHz	[34]
HBM Genesis	1 MSample/s	1.5 MHz	[35]
Hioki PW6001	5 MSample/s	2 MHz	[37]
Fluke Norma 5000	1 MSample/s	10 MHz	[31]
Keysight PA2203A	5 MSample/s	2.5 MHz	[32]
Tektronix PA3000	1 MSample/s	1 MHz	[33]

2.3. Related Work

This section reviews and discusses scientific work related to electric power measurements. The review includes realized power measurement devices from different work groups ranging from metrological institutions to research laboratories in the field of electric machines. The realized devices are compared with respect to the principle of operation, signal chain and evaluation algorithm. Commercial power analyzer are not analyzed in detail, as the corresponding user manuals provide typically no engineering details concerning the internal soft- or hardware. Publications contributing to measurement issues are discussed from three aspects: sources of uncertainty, evaluation of uncertainty and calibration of uncertainty sources. The literature review includes additionally modeling of electric drives and calorimetric measurement methods.

One of the first papers on power analyzers for the frequency range of electric drives presents the reference [38]. The authors introduce a power measurement device for the frequency range up to 20 kHz, denoted as audio frequency range. The presented

device of [38] is remarkable, as the power measurement device operates on basis of electrodynamic forces where the multiplication of voltage and current is carried out by magnetic fields. Electrodynamic devices however suffer from a limited bandwidth as they include mechanically moving parts with some inertia. To overcome the bandwidth limitation, researchers substituted the moving parts by electronics. In [39], a power measurement device based on electronic multiplication is proposed. The specific device did not increase the measurement bandwidth, but its development was a step into the right direction: electronics and digitization. Current power measurement solutions including analog multiplier are almost always used in grid applications, although two recent publications [40], [41] indicate the suitability for measurements of electric drives. The 10 MHz bandwidth of the presented analog multiplier solutions can already compete with standard off the shelf power analyzer for electric drives. Therefore it is possible that analog multipliers may be an alternative for the usage in power analyzers. Almost all current off the shelf power analyzer operate on basis of digital multiplication of voltage and current samples. The first wattmeter operating in the digital domain is presented in [42]. The hardware architecture of the first sampling wattmeter consists of two independent signal chains for voltage and current and utilizes two ADCs. This hardware design did in principle not change and is used even in current power analyzer. Main contributions to the development of power analyzer were given by metrological laboratories. Metrological laboratories are especially interested in power standards for calibration. Therefore working groups all over the world developed solutions [43]–[52]. Metrological devices have to provide a low level of uncertainty and therefore they are designed such that the uncertainty is firstly as low as possible and secondly traceable. All but the reference power analyzer from the Dutch National Metrolology Institute [52] utilize basically the same hardware structure as in the first digital sampling wattmeter from [42]. The dutch device utilizes only one common digitizer for digitizing voltage and current with a time division method. Because of this common digitizer, the device is limited to pure sinusoidal signals but due to the included switches only signal *ratios* are measured instead of absolute quantities. The ratiometric measurement strategy helps to keep the power measurement and calibration uncertainty low. The power standard from the Swedish metrology laboratory [48]–[50] was developed within a PhD thesis [53] and it is continuously improved [54]. Remarkable about the swedish solution [50] is, that it utilizes two commercial sampling voltmeters for the voltage and current measurement path. An interesting feature of the metrology device presented in [47] is the galvanic

insulation from the analog and digital part. The authors of [47] propose the realization with a galvanic insulation for having a low noise floor at the analog front end.

All of this meteorology devices are primarily designed for and tested with sinusoidal signals, as metrological power standards have evolved from dc to grid applications. Scientific power measurement instruments for electric drives differ from devices with a classical metrological background. Scientific instruments require more input channels, as ac motors have typically three phases. Additionally, uncertainty requirements are lower prioritized as in case of metrological devices, but the scientific instruments have to handle non-sinusoidal PWM signals. One of the first digital sampling wattmeter dealing with power measurements of non-sinusoidal signals is presented in [43]. The device is designed for power measurements of an electric drive and operates with a sampling rate of 1 MHz. Beside the presented power measurement device, the article [43] discusses briefly the sampling process for power measurements and gives two interesting and rare statements concerning the sampling process. The first statement is that the sampling frequency has to be four times the maximum analog signal frequency, as the digital multiplication of voltage and current doubles the maximum frequency and leads to aliasing in the digital domain. Secondly, the authors of [43] state that the aliasing error has *minor* influence on power computations as the switching frequency is not synchronized to the sampling frequency and therefore the aliasing error will cancel out in the mean. The underlying principles of signal sampling for power measurements are examined in detail in [21]. The examination reveals the concept of quasi-synchronous sampling. However the considerations in [21] focus on distorted signals of power line signals similarly to the publications [51], [55]. For non-sinusoidal signals, the authors recommend to sample over a relatively long signal period. Power measurement solutions especially designed for motor drives are presented in [56] and [57] where the authors deal with PWM signals. The authors utilize input sensors with bandwidths in the range of tens of kHz in the publication [56] and a 150 kHz current sensor and a 500 kHz voltage sensor in [57]. The signals are sampled with 25 kHz in the case of high bandwidth sensors [57] and with 1 MHz in the case of smaller bandwidth [56]. Although, the main focus of the articles [56], [57] is on the algorithmic design of power analyzer, the large difference of the utilized bandwidth and sampling frequency indicates that its unclear which bandwidth and sampling frequency is actually required. It seems that the presented device solutions include simply the highest bandwidth and the fastest sampling frequency available in their laboratories.

The limited bandwidth of current power analyzer stem from the components of the analog part of the measurement chain. Beside this limitation a further issue exists: the frequency response of the analog part is not perfectly flat, as discussed in [43]. The imperfect flatness affects the result of the power analyzer [58]. An amplitude deviation yields to a wrong amplitude of the spectral power component, whereas a phase deviation modifies the power factor of the spectral power component. The phase deviation however affects the power factor only, if there is a mismatch between voltage and current channel, as discussed in [45]. The matching of voltage and current can be challenging, as the measurement chains are different for voltage and current. The measurement chain for the voltage channel consists typically of two voltage divider per channel and a differential amplifier stage [59], [60]. The differential stage is required as the measurement ground can differ from the power supply ground.

Simple voltage divider provide a poor frequency response flatness mainly because of parasitic capacitors. Therefore voltage divider are, similarly to voltage probes for oscilloscopes, frequency compensated. The required phase matching of voltage divider is for itself already a complex task, as a differential stage for three-phase motors requires already 6 voltage phases to be matched. The power analyzer's current measurement is mainly realized in two variants resulting from the boundary conditions: dc capability, high bandwidth and high accuracy. The first variant is the utilization of a current shunt. Current shunts can be designed with low inductance, making them suitable for measurements above the MHz range [22], [23]. Metrology laboratories utilize mainly current shunts [48], [52], [61]. As a drawback, the introduction of current shunts requires a change of the motor supply cabling making practical measurements cumbersome. Therefore, the current shunt variant is not widely used in practical measurements. Power analyzer are typically equipped with an external sensor input for arbitrary current sensors. In practical applications, the external input is often connected to a current transducer operating with a hall effect magnetometer or fluxgate magnetometer enabling galvanic insulation and contactless measurements of dc as well as ac currents. Both sensor technologies offer bandwidths up to some hundreds kHz and high accuracy. With the insight to typical sensor technologies for voltage and current, the complexity of phase and amplitude matching becomes more obvious. The matching of voltage and current path can be achieved in the analog domain by tuning the amplifier stages [43], [45] or in the digital domain by digital filters [62]–[64]. Especially the results from [63] show that digital filtering can increase the sensors bandwidth without decreasing the measurement

uncertainty. However, the article [63] contributes to grid power measurements at high voltage where an upper frequency limit of 600 Hz is standardized. Although this field of contribution is different from power measurements of electric drives, the utilized methods seem to be suitable for measurements of electric drives.

After analog processing and digitization of voltage and current, the power is computed with an appropriate algorithm. Basically, Equation (2.5) (or (2.8) for three-phase systems) has to be computed. The way of computing Equation (2.5) can be categorized into three groups: the sum can be computed directly [21], or the power can be computed by means of the DFT of voltage and current [65] or the mean value of the active power is determined by filtering the instantaneous power [57]. Under ideal conditions, all computations give the same result. In real measurement scenarios, each computation method is prone to different sources of uncertainty. The DFT method is computationally complex but it provides an advantage for frequency response compensation. A nonideal frequency response can *theoretically* be compensated by multiplying the signal spectrum with the inverse frequency response [53] of the nonideal channel. However, practical measurements of electric drives are typically corrupted by spectral leakage as the true period of the signal is not perfectly determined. In this case the frequency response compensation does not necessarily improve the uncertainty of the active power. The second method for computing the active power is the direct computation. The direct method offers the possibility of computing the power over long intervals with constant computational cost, as Equation (2.5) can be computed recursively. Therefore the computation length is just limited by the precision of the digital number format. Both, the DFT and the direct method require the determination of the signal period or a multiple of it, as it is the case in quasi-synchronous sampling [21]. The accuracy of both methods can be enhanced by utilizing suitable windowing functions as demonstrated in [53], [66]–[68]. The third method does not directly require the knowledge of an averaging interval as the active power is computed by filtering the instantaneous power [57]. A suitable designed lowpass filter can filter out frequency content except for the dc component of the instantaneous power $\bar{p}[n]$, which equals to the active power. However, the method requires the design of a suitable digital filter. The filter design implies a compromise between fast setting time and high attenuation of the signal's ripple.

To determine the signal period, mainly zero crossing based strategies are utilized. Thereby, the zero crossings of a reference signal are evaluated for its fundamental

frequency [21], [44]. The reference signal can be a voltage or current signal, a filtered version of them or the output of a PLL with voltage or current as input. The error caused by determining a wrong integration interval has been investigated in [46], [69], [70] for grid signals. Most literature concentrates on frequency and period estimation for grid signals [71]–[73]. For PWM and strong non-sinusoidal signals however, direct zero crossing detection is not suitable as the multiple zero crossings in the vicinity of a fundamental zero crossing lead to wrong results [74]. Therefore integrating zero crossing techniques are utilized for PWM signals [57]. Generally manufacturers of power analyzer reveal only portions of the power computation algorithms; the details are not published. However, the possible power analyzer's setting options indicate that the actual computation algorithm is a combination of PLL synchronization, zero crossing detection, and lowpass-filtering of the active power at the same time.

To provide reliable measurement results, power measurements have to include an uncertainty bound. The standard work for uncertainty evaluation of measurements is the *Guide to the Expression of Uncertainty in Measurement* (GUM) [75]. The GUM proposes to evaluate the uncertainty on basis of error propagation or Monte Carlo based methods. Error propagation based investigations of power measurements are treated in [43], [48], [55], [58], [76]–[81], whereas Monte Carlo based methods are rare because of the huge parameter space composed by: the voltage and current signals, transducer frequency response, sampling process and algorithm. Generally uncertainty evaluations of sample based power measurements are problematic because of the number of contributing variables. In the article [55], a detailed uncertainty evaluation description is given, considering input transducer and the data acquisition hardware. The comprehensive table [55, Table 4] summarizes the results for the uncertainty and correlation analysis for all power realted quantities defined in the IEEE Standard [20]. The defined quantities relate mainly to distorted grid line signals. PWM signals are not directly covered in the standard, as PWM signals suffer from a clear interpretation of the terms fundamental and harmonic content. Instead, PWM signals are described more meaningful in terms of a fundamental and a switching frequency.

Power measurements of electric drives with PWM signals require more attention for an uncertainty evaluation. Evaluations based on error propagation are manageable within grid line signals as the number of contributing quantities, like harmonics, is limited. Furthermore there exist commercial voltage and current calibrators for uncer-

tainty evaluations of sinusoidal signals. Switching PWM signals however cannot be generated with a calibration device and therefore computed uncertainties suffer from an experimental verification. For example in [79], the uncertainty of a designed power measurement device is evaluated by comparing its output against a commercial power analyzer with a bandwidth of 800 kHz. It is unclear if this bandwidth is sufficiently high for serving as reference result. There is no scientific literature available stating the required measurement bandwidth. In the article [82] the author analyzes different power analyzer settings for electric drives and he concludes to utilize the maximum bandwidth of a power analyzer for accurate power measurements. However, it is unclear which signal parts have a considerable contribution to power measurements and have to be included in the measurement bandwidth.

From a theoretic viewpoint, the required bandwidth of a power measurement is affected by the spectral distribution of voltage and current. The rectangularly shaped PWM voltage signal is wideband as can be seen in [18], [83], [84]. The amplitude of the voltage signal decreases asymptotically with 20 dB per decade. The current in turn results from the source voltage and the load impedance. At electric drives, the load impedance of the inverter is primarily the electric motor. The basic signal behavior of an electric motor is described as resistive inductive load [85]. PMSMs for traction drives with a power rating above some tens of kilo Watt have an electric time constant of the stator in the range of approximately 5 ms to 30 ms [86], [87], corresponding to a cutoff frequency of roughly 5 Hz to 30 Hz. The resistive inductive model describes the relationship between torque, current and voltage and the usability of this model is limited to the fundamental frequency range. Above the fundamental frequency range (some kHz) simple resistive inductive load models are not suitable. Therefore, high frequency models were developed. The developed models stem from different engineering fields like electromagnetic interference considerations [88]–[91], bearing currents of electric motors [92], [93], overvoltage studies at electric motors [94]–[96] or design of damping chokes [97], [98]. Although these articles stem from different engineering fields and contribute to different research questions, there is an agreement concerning the high frequency behavior of electric drives. At high frequencies, parasitic capacitors and inductors of motor and cabling can form a resonant circuit depending on the drive setup. The resonant frequency can range up to some 10 MHz [96], [99], [100]. The rectangular voltage signal excites the resonant circuit at each switching instant. By doing so, phenomena like ringing and voltage overshoots can occur. At industrial applications, damping circuits are mounted

for reducing voltage overshoots and ringing. The drawback of this damping circuits is, that they increase the overall losses of the drive [94], which is not desired at automotive applications. The effect on power measurements of this high frequency resonant circuits is not tackled in literature. It is obvious that the dissipating energy has an influence on the power measurement, but it is unclear to what extent the influence is and which elements are the affecting quantities in a motor drive.

To evaluate the uncertainty of power measurements a reference result of the active power is required. An intuitive approach is to measure the power sample based with the *best* measurement equipment available and to utilize the result as reference measurement. The drawback of this approach is, that currently the best available sampling equipment is not sufficiently accurate. The combination of high bandwidth up to tens of MHz, correspondingly high sampling rate, amplitude resolution and overall low level of uncertainty of voltage and current acquisition is hardly achievable with current measurement equipment. Some scientific articles contributing to power measurements suffer from a reliable reference result for evaluating their proposed design. In [56], [79] for example a power measurement device with a bandwidth lower than 100 kHz is used as reference. Therefore it is possible that the designed measurement solution gives better results as the reference, but the designed measurement solution is misleadingly interpreted as less accurate as the commercial power analyzer. A further example for an improvable reference measurement is given in [101], where the reference measurement is made with ten times the switching frequency of the inverter. Within this scenario, small voltage pulses with a duty cycle smaller than 10 % can not be acquired correctly. In the article [102], the reference measurement is obtained by a digitizing signal analyzer scope with two giga samples per second. High speed scopes however include typically only 8 bit ADCs with a correspondingly limited amplitude resolution.

To overcome the bandwidth and signal acquisition issue with PWM signals, this thesis utilizes the calorimetric approach for reference power measurements. The calorimetric approach is well established for loss measurements and it has the advantage of being free of any signal bandwidth limitation. In [103], [104] for example, a calorimetric power loss measurement serves as reference result for evaluating different techniques for power measurements. A comprehensive survey of calorimeter types, their setup and achievable uncertainties is given in [105]. Although the articles [106], [107] state that calorimetric methods are complex for power measurements, calorimeter provide a strong benefit

in terms of measurement uncertainty [107]. In [108] different calorimeter types are compared and within the range up to 1 kW closed type calorimeter are the most accurate type. Closed type calorimeter require only temperature and dc power measurements and both can be engineered with low levels of uncertainty and reasonable effort. Open type calorimeter are however more suitable for higher losses as demonstrated in [109], where power losses up to 30 kW are handled. A general drawback of calorimetric measurements is the relatively long measurement time. The long measurement time stems from the high accuracy requirement and in turn steady state temperature conditions. The time for reaching steady state results from the thermal capacity of the calorimeter and the device under test. If the thermal model of the calorimeter and the device under test is well known, the measurement time of the calorimeter can be reduced drastically. In [110] for example, the measurement time of a calorimeter is reduced by evaluating the temperature *raise* instead of the absolute value. A further example for reducing the measurement time is given in [111]. Although the power measurement range and the calorimeter's dimensions are not suitable for power measurements of electric drives, the authors of [111] are able to reduce the measurement time with control theory and a thermal model.

2.4. Summary

In summary, this review shows that electric power measurements require detailed knowledge in multiple engineering fields. This fields include signal processing techniques, hardware design of signal chains, and measurement methods for electric power. Due to the wide field, many research articles contribute in general to electric power measurements. Although the amount of research articles is large, only a few articles contribute to power measurements with a special focus on electric drives and measurement uncertainty.

In all articles with focus on electric drives, the switching frequency range is included in the measurement bandwidth. In contrast, the frequency range above is not always considered. Likewise, commercially available power analyzers can provide a bandwidth up to some mega Hertz, but the motor current sensors may limit the bandwidth of the power analyzer and almost all considered power analyzer suffer from aliasing when the highest bandwidth is selected. This review outlines that in state-of-the-art literature

there is no general understanding which measurement bandwidth is actually required for a given level of measurement uncertainty.

3

Impedance Model of Electric Drives

In this chapter, an impedance model for electric drives is presented. Power measurements are based on voltage and current signals and therefore it is important to have a simulation model for predicting the relationship between voltage and current. This relationship is modeled by lumped elements, describing the behavior of an electric motor, the cables and the inverter. The model pays particular attention to the high frequency (HF) range, i.e. above the frequency of the fundamental current. The measurements presented in this chapter were performed on an automotive hybrid electric drive.

3.1. Basic Impedance Models

Typically, simple *RL* models of electric motors approximate the dynamic behavior of mechanical torque and mechanical power sufficiently accurate [85]. For efficiency simulations of inverter driven electric motors however, these simple models can become inadequate due to their reduced nature. This inappropriateness comes even more to hand with respect to the broadband excitation due to the inverter. The switching operation in the inverter and the high fundamental frequency of the motor yield to an ac voltage signal with a theoretically infinite frequency spectrum. From a frequency analysis it can be derived that the rate of amplitude decay of the voltage signal is 20 dB/Dec (see Equation (4.7) in Section 4.3.1). This limited decay rate results in a HF excitation of the parasitic elements given by the components of the electric drive. Therefore, a simple *RL* load impedance model like

$$\underline{Z} = R_{\mathrm{M}} + \mathrm{j} \cdot 2\pi f L_{\mathrm{M}}, \tag{3.1}$$

cannot cover all effects occurring in the electric drive. Hereby R_{M} and L_{M} are the resistance and the inductance of the motor winding.

Figure 3.1 depicts an actual voltage/current measurement within a powertrain. As can be seen, the signal contains strong overshooting effects primarily caused by the inverter switching operation. The current $\hat{i}$ in Figure 3.1(b) flowing in the stray inductances and the voltage $\hat{u}$ in Figure 3.1(a) across the stray capacitances of the inverters load circuit provide the energy for the overshoots. Such effects cannot be covered by a simple load model as given by Equation (3.1). An often found approach in literature is the extension of the simple load model by stray reactances to model parasitic effects.

In this chapter, an impedance load model with focus on power measurements is presented. The presented model consists of the motor cabling and a permanent magnet synchronous motor (PMSM). A considerable amount of literature addressing the modeling of electric drives has been published, but these already suggested load models are unsatisfactory for this thesis in terms of the following points: they address the motor only [90], [100], [112], need detailed knowledge of the motor data for finite element simulations [96], or do not provide a practical parameter determination routine [99], [113]. Additionally, the already published models are mainly developed for the prediction of electromagnetic

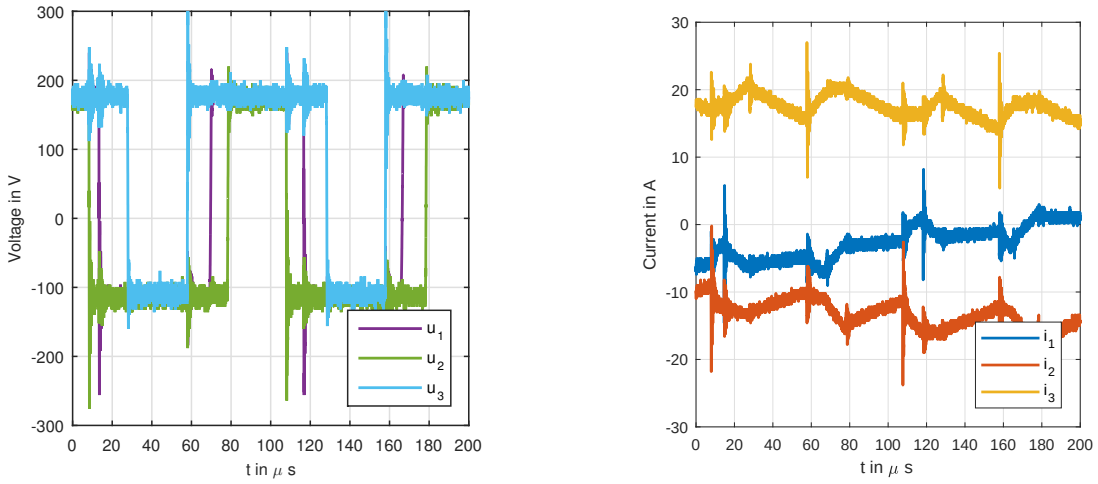

(a) Phase voltages.

(b) Phase currents.

Figure 3.1.: Actual measured current and voltage on the ac side of the inverter of an automotive traction drive. The figures show four inverter switching cycles. The phase voltages are measured against chassis ground. The offset of the phase voltages of approximately −100 V results from the voltage divider of the drive's stray impedances against chassis ground and the grounding scheme of the drive (see Figure 3.5 on page 49).

interference, bearing currents or the overvoltage phenomena. Therefore this models do not provide an optimal insight for the purpose of power measurement investigations as the model's level of detail is not sufficient. To compensate for the disadvantage, the following model augments and modifies the published impedance models to be useful for power measurement investigations. The proposed model features the following properties: the model covers resonance effects in a measurement setup, provides insight for power measurement and has a simple method for determining parameters from measured current/voltage signals.

In order to design and verify the proposed improved load model, measurements of an actual powertrain are presented and the origin of different effects, like overshoots or resonances, is investigated. The effects will be related to the parameters of the model and finally a comparison between measurement and simulation demonstrates that the model covers typical effects observed in a real system.

The remaining chapter is structured as follows. In Section 3.2 the modeling of the system components is discussed. Section 3.3 presents measurement results from an

automotive drivetrain. The simulation of the developed model is compared with the measured data in Section 3.4.

3.2. Modeling of System Components

This section discusses the behavior and modeling of the ac components of the electric drive. The components presented from Section 3.2.1 to Section 3.2.3 are given by the cable, the motor and the inverter itself. In the following sections the modeling of the individual components is discussed. The models are kept as simple as possible and provide therefore a compromise between accurate modeling of the relevant effects and simplicity of the model. After presenting the individual components, the load model is designed.

3.2.1. Model of the Shielded Cable

Due to the frequencies on the ac side of the inverter and electromagnetic compatibility (EMC) regulations, the connecting cables between inverter and motor are usually coaxial cables. As the maximum frequencies in the power circuit are in the range of some 10 MHz, and due to the limited length of the cabling it is not necessary to apply transmission line models for wave propagation. Instead, lumped element circuits can be used. This reduces the ability of the model to represent transmission line effects, but remains the electric properties of the cable in terms of equivalent impedances. As the aim is the modeling of resonance effects, these lumped element models cover all major effects. Several variations of equivalent circuit models for transmission lines are known, reaching from T-shaped, or Π-shaped circuits, to periodic variants of these circuits [114].

The model used in this work is depicted in the gray box in Figure 3.2. The modeling process shown in Figure 3.2 shows the shielded cable. It is modeled by an infinite number of cable stages consisting of a resistor, an inductance and a capacitor between the shield and the inner conductor. In the implemented cable model, the infinite number of cable stages are combined in one cable stage. Extended cable models [115] do not need to be used, as this simple structure already allows modeling of all relevant

effects. The coaxial structure of the cable might lead to the interpretation, that the cable inductance follows the formula of a coaxial structure. The formula of a coaxial structure assumes however that the current return path is the shield. This assumption is not correct for electric drives, as the predominant part of the cable current flows back in an other phase conductor and *not* in the shield. Therefore, the geometric loop inductance determines the cable inductor and not the coaxial structure.

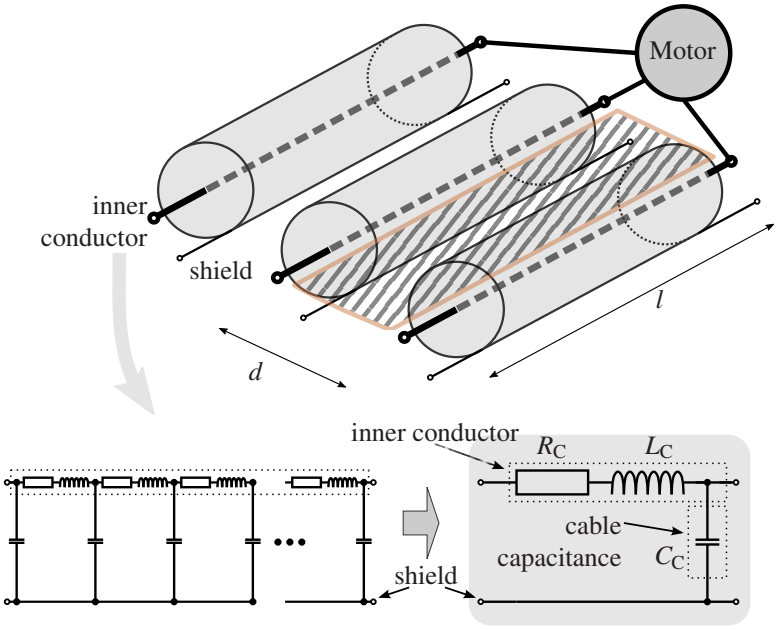

Figure 3.2.: Model of the shielded cable. The coaxial structure of the cable is represented by an infinite number of stages modeling the capacitive, inductive and resistive behavior. The stages are then approximated by the cable model highlighted by the gray background with three lumped elements. The inductor L_C models the loop-inductance of the cable, indicated by the shaded area. The resistor R_C models the resistance of the inner conductor. The capacitor C_C represents the capacitive coupling between the inner wire and the shield.

According to [116, p. 295], the self inductance of the cable L_C can be computed[1] by

$$L_C = \frac{l \cdot \mu_0}{\pi} \ln \frac{d - r_i}{r_i}, \tag{3.2}$$

where l is the cable length, μ_0 is the permeability of free space, r_i is the radius of the inner conductor, and d is the distance of the cables. It has to be noted that Equation (3.2)

[1]For the verification of an inductance calculation or measurement, the lower limit for the inductance per meter is given in the article [117] with 554 nH/m.

holds only for long cables, i.e. $d \ll l$. The resistance of the inner wire R_C is

$$R_C = \frac{l \cdot \rho}{r_i^2 \cdot \pi}, \tag{3.3}$$

where ρ denotes the specific resistance of the conductor material. The capacitance C_C is given by [118]

$$C_C = \frac{2\pi\varepsilon_{eff} \cdot l}{\ln \frac{r_s}{r_i}}, \tag{3.4}$$

where ε_{eff} is the effective permittivity of the insulator and r_s denotes the radius of the shield. For shielded cables with a foamed dielectric it is suggested to choose ε_{eff} as [115]

$$\varepsilon_{eff} = 0.83 \cdot \varepsilon_0 \cdot \varepsilon_r, \tag{3.5}$$

where $\varepsilon_0 \cdot \varepsilon_r$ is the permittivity of the insulator. The parametrization of the model can be done by consulting the data sheet of the cable manufacturer and estimating the distance of the cables d.

3.2.2. Model of the Motor Winding

Similar to different lumped element models of electric cables, also different models for motor windings exist in order to describe the load behavior of motors. Models for different motor types for use in the frequency domain [90], [100], [119], the time domain [96], and both frequency and time domain [112] have been developed. Depending on the purpose, a model has to incorporate different parasitic effects. E.g. models with the purpose of electromagnetic interference modeling include components for the representation of resonance effects. Other models include lumped representations of the skin effect. A common point of these models is the consideration of the capacitive coupling between the winding and the housing.

The generic model presented in [112] is modified for the current purpose. Firstly, iron losses are neglected as the model's purpose is to cover resonance effects in the HF range and iron losses scale with the much lower fundamental frequency. Secondly, the parasitic coupling between motor winding and housing is summarized into one capacitor C_{MH}

at the motor terminal side. The original model [112] divides the coupling into two capacitors located at the beginning and end of the motor winding. Both modifications (neglecting iron losses and introducing just one winding stray capacitor C_{MH}) increase the simplicity of the model as less parameters are required and the capability for covering resonance effects remains. The original model [112] is designated to model induction motors, but its suitability for other motor types, such as PMSMs, is presented in [90], [96], [100].

The used winding model is depicted in in the gray box in Figure 3.3. The remaining part of the figure illustrates the modeling process. The modeling starts with the physical winding in the motor embedded in the motor housing. The winding is modeled by an infinite chain of lumped element stages, where lowercase letters indicate per length quantities. The full capacitive coupling network, i.e. the capacities of each winding to all neighbouring windings and the capacities between the phases are not shown for the sake of clarity. Each stage includes a resistor r_{M} describing the low frequency resistance of the winding and a resistor $r_{\mathrm{M-HF}}$ describing high frequency resistance of the winding. The motivation of separating the low and high frequency resistance is that the high frequency resistance $r_{\mathrm{M-HF}}$ comes mainly from nonlinear and frequency dependent effects like the skin and proximity effect. The high frequency resistance $r_{\mathrm{M-HF}}$ differs therefore from the low frequency resistance r_{M} of the winding. The distributed inductors l_{M} represent the inductance of the motor winding. The capacitive coupling between motor housing (chassis ground) and motor winding is described by the capacitor c_{MH}. Within the modeling process, the parameters of the infinite chain are summarized in the resulting model with the gray background.

The parameters of the resulting model are: the resistors R_{M} and R_{MH}, the capacitor C_{MH} and the inductor L_{M}. All elements except from R_{MH} stem from the infinite chain stages. The resistor R_{MH} corresponds to the high frequency resistance $r_{\mathrm{M-HF}}$, but its position is changed to the capacitive coupling path in series with the capacitor C_{MH}. The position change has the objective to separate the low frequency and HF behavior of the motor winding model. As a result of the position change, the low frequency behavior can be described by the winding path including R_{M} and L_{M} and the HF behavior is described by the coupling path with C_{MH} and R_{MH}. The position of R_{MH} in the resulting model leads to a difference between the physical winding and the lumped element model. Physically, the resistance R_{MH} stems from the winding as illustrated in the left part in Figure 3.3. A

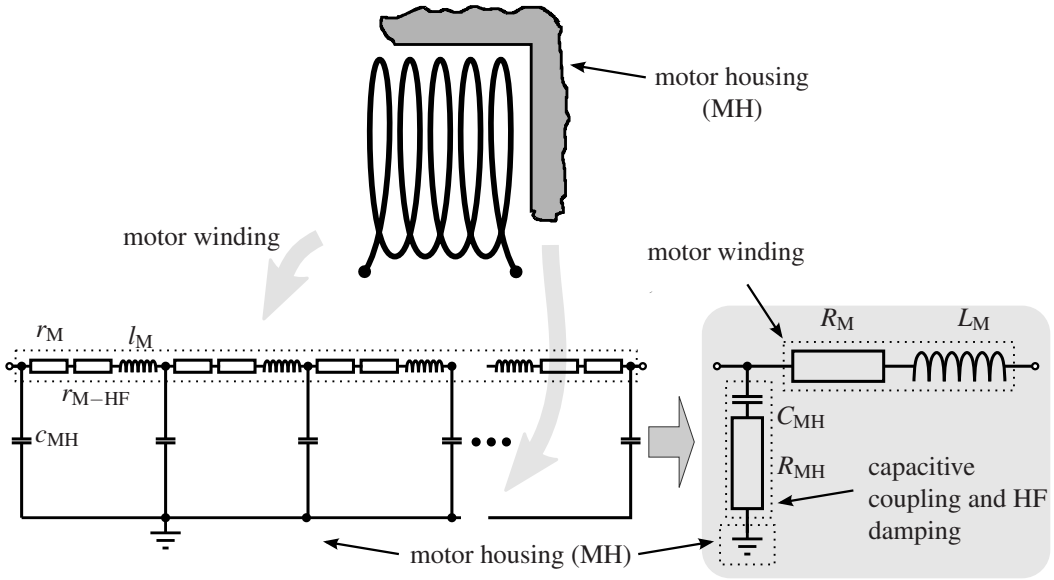

Figure 3.3.: Model of the motor winding. The modeling process starts with the actual winding within the motor housing (MH). The winding is then modeled by an infinite number of winding stages describing the resistance of the winding r_M, the high frequency resistance of the winding r_{M-HF}, the winding inductance l_M and the capacitive coupling between motor housing and winding c_{MH}. The motor winding stages are then summarized to one macroscopic lumped element model, whereby the position of the high frequency resistance r_{M-HF} is moved to the coupling path of the motor winding and results in R_{MH}. The position change separates the low and high frequency behavior of the motor winding in the model. The macroscopig elements R_M and L_M form the winding and C_{MH} represents the capacitive coupling between the motor winding and the motor housing. The resistor R_{MH} models the resistance in the coupling path of the windings and the motor housing.

further approximation of reality is the idealization of the winding inductor L_M. In reality the inductor L_M is a function of the motor current and shows saturation effects. The model neglects this dependence. The simplified model structure yields to the restriction that the model parameters are only valid in the vicinity of the investigated frequency.

The parameters of the motor winding R_M and L_M in Figure 3.3 depend on the performance rating of the individual motor. As noted before, the parameters of the capacitive coupling C_{MH} and R_{MH} result from the geometry of winding and housing of the motor. For obtaining the model parameters, it is most useful to directly measure R_M and L_M at some 100 Hz. At higher frequencies parasitic effects start to influence the

measurement.

The parametrization of the parasitic capacitive coupling is not as straightforward as for the winding. The resistance R_{MH} is mainly caused by HF effects and increases at higher frequencies. Therefore, the value of R_{MH} is a function of the frequency and must be adjusted such that the simulation matches the measurements. A direct measurement of the capacitance C_{MH} yields to similar problems. The motor geometry influences the frequency curve of the impedance between winding and housing at higher frequencies. This influence complicates the choice of a suitable measurement frequency for C_{MH} since the frequency encounters conflicting properties. On one hand the frequency has to be chosen high enough such that the measurement signals provide an adequate amplitude. On the other hand, a low measurement frequency provides a higher robustness against parasitic effects due to geometric properties of each motor. Therefore, literature suggests to solve an optimization problem, as done in [90]. These problems in the parametrization motivate the simple parameter determination method which is described in Section 3.4.

The winding model does not include the counter-electromotive force (CEMF). Usually, the CEMF is modeled by an additional rotational speed dependent voltage source. The voltage difference between inverter output and CEMF is the effective voltage which determines the current of the motor windings. The actual shape of the CEMF is determined by the motor geometry and for constant rotational speeds it is typically sinusoidal or trapezoidal. Therefore its spectrum is limited to the rotational frequency times the number of pole pairs z and a few harmonics. Consequently, including the spectrum of the CEMF voltage source in the measurement bandwidth is essential for power measurements. For sake of simplicity the CEMF is not included in the model even though it influences the power consumption of a motor decisively, but not the spectrum in the HF domain.

3.2.3. Model of the Inverter

The inverter module consists of the electronic switches providing the functionality to generate an ac voltage from the dc powered circuit. On the dc side, the inverter is equipped with decoupling capacitors reducing the feedback from the ac side to the dc side. Acting as source, the overall behavior of the inverter and the load is determined

by the source properties provided by the inverter. This comes down to the parasitic properties of the used electronic power switches which are mostly IGBT devices. The range of this parasitics can be found in the data sheets such as [120], [121].

The inductance of a typical IGBT module is mostly in the range of some 10 nH and the series resistance is in the range of some mΩ [120]. The parasitic capacitance between collector and emitter of an IGBT module is in the range of some 100 pF [121]. With respect to the impedances in the cable and the motor, the parasitic impedances of the inverter can be neglected; e.g. the parasitic capacitance between the motor winding and the housing is stated in the range of nF [90], [112], [119], forming the dominant capacitance in the system.

3.2.4. Three-Phase Model of the Output Impedance of the inverter

Assembly of the Load Model

In this subsection, the load impedance model for the specific measurement setup is presented. The following Section 3.3 presents the numeric parameter values. The schematic overview of the arrangement is depicted in Figure 3.4. As shown, the shields are connected to the inverter and motor housing. Depending on the drive scenario different schemes for connecting the shield of the cables are viable. The shield can be bonded on both ends [122] or on one end [93] to earth, depending on the suppression of radiated electromagnetic noise (both ends bonded) or the suppression ground loops (drive side bonded) [91]. The shielding scheme of the actual drive agrees with the model and the sensing location of voltage and current is in the middle of the cable.

The assembled load model will be compared with respect to the phase to phase voltages u_{12}, u_{23} and u_{31}, and phase currents i_1, i_2 and i_3 depicted in Figure 3.1. The phase voltages u_1, u_2 and u_3 in Figure 3.1(a) have an offset of approximately $-100\,\mathrm{V}$ against the measurement ground (equal to chassis ground). The offset of approximately $-100\,\mathrm{V}$ results from the grounding scheme of the drive and the insulation resistances of the drive components against chassis ground as illustrated in Figure 3.5. The insulation resistances R_{Iso+} and R_{Iso-} and the stray capacitances C_{S+}, C_{S-}, C_{S1}, C_{S2} and C_{S3} roughly summarize the physical properties of the drive in concentrated elements to explain the offset of the phase voltages u_1, u_2 and u_3. In a symmetric impedance

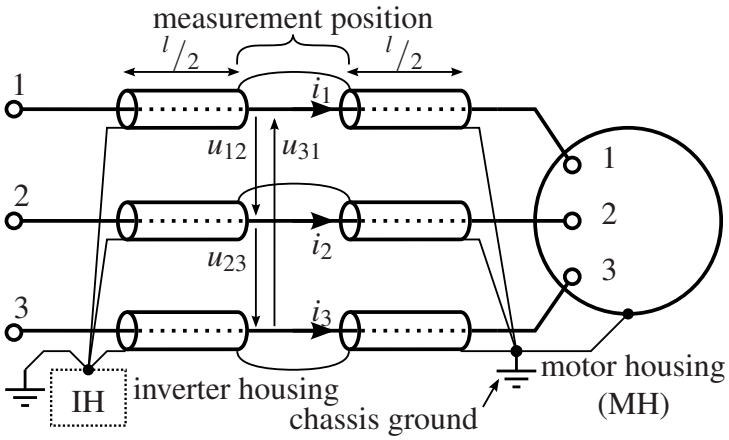

Figure 3.4.: Schematic assembly of the cables and the motor. The measurement position for voltage and the current is in the middle of the cable length l. The shields are connectet at the motor and inverter housing.

configuration, the voltage U_{+C} from the positive dc link potential to chassis ground and the voltage U_{PC} from the negative dc link potential to chassis ground would be equal to $\frac{U_{dc}}{2}$. For safety reasons, however, the power ground (PGND) is connected to the chassis via a bonding capacitor C_B and a bonding resistor R_B [12]. The capacitance C_B of the bonding capacitor is larger than the stray capacities C_{S+}, C_{S-}, C_{S1}, C_{S2} and C_{S3} and the bonding resistor R_B is smaller than the insulation resistances R_{Iso+} and R_{Iso-}. Without switching operations, the voltages from the dc link potentials to the chassis U_{+C} and U_{PC} behave according to the voltage divider formed by the bonding resistor R_B ($R_B \parallel R_{Iso-} \approx R_B$) and the upper insulation resistance R_{Iso+} [123, Annex 4A]. Since the bonding resistance R_B is typically lower than the insulation resistance R_{Iso+}, the dc part of the voltage U_{+C} is higher than the voltage U_{PC} from PGND to the housing as can be observed in Figure 3.1(a). The switching operation of the inverter causes a displacement current i_0 being relevant for the ac part of the voltage U_{PC} from PGND to chassis. The ac amplitude of the voltage U_{PC} is approximately determined by the capacitive voltage divider formed by the phases' stray capacitance C_{S1}, C_{S2} and C_{S3} and the bonding capacitor C_B. The capacitance C_B must be sufficiently large so that the ac voltage part of U_{PC} is below the limit value of 30 V_{ac} [12]. Moreover, the displacement current i_0 can shift the voltage U_{PC} out of the voltage divider ratio depending on the switching strategy and the interlocking times of the inverter phases. The diodes in the inverter rectify thereby the displacement current i_0 through the bonding capacitor C_B and the stray capacitance C_{S+} during the interlocking times, resulting in a dc voltage. It is important to note that the input impedance of a voltage probe can significantly influence

the insulation resistances R_{Iso+} and R_{Iso-}. Therefore, the voltage levels and offsets can change considerably when probes are installed. However, as all high frequency effects observed in the measured data can be described without the grounding scheme of the drive, only the phase to phase voltages are compared against each other. There are, however, combinations of earthing and cable shielding where the phase voltages must be taken into account.

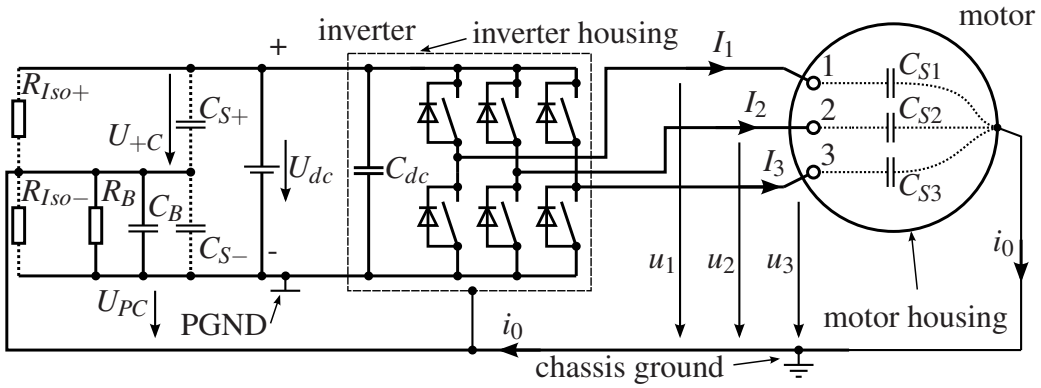

Figure 3.5.: Stray capacitances within an electric drive to explain the dc offset of the phase voltages u_1, u_2 and u_3. Dotted lines represent capacitive coupling paths or non hard-wired connections. Each motor phase is connected to chassis ground via a stray capacity C_{S1}, C_{S2} and C_{S3}. The chassis ground has a capacitive coupling to the dc link potentials via the stray capacities C_{S+} and C_{S-}. For safety reasons, the power ground (PGND) is connected to the chassis via a bonding capacitor C_B and a bonding resistor R_B.

Figure 3.6 depicts the complete model for the assembly of the devices given in Figure 3.4. The model combines the cable model presented in Section 3.2.1 and the winding model presented in Section 3.2.2. The motor windings are configured as star connection and all three phases are assumed to be symmetric. The model in Figure 3.6 includes a two-stage cable model. Generally, a two-stage model is yet not required with respect to the geometric expansion of the measurement setup discussed in Section 3.3. However, measurements of the voltages u_{12}, u_{23}, u_{31} and the currents i_1, i_2, i_3 were taken in the middle of the cable as indicated in Figure 3.6 and Figure 3.4. Therefore the two-stage model is introduced.

The points MH and IH in Figure 3.6 refer to the motor and inverter housing, respectively. MH represents the connection of all three shields on the motor housing. IH denotes the connection point of the shield on the housing of the inverter. Therefore all three phases

are jointly connected via the parasitic capacities of the cable C_C and the motor housing C_{MH} to chassis ground.

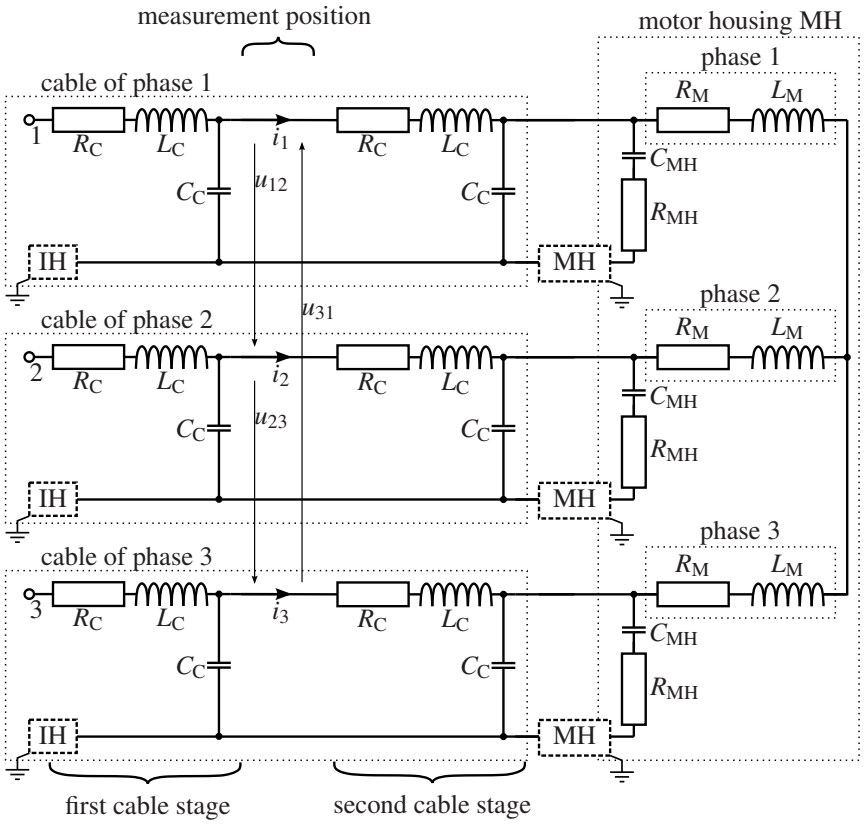

Figure 3.6.: Interconnection of cable and electric motor with the two-stage cable model. The housing of the inverter and the motor are abbreviated with IH and MH respectively. The measurement positions of the voltages u_{12}, u_{23}, u_{31} and the currents i_1, i_2, i_3 are in the middle of the cable length l.

Equivalent Resonance Impedance

Now the aim is to identify the critical components in the equivalent circuit in Figure 3.7 in order to explain resonance and overshooting effects as depicted in Figure 4.

The points $\{1,2,3\}$ in Figure 3.6 indicate the connection points to the inverter output. Apart from the time during the switching operation, two of these points are always on the same potential since the inverter is connected only to two different potentials, given by the positive and negative terminal of the dc source. Figure 3.7 illustrates the

phase configuration for phase 1 being active. For simplicity reasons the measurement positioning in Figure 3.7 is neglected and a one stage cable model is used.

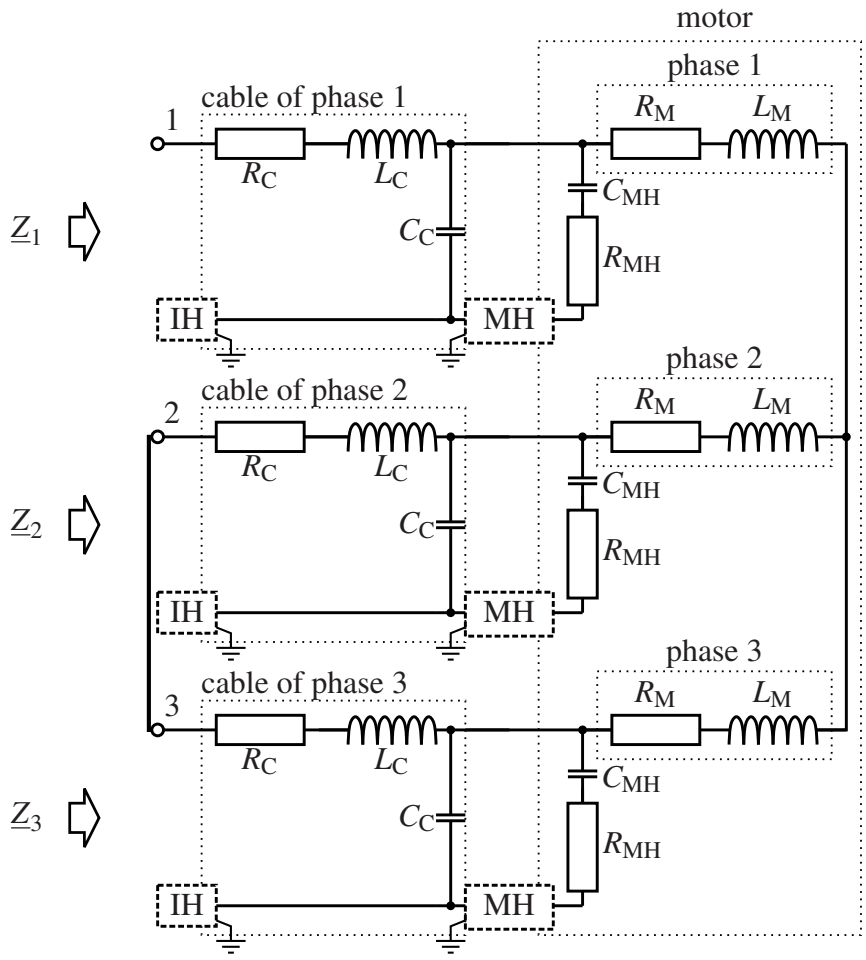

Figure 3.7.: Exemplary phase configuration of motor and cables if phase 2 and 3 are on the same potential.

The equivalent impedance $\underline{Z}_{1-23}$ between the points 1 and $\{2,3\}$ of the configuration in Figure 3.7 is given by $\underline{Z}_{1-23} = \underline{Z}_1 + \underline{Z}_2 || \underline{Z}_3$, where each $\underline{Z}_i$ presents a single phase load impedance.

Without simplifications $\underline{Z}_{1-23}$ becomes a complex expression which does not provide much insight for explaining the resonance effects. For HF signals two simplifications can be made:

- The serial impedance $R_M + j\omega L_M$ of the motor winding has a high impedance at HF and it is therefore neglected for this consideration. In reality however, the

capacitor C_{MH} is distributed across the complete motor winding (see lower left part in Figure 3.3) and currents will partially utilize the path through the winding impedance $R_{\mathrm{M}} + \mathrm{j}\omega L_{\mathrm{M}}$.

- The capacitance C_{C} between the cable shield and the cable is much smaller than the capacitive coupling between the motor and the motor housing C_{MH}. Hence, the approximated impedance for HF signals ignores the path via C_{C}.

With these two simplifications the load impedance for HF becomes approximately

$$\underline{Z}_{1-23} \approx \tfrac{3}{2}\left(\mathrm{j}\omega \cdot L_{\mathrm{C}} + \frac{1}{\mathrm{j}\omega \cdot C_{\mathrm{MH}}} + (R_{\mathrm{C}} + R_{\mathrm{MH}})\right). \tag{3.6}$$

Equation (3.6) presents an RLC series circuit which has its resonance frequency f_{res} at

$$f_{\mathrm{res}} = \frac{1}{2\pi\sqrt{L_{\mathrm{C}} \cdot C_{\mathrm{MH}}}}. \tag{3.7}$$

The oscillation frequency f_D of Equation (3.6) is (see Appendix B)

$$f_D = f_{\mathrm{res}} \cdot \sqrt{1 - \left(\tfrac{1}{2 \cdot Q}\right)^2} = \sqrt{f_{\mathrm{res}}^2 - \left(\tfrac{R_{\mathrm{C}} + R_{\mathrm{MH}}}{2 \cdot L_{\mathrm{C}}}\right)^2}. \tag{3.8}$$

Therefore, the oscillation frequency f_D differs from the resonance frequency f_{res} depending on the quality factor Q, as shown in Equation (B.17).

This analysis of the equivalence circuit offers an insight to the relevant elements, which affect the resonance. The damping is determined by the cable and motor housing resistances R_{C} and R_{MH} and the resonance frequency is a function of the cable inductance L_{C} and the capacitive coupling of the motor housing C_{MH}. Therefore, the resonance frequency of a setup with a given motor is significantly affected by the cable length l since L_{C} scales with l, as can be seen by Equation (3.2).

3.3. Measurements

This section presents the measurement setup and gives more detailed results about the appearance of resonance effects as depicted in Figure 3.1. An overview sketch of

Table 3.1.: Measured parameters of the setup. The model parameters for the simulation are determined in Section 3.4.

Quantity	Value	Comments
Cable Length l	2 m	Measuring tape; sensing location for voltage and current after 1 m.
Inner cable radius r_i	2.6 mm	Vernier caliper.
Inner shield radius r_s	3.9 mm	Vernier caliper.
Cable distance d	30 mm	Measuring tape; approximate.
Motor winding	$R_\mathrm{M} = 53\,\mathrm{m\Omega}$, $L_\mathrm{M} = 477\,\mu\mathrm{H}$	RLC bridge at 100 Hz; windings in star connection.
Motor power	80 kW to 100 kW	Estimation.
Time constant τ	740 ns	63 % time constant of the amplitude decay. Details are given in Figure B.2 in Appendix B.
Frequency f_D	2.2 MHz	Determined with the discrete Fourier Transform.

the setup and the sensing location for voltage and current is depicted in Figure 3.4. Taking the measurements in the middle position motivates the introduction of the two stage cable model as shown in Figure 3.6. Directly measured quantities of the actual electric drive are summarized in Table 3.1. Calculated quantities are presented later in Section 3.4.1.

3.3.1. Measurement Equipment

For voltage measurements, three differential probes are utilized with a bandwidth of 100 MHz (-3 dB) and a measurement range of ± 1400 V. The current probes for i_1, i_2 and i_3 are Rogowski coils with the a measurement range of ± 600 A and a bandwidth of 20 MHz (-3 dB). The large measuring range of the voltage probes and current sensors leads to a relatively large measurement uncertainty of the signals. However, the sensors were chosen because they offer a high bandwidth, which is more important than an absolute accuracy for this measuring task. The six signals are sampled using two synchronized digital sampling oscilloscopes with four channels per oscilloscope. The oscilloscopes have a bandwidth of 350 MHz and are configured with a sampling frequency of 50 MSample/s.

3.3.2. Measurement Results

The occurrence of resonance effects during the switching operation is already depicted in Figure 3.1. For a better explanation Figure 3.8 shows the same signal over one switching cycle of the inverter. As can be seen, the three half bridges of the inverter had different rise times resulting in varying amplitudes of the overshoot of the resonance. The fastest rise time in Figure 3.8 occurs at $t \approx 3\,\mu s$ while the slowest occurs at about $t \approx 15\,\mu s$. The different slopes of the signals result in distinct excitation strengths of the resonant circuit. Nevertheless, the resonance frequency remains the same.

To determine the parameters of the impedance model, two characteristic values of the overshoots are analyzed in Figure 3.8. The first parameter is the 63 % time constant τ of the amplitude decay, as described in Appendix B. The time constant τ was evaluated with Equation (B.14) and the average value of the time constant τ is 740 ns in Figure 3.8.

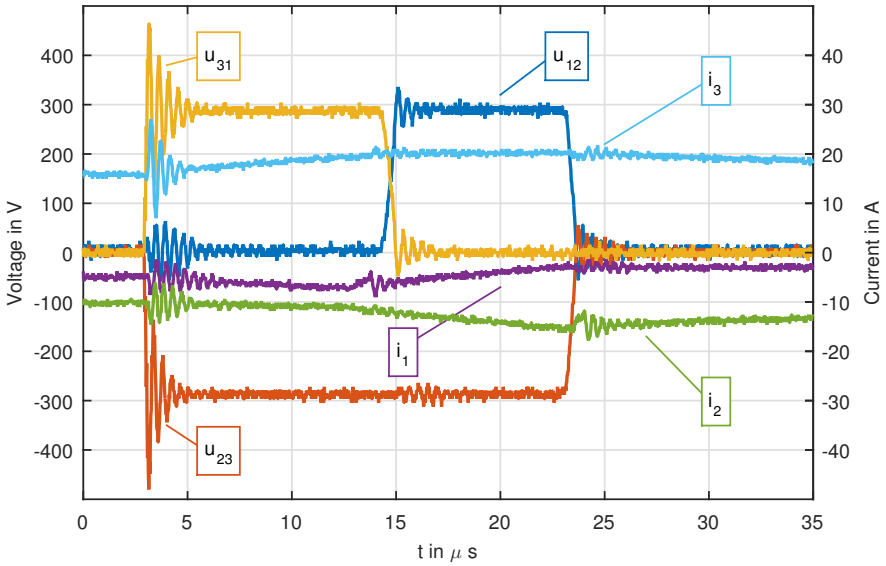

Figure 3.8.: Measured overshooting of voltage and current signal for one inverter switching cycle. The measurement-positions are explained in Figure 3.6 and Figure 3.4.

The second important parameter of the overshoots in Figure 3.8 is the oscillation frequency f_D. The discrete Fourier transform of a complete fundamental wave of sampled voltage u_{31} and current i_3 is depicted in Figure 3.9, whereas the inverter had a switching frequency of 20 kHz and the frequency of the fundamental was 300 Hz. Both

frequencies can be identified in Figure 3.9. As can be seen in Figure 3.8 and Figure 3.9, the frequency of oscillation is $f_D = 2.2\,\text{MHz}$ in both figures.

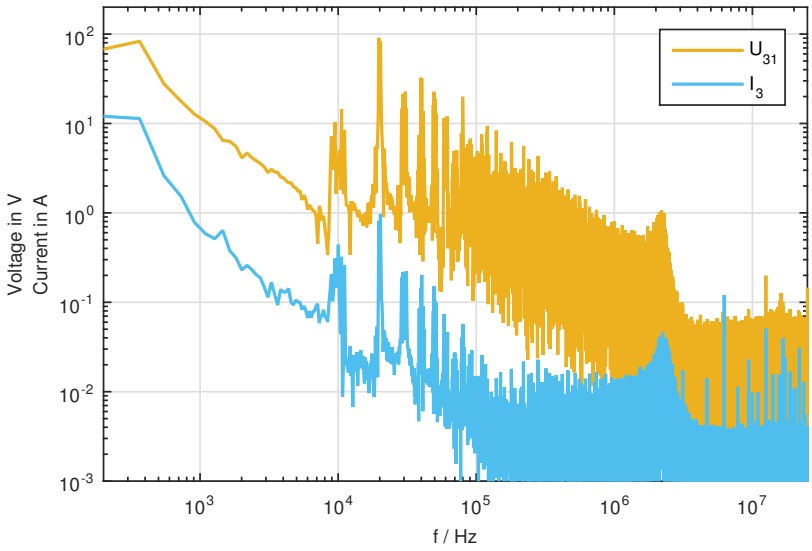

Figure 3.9.: Discrete Fourier transform of measured voltage and current. The oscillation frequency can be observed in the region around 2.2 MHz. The inverter switching frequency f_{Sw} is approximately 20 kHz.

3.4. Simulation

In this section the simulation of the transient behavior of the resonances is compared with the measurements as depicted in Figure 3.8. The SPICE simulation model is derived using the circuit depicted in Figure 3.6 and the measured parameters given in Table 3.1. The simulated transient behavior of the resonances is compared with the measurements to validate the simulation model.

3.4.1. Model Parameters

Given the data from Table 3.1 and the Equations (3.2, 3.3, 3.4, 3.5), the cable parameters are computed and summarized in Table 3.2, where the insulating material between shield and inner conductor was polyethylene with $\varepsilon_{\text{r}} = 2.4$ and $\mu_{\text{r}} = 1$.

Table 3.2.: Computed cable parameters from the data given in Table 3.1.

Equation	Quantity	Value per meter / Figure 3.6	Value for a 2 m cable / Figure 3.7
(3.2)	$L_C = \frac{l \cdot \mu_0}{\pi} \ln \frac{d - r_i}{r_i}$		
	$= \frac{l \cdot \mu_0}{\pi} \ln \frac{30\,\text{mm} - 2.6\,\text{mm}}{2.6\,\text{mm}}$	942 nH/m	1.9 µH
(3.3)	$R_C = \frac{l \cdot \rho}{r_i^2 \cdot \pi}$		
	$= l \cdot \frac{0.0175\,\Omega\,\text{mm}^2/\text{m}}{(2.6\,\text{mm})^2 \cdot \pi}$	824 µΩ/m	1.6 mΩ
(3.4)	$C_C = \frac{l \cdot 2\pi \cdot \varepsilon_{\text{eff}}}{\ln \frac{r_s}{r_i}}$		
	$= \frac{l \cdot 2\pi \cdot 2.4 \cdot 0.83 \cdot \varepsilon_0}{\ln \frac{3.9\,\text{mm}}{2.6\,\text{mm}}}$	273 pF/m	546 pF

The data in Table 3.1 and Table 3.2 define the load model apart from the capacitive coupling path between motor and motor housing. As mentioned in Section 3.2, the determination of the coupling path elements C_{MH} and R_{MH} requires more efforts. Initially, the damping resistor R_{MH} is determined from the time constant τ of the amplitude decay (Table 3.1), the cable inductance L_C (Table 3.2), and neglecting the cable resistance R_C with Equation (B.15):

$$R_{MH} = \frac{2 \cdot L_C}{\tau} = \frac{2 \cdot 1.9\,\mu\text{H}}{740\,\text{ns}} = 5.1\,\Omega. \tag{3.9}$$

This value seems reasonable with respect to values found in literature for comparable machines [112]. By comparing the obtained value with the cable resistance R_C and the motor winding R_M, it turns out that R_{MH} is the dominating damping resistance of the resonance circuit indicated by Equation (3.6). The model resistor R_{MH} stems physically from the *additional* high frequency resistance of the motor winding, mainly due to the skin- effect. The high frequency hypothesis is supported by evaluating the increase of the the motor winding resistance R_M due to the skin effect at the frequency of the oscillation f_D=2.2 MHz. The true wire cross section of the motor winding is unknown.

However, if a wire cross section of $16\,\mathrm{mm}^2$ is assumed, the motor resistance R_M increases by a factor of 26 to $1.4\,\Omega$ at 2.2 MHz (see approximate skin effect formulas in [124, Chapter 29.1]). Therefore it can be stated that approximately 30 % of the resistor $0.3 \cdot R_\mathrm{MH}{=}1.5\,\Omega$ are caused by the skin effect of the *motor* winding. The remaining 70 % of the resistor R_MH can be argued by the increase of the *cable* resistance R_C due to the skin effect, the resistance increase due to the proximity effect at the resonance frequency f_res=2.2 MHz and due to imperfect modeling.

Then, C_MH is computed by Equation (B.18):

$$C_\mathrm{MH} = \frac{1}{L_\mathrm{C} \cdot \left((2 \cdot \pi \cdot f_D)^2 + \frac{1}{\tau^2} \right)} = \frac{1}{1.9\,\mu\mathrm{H} \cdot \left((2 \cdot \pi \cdot 2.2\,\mathrm{MHz})^2 + \frac{1}{(740\,\mathrm{ns})^2} \right)} = 2.7\,\mathrm{nF}. \tag{3.10}$$

A comparison of the calculated value of C_MH to values in literature for comparable machines [90], [112] shows that the result seems to be reasonable.

3.4.2. Transient SPICE Validation

Given all values from Table 3.1, Table 3.2 and the determined values for C_MH and R_MH a transient SPICE simulation for the load model is performed and depicted in Figure 3.6. The simulation result depicted in Figure 3.10 illustrates that the model is capable to cover resonance effects as shown in the measurements in Figure 3.8. The frequency of the simulated overshoots meets the measurement. The amplitude of the overshoots does not perfectly match the measured values because of the modeling imperfections discussed in Section 3.4.1. However, this result demonstrates that the combination of the cable and the motor model together provide a reasonable load model to explain occurring resonance effects due to the cable and the motor parasitics.

3.5. Summary

In Chapter 3 a load model for inverter driven motors is presented. The model combines the cabling and the motor's winding model. Because of the incorporation of the winding

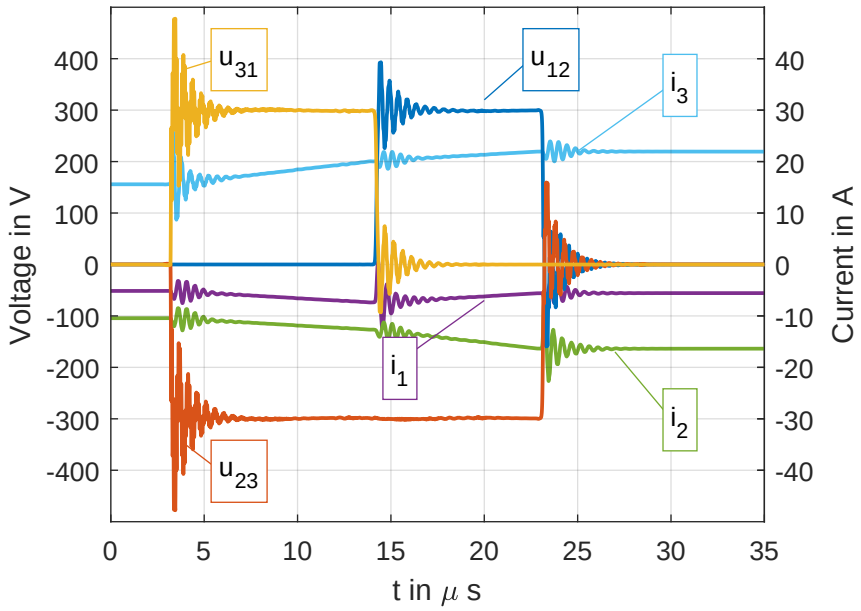

Figure 3.10.: Simulated overshooting of voltage and current — all phases.

parasitics, occurring resonance effects are covered by the model. The winding model provides a compromise between physical modeling accuracy and simple structure. In the proposed model the simple structure is preferred, as the simple model structure is able to approximate the occurring resonance effects sufficiently accurate. In addition, the simple structure allows for an informative analysis in the following Chapter 4, which discusses the implications for electric power measurements.

Most model parameters can be measured directly or can be computed by simple formulas. The parametrization of the impedance between motor housing and motor winding however raises difficulties if an impedance analyzer measurement is not possible. Therefore a simple procedure to estimate the capacitive coupling and the damping resistance from measurements is provided.

The capacitive coupling C_{MH}, the damping resistor R_{MH} and the cable inductance L_{C} influence the resonance considerably. For describing the resonance concisely, simple formulas are provided for describing the three-phase model with a simplified equivalent impedance.

4

Bandwidth Limitation Investigation

In this chapter the required bandwidth for power measurements of electric drives is analyzed. The analysis is carried out by simulations and the utilized method was originally published in [**6**]. In comparison to Chapter 3 (80 kW motor, see Table 3.1) the simulations refer to an industrial 10.4 kW machine used in an automotive drive system. The chapter is structured as follows: Section 4.1 continues with a problem description and Section 4.2 reviews the theoretical background for evaluating a bandwidth limitation. Section 4.3 explains the setup of the electric drive and the excitation PWM voltage signal. The numerical study in Section 4.4 illustrates the usage of the proposed method and identifies critical quantities.

4.1. Problem Description

As the inverter of an electric drive operates with electronic power switches, the voltage signal can be considered as a series of almost rectangular pulses. A consequence of the steep slopes is a theoretically infinitely extended bandwidth of the voltage signals. The pulses provide a limited bandwidth due to the limited slew rate, as the inverter's IGBTs act like a current source in fully conducting mode. The difference between the theoretic and practical pulse shapes will be discussed later in Section 4.3.1. As real world measurement devices provide a limited bandwidth as well, measurements of this signals may be corrupted by a bandwidth limitation as well if the measurement bandwidth is smaller than the one from the device under test. Figure 4.1 illustrates a power measurement setup, where all devices with a possible bandwidth limitation are encircled. Using the bandlimited signals for power calculations will then result in a difference between the true and computed power. Accurate measurements of the electric power require a suitable analog bandwidth of the measurement devices such that the influence of a bandwidth limitation is sufficiently small.

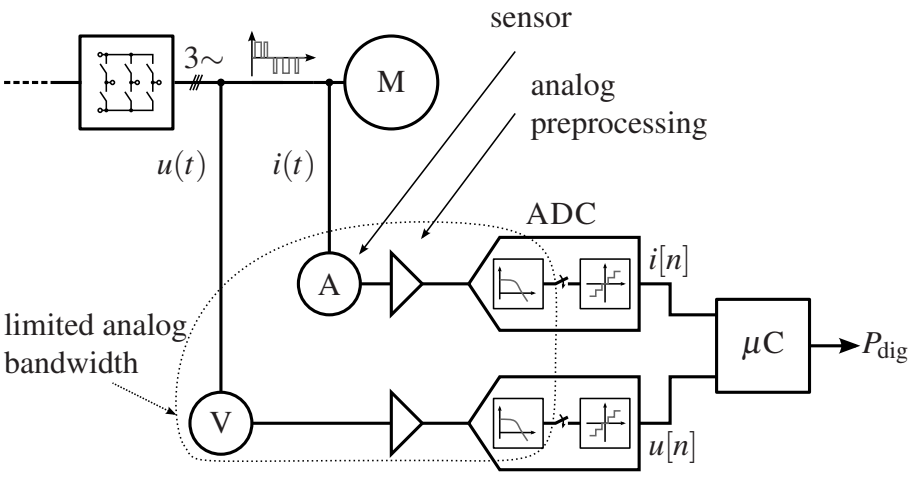

Figure 4.1.: Setup for power measurements between motor and inverter. All analog processing steps, i.e. from the sensor to the quantization step in the ADC, have a limited analog bandwidth and thus may reduce the power measurement accuracy.

Even though the influence of the bandwidth limitation is obvious, literature on power measurements pays minor attention to it. In most articles on power measurements,

the analog measurement bandwidth is chosen to be the highest possible bandwidth of the power measurement device. For example in [62] a measurement bandwidth of 100 kHz is used for the developed power measurement device for power grid signals. Similarly, in [80] and [125] the developed devices provide a measurement bandwidth above 500 kHz for power measurements at the power grid. These research articles indicate the trend of using the highest available measurement bandwidth for power metering, even in the case of less critical power grid signals. In the field of variable speed drives this trend is present too: in [79] for example a 600 kHz measurement bandwidth is used to measure the power of PWM signals. The articles [56], [77] give some rare statements concerning the bandwidth: both articles suggest a bandwidth of some tens of kHz. In contrast, the article [57] recommends a bandwidth of 1 MHz. Similarly, a bandwidth of 1 MHz is indirectly suggested in [52] as a precision power meter is characterized up to 1 MHz. However, none of these articles provide a quantitative statement concerning the required bandwidth to obtain a given accuracy of the measurement devices. The previous chapter and scientific literature on electric drives indicate, that an electric motor and its cabling can form a resonant circuit with resonant frequencies in the range of some MHz [94], [97], [126]. Resonant frequencies in this frequency range require an investigation which spectral components have a considerable effect on a power measurement in an electric drive.

Motivated by the lack of investigation in literature on the bandwidth error, this chapter combines the bandwidth evaluation method presented in [**5**] with a realistic model of an electric drive from Chapter 3.

4.2. Power and Error Definition

This section describes the computation of the electric power for the case of periodic signals and defines the error metric for the evaluation of the bandwidth limitation. The provided theory is applied to the specific scenario of an electric drive in Section 4.3.

4.2.1. Definition of Power for the Periodic Case

The average electric power P is defined by the average of voltage $u(t)$ times current $i(t)$, as described in Equation (2.2). If $u(t)$ and $i(t)$ are periodic with period T, it is possible to express the time signals as a Fourier-Series (FS):

$$u(t) = \sum_{k=-\infty}^{\infty} \underline{U}_k \cdot \mathrm{e}^{\mathrm{j}\frac{2\pi}{T}\cdot k\cdot t} \qquad i(t) = \sum_{k=-\infty}^{\infty} \underline{I}_k \cdot \mathrm{e}^{\mathrm{j}\frac{2\pi}{T}\cdot k\cdot t}, \tag{4.1}$$

where $\underline{U}_k$ and $\underline{I}_k$ are the complex FS coefficients of voltage and current.

In the FS domain, the power P is computed by summing the FS coefficients $\underline{U}_k$ and $\underline{I}_k$ instead of an average value computation in the time domain:

$$P = \lim_{K\to\infty} 2 \cdot \sum_{k=1}^{K} \mathrm{Re}(\underline{U}_k \cdot \underline{I}_k^*), \tag{4.2}$$

where $(.)^*$ denotes the complex conjugate. In Equation (4.2) and throughout the chapter it is assumed that the dc components of voltage and current are zero as they are eliminated by the control algorithm in order to prevent iron saturation.

4.2.2. Bandwidth Limitation Error

Interpreting the bandwidth limitation in power calculations as a truncation of the infinite sum in Equation (4.2) yields the bandlimited power $P(f_\mathrm{a})$:

$$P(f_\mathrm{a}) = 2 \cdot \sum_{k=1}^{K} \mathrm{Re}(\underline{U}_k \cdot \underline{I}_k^*) \qquad f_\mathrm{a} = \frac{K}{T}, \tag{4.3}$$

where f_a is the analog bandwidth up to which signal components are considered. If the true signal bandwidth exceeds f_a, then the band limitation introduces a power calculation error.

In order to evaluate the error caused by the bandwidth limitation, a comparison of the bandlimited power $P(f_\mathrm{a})$ against the true power P would be required. However, a computation of the true average power P in (4.2) would require an infinite number of FS coefficients and is therefore not feasible. Instead of comparing results of (4.3) against

the true power P, the power $P(f_\mathrm{a})$ at an appropriately high analog reference bandwidth $f_\mathrm{a,ref}$, denoted as P_ref, is used as reference:

$$P_\mathrm{ref} = P\big(f_\mathrm{a,ref}\big)\,. \tag{4.4}$$

The reference bandwidth $f_\mathrm{a,ref}$ has to be chosen such that the difference between the true power P and the reference power P_ref is negligibly small. As the true power P is not available, the reference frequency $f_\mathrm{a,ref}$ can be chosen such that increasing it does not notably modify the reference power P_ref. A further more practical possibility for choosing a reference frequency is setting it a few times beyond the highest frequency at which a contribution to the power is expected. This approach is similar to the approach found in research articles focusing on power measurements such as [101]. Within the following simulations, however, the highest contribution is determined by the simulation model and can therefore be predicted accurately.

The measurement error $E_\mathrm{abs}(f_\mathrm{a})$ and $e_\mathrm{rel}(f_\mathrm{a})$ express the difference between the bandlimited power $P(f_\mathrm{a})$ and the reference power P_ref. The relative error $e_\mathrm{rel}(f_\mathrm{a})$ is defined as the relative deviation of the absolute error $E_\mathrm{abs}(f_\mathrm{a})$:

$$E_\mathrm{abs}(f_\mathrm{a}) = P_\mathrm{ref} - P(f_\mathrm{a}) \tag{4.5}$$

$$e_\mathrm{rel}(f_\mathrm{a}) = \frac{E_\mathrm{abs}(f_\mathrm{a})}{P_\mathrm{ref}} = \frac{P_\mathrm{ref} - P(f_\mathrm{a})}{P_\mathrm{ref}}. \tag{4.6}$$

As the power is calculated with FS coefficients, the error definition has the advantage of being analytically exact up to the bandwidth of the reference power with a simple summation.

4.3. Measurement Model

This section presents the modeling of an electric drive concerning the load impedance seen from the inverter and the excitation voltage signal resulting from controlling the electric motor by a PWM inverter.

4.3.1. PWM Voltage Signal

Electric automotive drive systems are typically controlled by an FOC algorithm, which steers the switching pattern of the six switches per inverter cycle period such that the torque or rotational speed of the motor meets the set point. Steady state conditions of the drive, i.e. constant load torque and rotational speed, and an operating point within the linear modulation range of the SVPWM imply an approximately sinusoidal shape of the motor currents per phase. Therefore, the three voltage signals resulting from the switching pattern of the inverter can be described as a three level PWM signal with a sinusoidal modulation signal [**5**], [83], [127]. The relationship between PWM voltage signal and sinusoidal motor current is idealized in this simulations such that the motor inductor L_{M} is constant and no function of the motor current, as already noted in Chapter 2. In reality, however, the relationship is nonlinear as the core material may saturate.

Power calculations can be done conveniently in the frequency domain. Therefore an FS representation of the voltage signal is required. There exist several methods for the computation of the frequency spectrum of PWM signals. These methods range from the historical double FS method [128, Chapter 17] to more advanced methods like those in [83]. However, the resulting formulas of these approaches do not allow for an insightful bandwidth interpretation because of their complexity. Therefore, the FS coefficients of the voltage are computed directly by superposing shifted and scaled rectangular pulses like illustrated in Figure 4.2. The superposition represents the PWM signal, where the FS of one pulse $\underline{U}_{\mathrm{Pulse}}(k)$ (see Figure 4.2) can be computed analytically with

$$\underline{U}_{\mathrm{Pulse}}[k] = \frac{A}{2\pi \cdot k} \cdot \left(\cos\left(\frac{2\pi k}{T} t_1\right) - \cos\left(\frac{2\pi k}{T} t_2\right) + \mathrm{j}\sin\left(\frac{2\pi k}{T} t_1\right) - \mathrm{j}\sin\left(\frac{2\pi k}{T} t_2\right) \right). \tag{4.7}$$

The computation of the FS coefficients $\underline{U}_{\mathrm{Pulse}}[k]$ in Equation (4.7) can be optimized for a faster computation. The most time consuming computation step of Equation (4.7) are the multiple sine and cosine computations. For speeding up this computations,

Chebyshev's recursive method is applied:

$$\cos(k\cdot a) = 2\cdot\cos(a)\cdot\cos((k-1)\cdot a) - \cos((k-2)\cdot a) \quad \forall \quad k\in\mathbb{N} \quad k\geq 2 \tag{4.8}$$

$$\sin(k\cdot a) = 2\cdot\sin(a)\cdot\sin((k-1)\cdot a) - \sin((k-2)\cdot a) \quad \forall \quad k\in\mathbb{N} \quad k\geq 2 \tag{4.9}$$

With equations (4.8) to (4.9) it is possible to compute the sine and cosine values for all k in Equation (4.7) by evaluating the trigonometric functions for the first two ks only and the remaining terms by recursion. For applying the recursion to Equation (4.7), the term a has to be substituted by $\frac{2\pi t_1}{T}$ and $\frac{2\pi t_2}{T}$ such that Equation (4.7) is evaluated by two recursive expressions for the sine function (4.9) and two recursive expressions for the cosine (4.8) .

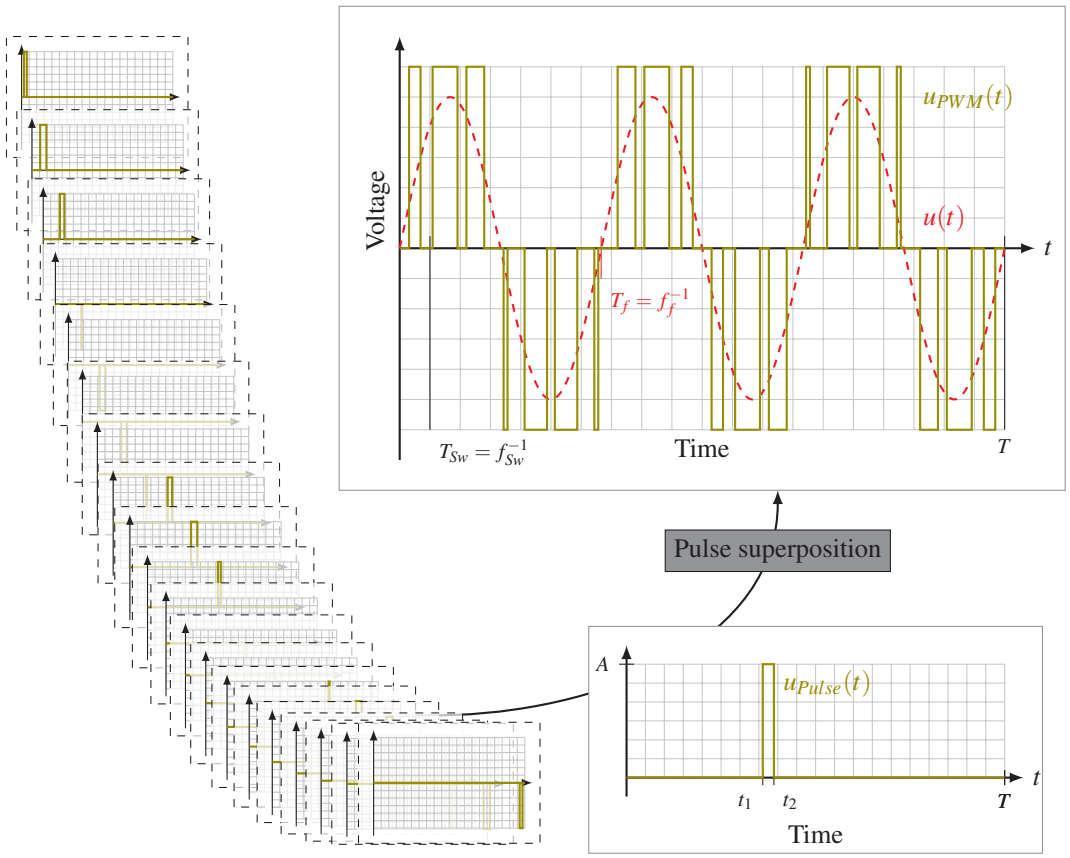

Figure 4.2.: PWM voltage signal represented as superposition of scaled and shifted rectangular pulses $u_{\text{Pulse}}(t)$. For the FS representation the spectrum of each rectangular pulse is computed analytically and the superposition of all spectra yield to the FS. The PWM method shown is asynchronous, since the pulse train is not the same for all fundamental periods.

The analytic computation method with Equation (4.7) provides the possibility of modeling a variety of different PWM strategies since they only affect the scaling and shifting of the pulses. The implemented PWM strategy is of the asynchronous type. In asynchronous PWMs, the switching frequency f_{Sw} is fixed and not synchronized with the fundamental frequency f_{M}. Therefore, the number of switching pulses per fundamental period f_{M} can be a *non-integer* number causing subharmonics. In a practical PWM implementation, the switching frequency f_{Sw} can be synchronized with the fundamental frequency f_{M} to avoid subharmonics and possible iron saturation. As mentioned in Chapter 2, iron saturation is not implemented in the simulation model and therefore only the overall periodicity of the PWM signal is taken into account. In order to avoid the problem of aperiodicity, the fundamental frequency f_{M} and the switching frequency f_{Sw} are limited to be *rational* numbers $\mathbb{Q}$. In case of rational numbers for the fundamental frequency f_{M} and the switching frequency f_{Sw}, a common signal period T does *always* exist, as both frequencies fulfill the following relations:

$$T = \frac{M_{\mathrm{Sw}}}{f_{\mathrm{Sw}}} \qquad \wedge \qquad T = \frac{M_{\mathrm{M}}}{f_{\mathrm{M}}} \qquad M_{\mathrm{Sw}}, M_{\mathrm{M}} \in \mathbb{N} \qquad f_{\mathrm{Sw}}, f_{\mathrm{M}} \in \mathbb{Q}, \tag{4.10}$$

where M_{M} and M_{Sw} are the number of periods of the fundamental motor current and and the inverter switching respectively. The limitation to rational numbers guarantees the periodicity of the voltage signal and therefore the existence of an FS representation. The PWM strategy at an actual inverter can result in a broader range of periodicities. If a fixed pulse number per fundamental period is implemented ($M \cdot f_{\mathrm{Sw}} = f_{\mathrm{M}}, M \in \mathbb{N}$), then the period of the PWM voltage signal is the same as the fundamental period. A randomized switching frequency for the suppression of acoustic noise or DTC will yield to a non-periodic PWM voltage signal. In an actual measurement however, the aperiodicity issue can be resolved by choosing a long integration interval.

Although the computation is optimized by applying Chebyshev's recursion, the drawback in form of computational complexity remains: calculating the FS coefficients of a PWM signal up to 10 MHz with a common period of $T = 10\,\mathrm{s}$ and $200 \cdot 10^3$ pulses takes approximately one day on an *Intel*® CPU with 24 GiB RAM and 3.2 GHz frequency. Advantages of the direct computation are the insightful interpretation of the bandwidth and the straight implementation.

Modeling the PWM voltage signal of the motor with perfectly sharp edged pulses

corresponds to a worst case scenario, since sharp edges extend the bandwidth of a signal to infinity. Real world PWM pulses however, have always a nonzero rise time. Automotive inverters use typically IGBTs, providing a rise time in the range of approximately 50 ns to 70 ns [120]. This leads to a trapezoidal shape of the pulses as illustrated in Figure 4.3(a). The difference between the rectangular modeling and trapezoidal reality is clarified by comparing the FS coefficients of the waveforms. Therefore Figure 4.3(b) shows the *absolute values* of the FS coefficients, where all waveforms have the same amplitude, a 50 % duty-cycle and a fundamental frequency of 20 kHz. The trapezoidal waveforms provide rise times of 50 ns and 70 ns. As depicted in Figure 4.3(b), the amplitude of the trapezoidal FS coefficients agree with the rectangular waveform for frequencies up to approximately 2 MHz. By comparing the amplitudes at higher frequencies, it can be seen that the rectangular coefficients are larger than the trapezoidals, where the faster 50 ns rise time results in a smaller deviation. The deviation between the envelope of the trapezoidal and rectangular amplitudes increases with 20 dB/Dec starting at approximately 2 MHz. However, as the amplitudes at this frequency ranges are already smaller than −40 dB, their overall contribution is limited. Modeling the PWM voltage with rectangular pulses is therefore a suitable worst case scenario.

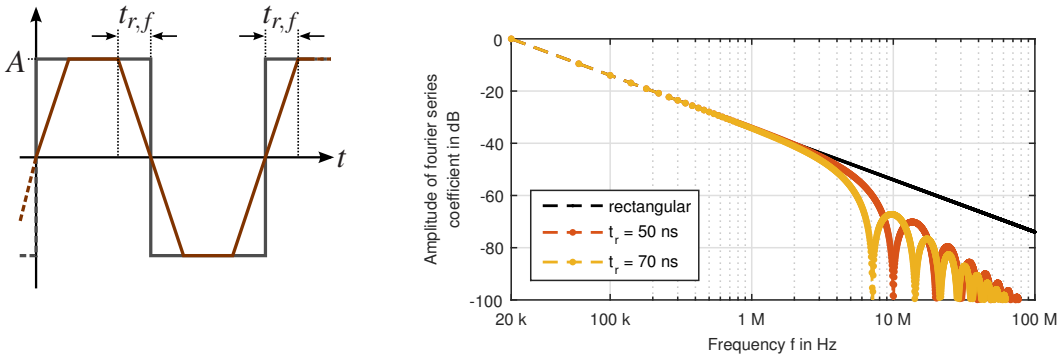

(a) Waveforms.

(b) Magnitude of the FS coefficients of a rectangular and a trapezoidal waveform.

Figure 4.3.: Difference in spectrum between rectangular and trapezoidal waveforms. The waveform has a fixed switching frequency of 20 kHz, a duty cycle of 50 % and the same amplitude A in all cases. The rise and fall time $t_{r,f}$ of the two trapezoidal waveforms in (b) are 50 ns and 70 ns. As can be seen in the spectrum, the magnitude of the three waveforms starts to deviate at approximately at 2 MHz.

A further modeling idealization concerns the maximum and minimum pulse width of the

PWM pulses. In the model the PWM voltage signal can represent arbitrary pulse widths from 0 % to 100 % of the switching period. In reality, the IGBT requires a minimum time delay between two subsequent switching actions. The minimum time delay lies in the range of some µs [129, p. 34]. Therefore, short pulses with a duty cycle of some % and long pulses with almost 100 % can not be generated and the actual voltage signal will consist of less pulses as in the simulation. The simulation represents therefore a worst case scenario, as the HF excitation occurs less often.

4.3.2. Load Impedance Model

Evaluating the effect of a bandwidth limitation on a power measurement requires an impedance model of the electric drive as it connects the generated voltage signal with the current signal. As high frequency (HF) components are included in the PWM voltage signal, the impedance model has to be suitable for frequencies beyond the fundamental frequency of the motor current f_{M}. Therefore the impedance model presented in Chapter 3 is utilized.

The motor winding is modeled as a resistor–inductor series impedance with the resistor R_{M} and inductor L_{M} and a capacitor C_{MH} in series with a resistor R_{MH} representing the coupling path between the motor housing and the motor winding as can be seen in Figure 3.3 (see Chapter 3).

The cable is modeled as a shielded cable with a coaxial structure as shown in Figure 3.2. The cable model is parametrized by the capacitance between shield and inner conductor C_{C} (Equation (3.4)), the cable loop inductor L_{C} (Equation (3.2)) and the cable resistor R_{C} (Equation (3.3)).

The assembly of the three-phase motor and cable model is presented in Figure 4.4. As an evaluation of the complete three-phase system shown in Figure 4.4 is due to its complexity not effective, the equivalent impedance between one phase and the connected remaining phases is analyzed. The single phase impedance offers the same impedance characteristic like the complete model, as two phases are always at the same potential during normal operation as the inverter can only switch between the positive and negative dc power supply voltage input. The reduced equivalent impedance, denoted as $\underline{Z}_{1-23}$, covers two aspects of the electric drive. Firstly, $\underline{Z}_{1-23}$ covers the

torque-generating part, modeled by the motor winding with R_M and L_M and secondly, it covers all parasitic effects represented by the remaining elements.

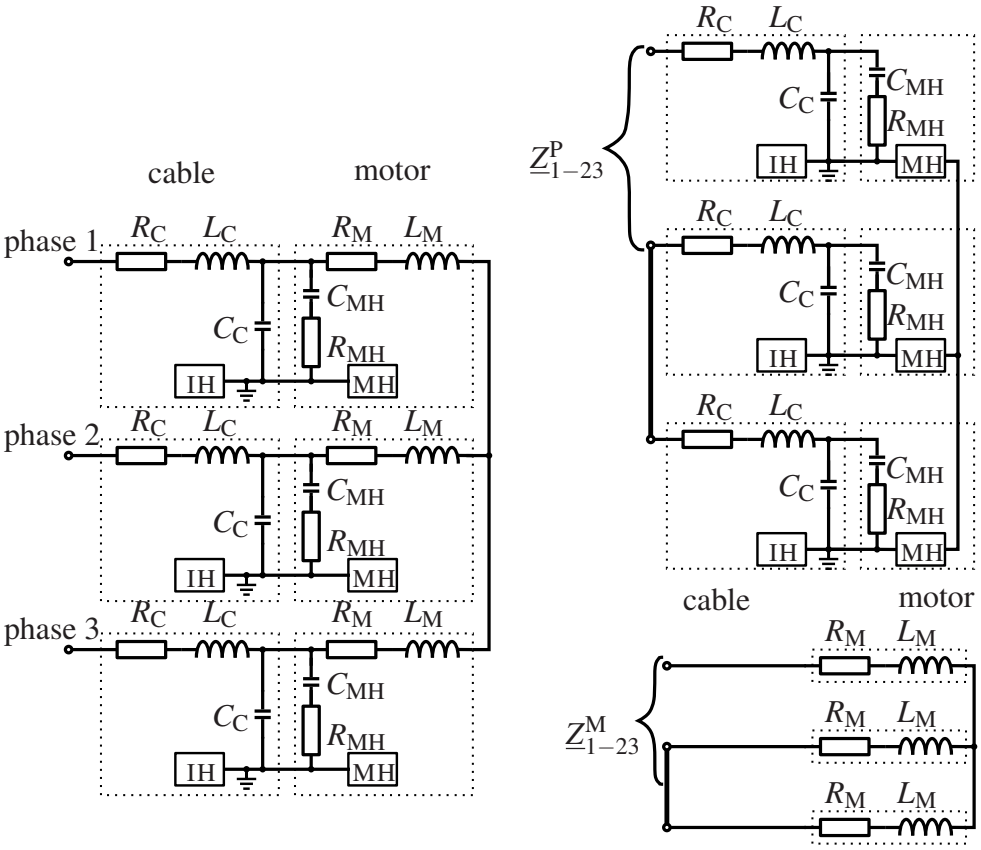

Figure 4.4.: Equivalent impedances for different purposes. On the left hand side is the torque-producing *and* parasitic part of the drive. For the sake of clarity, connections internal to the motor housing (MH) or the internal to the inverter housing (IH) are not always shown. The upper right hand side shows the impedance of the parasitic part $\underline{Z}^P_{1-23}$ and the lower right hand side shows the torque-producing part $\underline{Z}^M_{1-23}$.

These two parts are affected differently by the motor operating point, i.e. the load torque and rotational speed: in reality the winding part produces the mechanical torque and is therefore strongly affected by the CEMF voltage source, which is, as already explained, not included in the model. In contrast, the power dissipation in the parasitic part is determined by the voltage level of the dc voltage supply, the switching frequency and the resonant frequency of motor cabling and winding. The switching frequency acts linearly on the power dissipation, as it determines how often the resonant circuit is excited per time unit. The voltage level of the dc supply increases the power dissipation

quadratically, as the voltage level determines the energy stored in the resonant circuit. The motor current does hardly influence the energy dissipation as it is approximately constant before and after the resonant effect (compare Figure 3.1(b) and Figure 1.3(a)). Therefore the energy stored in the cable inductance is constant before and after a switching action. A consequence of this difference is a stepwise evaluation of the impedance: first the torque-generating and parasitic parts are evaluated separately and then the complete impedance is evaluated. The two impedances are denoted as $\underline{Z}^{\mathrm{P}}_{1-23}$ and $\underline{Z}^{\mathrm{M}}_{1-23}$ for the parasitic and torque-producing parts respectively and $\underline{Z}_{1-23}$ denotes the complete impedance.

As described in Chapter 3, the parasitic impedance $\underline{Z}^{\mathrm{P}}_{1-23}$ forms a series resonance circuit. The cable inductance L_{C} and the capacitance in the motor housing C_{MH} influence the resonant frequency f_{res}, which is $f_{\mathrm{res}} = \frac{1}{2\pi\sqrt{L_{\mathrm{C}} \cdot C_{\mathrm{MH}}}}$ (Equation (3.7)). The resistor R_{MH} models the damping of the resonant circuit and therefore strongly affects the rate of amplitude decay of the parasitic impedance $\underline{Z}^{\mathrm{P}}_{1-23}$ within the simulation.

4.4. Numerical Study

This section provides a numerical example illustrating the evaluation of the bandwidth limitation error.

To point out the practical relevance of the following results, they are put in contrast with a target uncertainty e_{tar} of a power measurement. Therefore the scenario of evaluating the efficiency η_{inv} of an inverter is considered. Given the definition of the efficiency in general and an assumed inverter efficiency of η_{inv}=95 %, the error bounds can be derived by error propagation at a desired efficiency uncertainty of $\Delta\eta_{\mathrm{inv}}$=0.5 % as

$$\eta_{\mathrm{inv}} = \frac{P_{\mathrm{out}}}{P_{\mathrm{in}}} \qquad \left|\frac{\Delta\eta_{\mathrm{inv}}}{\eta_{\mathrm{inv}}}\right| = \left|\frac{0.5\,\%}{95\,\%}\right| = 0.5\,\% \leq |e_{\mathrm{in}}| + |e_{\mathrm{out}}|\,, \tag{4.11}$$

where e_{in} and e_{out} are the uncertainties of the dc input power P_{in} and the ac output power P_{out}. The uncertainty is derived by error propagation. The results illustrate the order of magnitude of the uncertainties. Some power analyzer manufacturers [31] utilize the worst case uncertainty too, which is equivalent to the uncertainty obtained by error propagation. Current power analyzer provide an uncertainty for dc power

in the range of 0.1 % [130]. The input power P_{in} of the inverter is a dc quantity and therefore the measurement uncertainty of the input power e_{in} is 0.1 %. Consequently, the measurement uncertainty e_{out} of the inverter's ac output power has to be smaller than $e_{\text{out}} \leq 0.5\,\% - 0.1\,\% = 0.4\,\%$ for keeping the desired uncertainty of the inverter efficiency $\Delta\eta_{\text{inv}}$=0.5 % (see Equation (4.11)). The relation between the resulting uncertainty of the power and the various uncertainties of sensors, the measurement chain, algorithms and the bandwidth limitation of the complete measurement chain is a complex matter [77], [80], [125]. The effect of a bandwidth limitation is therefore roughly estimated with an intuitive and practical engineering approach: splitting the uncertainty budget of 0.4 % equally among the sensor, measurement chain, algorithm and bandwidth limitation leads to the target uncertainty of the bandwidth limitation of $e_{\text{rel,tar}}$=$1 \cdot 10^{-3}$.

In this chapter, a different motor than in Chapter 3 (approximately 80 kW to 100 kW, see Table 3.1) is used as the load impedance. For evaluating the bandwidth error, a 10.4 kW PMSM machine with variable rotational speeds and variable cable lengths is considered as load impedance. The following values are constant for the complete numerical study: the switching frequency of the inverter f_{S} is constant with 20 kHz, the dc voltage is 400 V and the PWM is realized with the trailing edge uniform sampling strategy [83]. The values for the motor winding are: $R_{\text{M}} = 180\,\text{m}\Omega$ and $L_{\text{M}} = 1.6\,\text{mH}$. An impedance analyzer measurement of the motor parasitics at 3 MHz resulted in $R_{\text{MH}} = 2\,\Omega$ and $C_{\text{MH}} = 4\,\text{nF}$. This measured values are comparable with motors of the same power rating [90], [112]. The cable parameters are calculated for a cable radius r_{i} of 1.8 mm, a shield radius r_{S} of 3.1 mm and a cable distance d of 30 mm. The cable parameters result from Equation (3.4), (3.2) and (3.3): $C_{\text{C}} = l \cdot 204\,\text{pF/m}$, $L_{\text{C}} = l \cdot 1.1\,\mu\text{H/m}$ and $R_{\text{C}} = l \cdot 1.7\,\text{m}\Omega\text{/m}$.

The frequency of the motor current f_{M} varies in the range of 0.4 Hz to 1 kHz and is limited to one digit after the decimal point in order to guarantee a periodic PWM signal (see Equation (4.10)). The computation steps of the evaluation are illustrated in Figure 4.5, where different load impedances $\underline{Z}_k$ are used in different parts of this numerical study.

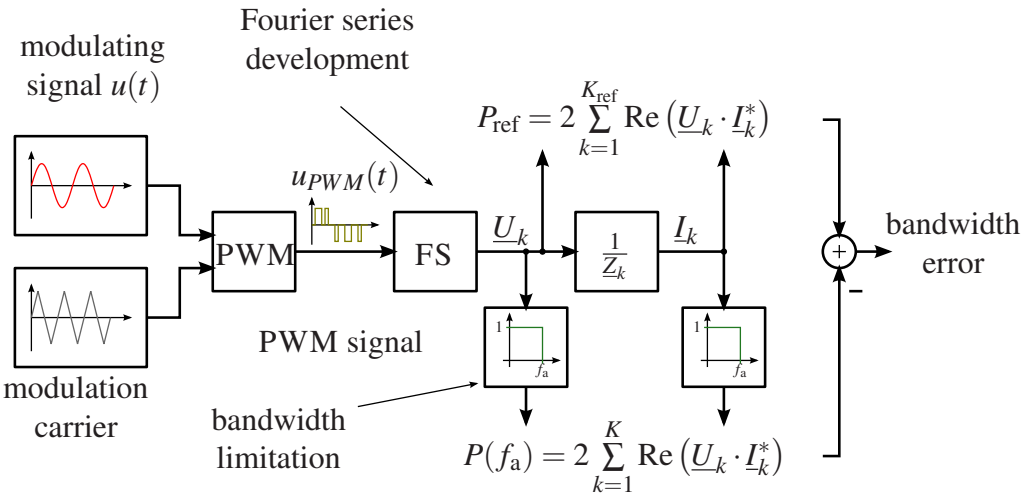

Figure 4.5.: Signal flowchart for the evaluation of the bandwidth limitation error. The current is calculated in the FS domain from the PWM voltage signal and a load impedance. Evaluating the difference between the bandlimited power and the reference power results in the bandwidth limitation error.

4.4.1. Torque-Producing Part of the Impedance

In this section the influence of a bandwidth limitation on power calculations is evaluated for the torque-producing part of the impedance $\underline{Z}^{\mathrm{M}}_{1-23}$.

For the evaluation the FS coefficients are generated up to 10 MHz for a variety of PWM voltage signals, where the reference power P_{ref} is calculated with a bandwidth of 10 MHz. The variation includes different fundamental motor current frequencies f_{M}, initial phase shifts and different amplitudes of the sinusoidal modulating signal $u(t)$ (see Figure 4.5).

The simulations showed that neither an amplitude change nor an initial phase shift between triangular carrier and sinusoidal modulating signal influences the relative error. Therefore Figure 4.6 shows the relative error for different fundamental frequencies of the motor current only. As can be seen, a higher frequency f_{M} yields a higher relative error $e_{\mathrm{rel}}(f_{\mathrm{a}})$. From the point of keeping the target uncertainty of $1 \cdot 10^{-3}$, this part of the impedance is uncritical: the relative error is for all frequencies f_{M} smaller than $1 \cdot 10^{-3}$. It is important to highlight the analog bandwidth f_{a} where the error is influenced the most: it is the inverter switching frequency f_{Sw} at 20 kHz. As soon as the bandwidth f_{a} is higher than the switching frequency f_{Sw}, the error $e_{\mathrm{rel}}(f_{\mathrm{a}})$ starts to decrease. Therefore, it is advisable to set the analog bandwidth f_{a} beyond this frequency.

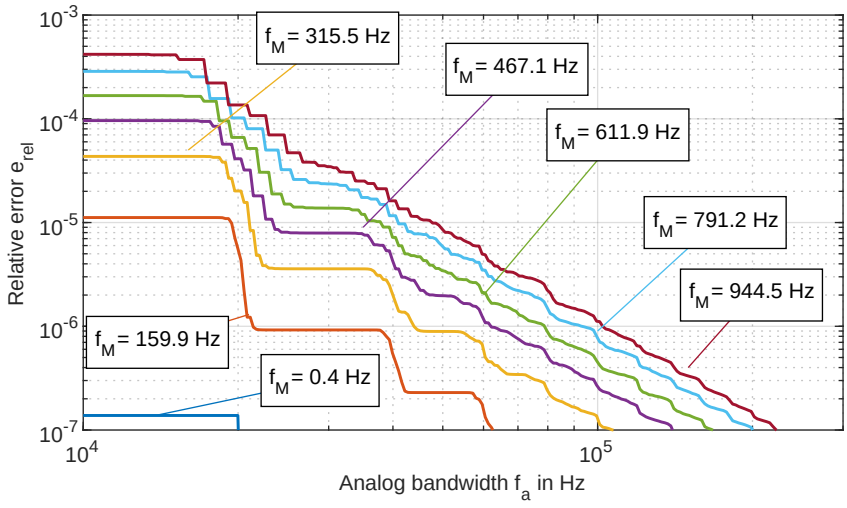

Figure 4.6.: Relative error $e_{\mathrm{rel}}(f_{\mathrm{a}})$ in power calculations as a function of the analog bandwidth f_{a} for the motor impedance $\underline{Z}^{\mathrm{M}}_{1-23}$ only. The seven lines represent different fundamental frequencies of the motor current f_{M}.

Setting the analog bandwidth to some hundreds kHz makes the bandwidth limitation error negligible.

4.4.2. Parasitic Part of the Impedance

The power dissipation $E_{\mathrm{abs}}(f_{\mathrm{a}})$ in the parasitics is expressed as an absolute value with Equation (4.5). The resonant frequency for a given motor is a function of the cable inductance L_{C} and thus a function of the cable length l. Motivated by this dependence, the bandwidth limitation error is evaluated for different cable lengths, where the reference power P_{ref} is calculated at a reference frequency of 50 MHz. In order to obtain reliable simulation results it is advisable to set the reference frequency beyond the highest frequency where a contribution is expected. In contrast to measurements, simulations allow for reliably estimating the maximum contribution. For the simulated drive parameters the resonant frequency ranges up to approximately 5 MHz. Therefore the reference frequency is set to $f_{\mathrm{a,ref}}$=50 MHz, such that the reference power is computed with a factor of ten to the highest expected contribution.

The resulting absolute error E_{abs} is shown in Figure 4.7 for four different cable lengths. As can be seen, a shorter cable with a higher resonant frequency requires a higher

analog bandwidth f_a for the same accuracy of the measurement. The maximum power dissipation is for one motor mainly a function of the capacitor C_{MH} and the dc voltage level. As the absolute error is in the range of approximately 9 W its consideration can be negligible if the power of the torque-producing part is much larger. However, accurate measurements require the consideration of these power losses, as this losses exist beside other uncertainties like sensor accuracy or ADC non-idealities. Furthermore, neglecting this losses will influence the measurement result in a biased way, i.e. the influence on the measurement result will not cancel out in the mean like in case of white noise.

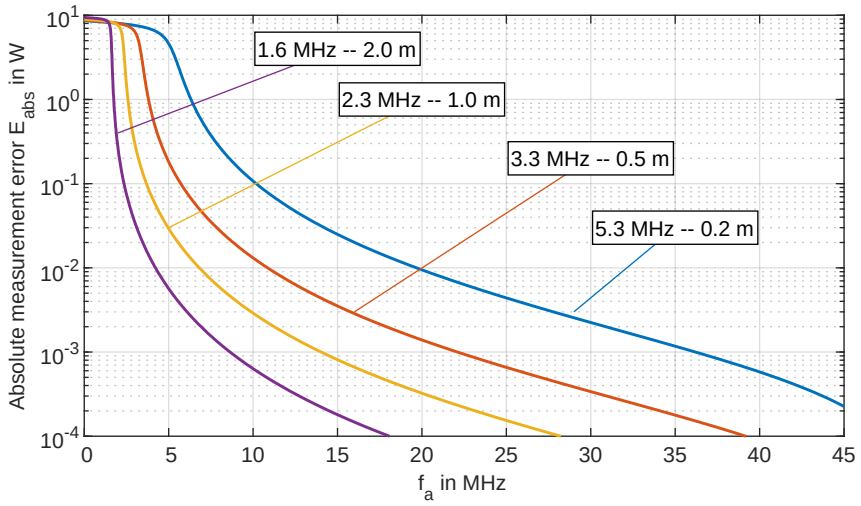

Figure 4.7.: Absolute error $E_{abs}(f_a)$ in power calculation caused by the parasitic elements $\underline{Z}^{P}_{1-23}$ of the drive impedance as a function of the analog bandwidth f_a. The different lines represent different cable lengths with different resulting resonance frequencies.

4.4.3. Total Impedance

Having discussed the torque-producing and parasitic parts of the impedance separately, the final section of this numerical study addresses the bandwidth limitation of the total impedance of the drive. As described in Section 4.3, the total error is a function of the operating point. However, the load model does not support any mechanical coupling, and therefore the different operating points are implemented by different frequencies and amplitudes of the modulation signal. Amplitude and frequency are adjusted such that the power of the torque-producing part of the load impedance results in the following

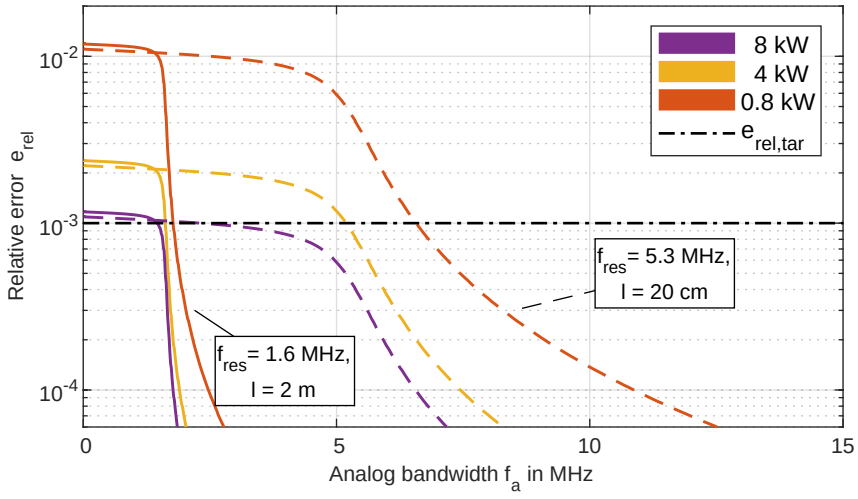

Figure 4.8.: Relative error $e_{\mathrm{rel}}(f_{\mathrm{a}})$ for the impedance of the complete electric drive $\underline{Z}_{1-23}$. The different colors represent different set points of the motor. The solid lines correspond to a cable length with 2 m and the dashed lines represent the 20 cm case. The target uncertainty $e_{\mathrm{rel,tar}}$ is visualized by the dash-dotted line.

operating points: full power with 8 kW, half power with 4 kW and low power with 0.8 kW. Evaluating these operating points with two different cable lengths illustrates the difference between running the drivetrain on a test bed or in the vehicle. The cable length l is assumed to be 2 m in case of an installation on test bed and 20 cm in case of a vehicle installation.

As shown in Figure 4.8, the relative error converges for lower frequencies to approximately $1 \cdot 10^{-3}$, $2 \cdot 10^{-3}$ and $1 \cdot 10^{-2}$ for the cases 8 kW, 4 kW and 0.8 kW respectively. From this relative errors follows, that the error at lower frequencies is limited by the ratio of the power dissipation in the parasitics to the motor operating point, where the parasitic power dissipation is approximately 9 W as evaluated in Section 4.4.2.

This indicates that the relative accuracy of a measurement is limited if a motor is operating at a low power operating point and the analog bandwidth does not cover the power dissipation of the parasitic parts. However, once the analog bandwidth covers the resonant frequency, the relative error starts to decrease. Summing up, these results show that the cable length influences the bandwidth error for a given analog bandwidth. Thus, an efficiency determined on a test bed can differ from the actual efficiency in the vehicle.

A comparison of the relative error from Figure 4.8 with the defined target uncertainty $e_{\text{rel,tar}}=1\cdot10^{-3}$ shows that the full power operating point with 8 kW is the least critical operating point. At the full power operating point, the ratio of the parasitic power to the total power violates the desired target uncertainty just slightly . Therefore, a low analog bandwidth is sufficient. The half and low power operating point with 4 kW and 0.8 kW require in case of a 2 m cable an analog bandwidth in the range of 2 MHz to meet the target uncertainty constraint. In case of the shorter 20 cm cable, the required bandwidth to fulfill the target uncertainty increases to 5 MHz and 7 MHz for the half and low power operating point respectively. Since the simulations consider an ideal low pass filter, a measurement system would require a higher bandwidth of for example 10 MHz. In practice, however, a bandwidth around some 10 MHz is not always feasible in combination with a correspondingly low level of uncertainty of the measurement chain. Therefore, power measurements with a bandwidth not covering the resonant frequency should be made, if possible, at a high power operating point, such that influence of the parasitic power is small enough.

A metrological verification of the presented results is a challenging task: a direct power measurement based on voltage and current acquisition would have to provide uncertainties low enough such that the isolated bandwidth limitation error can be determined. The difficulty gets obvious by desiring an exemplary power measurement uncertainty of one third of $e_{\text{rel,tr}}$ which is approximately $300\cdot10^{-6}$. This exemplary uncertainty must hold within the constraints of an automotive drive: amplitudes up to 1 kV and some 50 A and frequencies from dc up to at least 10 MHz. As the uncertainties of current and voltage sensor influence the resulting power uncertainty they should be at least in the range of the desired power measurement uncertainty of $300\cdot10^{-6}$. Metrological laboratories provide voltage dividers and coaxial current shunts with uncertainties in the range of $10\cdot10^{-6}$. However these sensors are typically characterized within the audio frequency band [59], [131]. Therefore, verifying the bandwidth limitation error with these sensor is limited to some hundred kHz. Another possibility for obtaining a wideband reference result for the ac power P_{ac} is to measure the dc input power P_{dc} and subtract the heat losses P_L of the inverter. If the heat losses P_L of the inverter are determined by calorimetry, they are independent of a bandwidth limitation. Calorimeter can determine the heat losses with uncertainties in the range of 1 % [108]. The output ac power P_{ac} of an inverter is then the input power P_{dc} of the inverter reduced by the heat losses P_L of the inverter and the absolute measurement uncertainty of the

output power P_{ac} is the sum of input power uncertainty plus the heat loss uncertainty. If an inverter operates at an approximate efficiency of 95 %, then the overall relative uncertainty of the ac output power is the dc input power uncertainty weighted by approximately 95 % plus the heat loss uncertainty weighted by approximately 5 %. However, reaching the desired relative overall uncertainty of some $300 \cdot 10^{-6}$ is challenging. The combined calorimetric method is presented for less stringent uncertainty requirements in the following Chapter 5 including a detailed discussion of the achievable accuracy.

4.5. Summary

This chapter presents a method for the evaluation of the bandwidth limitation in electric power measurements and analyses in detail the power measurements taken on the ac side of an inverter in an electric automotive drivetrain. The FS development and the usage of a realistic equivalent impedance of the electric drive represent the key elements of the investigation. The examination of the proposed method in a numerical study identified the resonance frequency of the parasitic components to be a critical quantity, where the simulated bandwidth limitation corresponds to filtering with an ideal rectangular lowpass filter. As illustrated in the numerical study, power measurements of the torque-producing part are sufficiently accurate with a bandwidth covering the switching frequency of the inverter.

Accurate measurements of the total power, however, require an analog bandwidth covering the parasitic power dissipation. Therefore the spectral content of the signals on the ac side has to be inspected prior to measurements with a power analyzer with attention to resonance effects with a fast acquisition device like an oscilloscope. From the point of view of practical application, the required analog bandwidth of the power analyzer can be difficult to achieve as it can exceed the range of some 10 MHz. To overcome this bandwidth limitation, the following chapter proposes a calorimetric measurement method that is inherently free of a bandwidth limitation.

Therefore, it is important to bear in mind, that power measurements can be corrupted by a significant bandwidth limitation error if the bandwidth is in the range of some hundreds kHz and therefore not covering the power dissipation of the parasitics. In conclusion, it is advisable to measure the power, if possible, at an operating point, such

that the ratio of the parasitic power dissipation to the total power is small enough for keeping the desired uncertainty.

5

Reference Power Measurement

In this chapter, a method for obtaining a reference power measurement is presented. The reference power result is utilized for evaluating the simulation-based results of the thesis and it can serve as reference by comparing power analyzers under non-sinusoidal conditions appearing in electric drives. The method provides power measurements on the ac side of the inverter by combining the dc input power with a calorimetric heat loss measurement of the inverter. The following sections discuss the constructed calorimeter, the designed electric drive and the measurement setup.

5.1. Problem Description

For measuring power in inverter-fed drives, power analyzer are typically utilized. A power analyzer samples and multiplies voltage and current at once and averages the instantaneous power for computing the active power based on Equation (2.5). Besides measurement issues like the accuracy of a probe, this sample based approach yields to the measurement issue of acquiring wide bandwidth signals.

Figure 5.1 shows measurements of voltage and current. The voltage is almost rectangular while the current is a set of piecewise linear functions, approximating a sine. The sharp switching transients and the ringing in voltage and current disclose a wide bandwidth of the circuit. To obtain accurate results of the active power, the acquisition of this signals requires fast and simultaneously accurate measurement hardware. The problem is, that the acquisition device should provide sufficient memory depth for storing multiple periods of the fundamental, a high sampling rate for capturing the high frequency resonance effects and a high amplitude resolution for handling the accuracy demands. Current signal chain electronics however are not able to handle this requirements simultaneously. Therefore, this chapter presents a novel method for measuring the power at the ac side of the inverter without the need for acquiring fast ac signals.

For verifying, evaluating or comparing the power analyzer's measurement result, a reference measurement is required. The reference measurement has to provide a smaller uncertainty to serve as a reference.

From a theoretic viewpoint, the reference power measurement has to include the full spectrum of voltage and current. In practice, the measurement system has to acquire all spectral content with a significant contribution to the power. As discussed in Chapter 4, the spectrum has to cover possible resonances resulting in a measurement bandwidth of tens of MHz. From engineering point of view, it is challenging to design a measurement chain from dc to some tens of MHz with low level of uncertainty. At the sensor side of the measurement chain, the voltage and current probes have to provide sufficient bandwidth and in addition sufficient flatness in the frequency response. In automotive drives, the voltage signal has an amplitude of typically some 100 V up to 1000 V and the current's amplitude ranges from 50 A to 200 A.

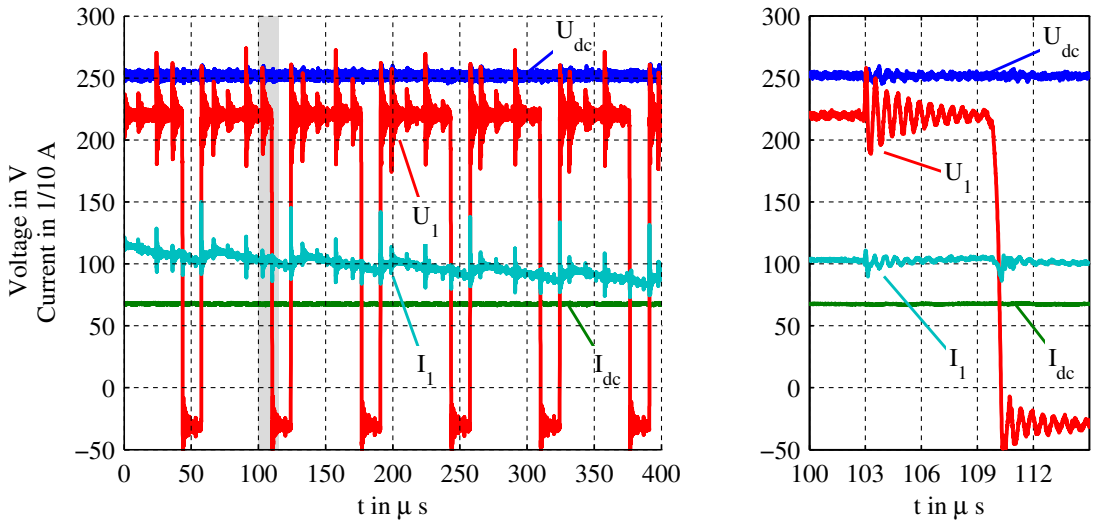

(a) Switching pattern.

(b) Zoom.

Figure 5.1.: Measured voltage and current signals on the ac and dc side of the inverter with a sampling frequency of 125 MHz. The ac voltage and current contain overshoots resulting from the switching operation of the inverter. All measurement probes are equipped with common mode chokes, reducing noise created by inverter switching. The offset of the ac voltage U_1 of −30 V is explained in Figure 5.2 and Figure 3.5.

Although it is challenging, the acquisition of the voltage signal is feasible from a practical viewpoint. Differential voltage probes are available with a flat frequency response, wide bandwidth and sufficient accuracy. Scientific research articles [60], [132] describe probe development with suitable measurement parameters.

However, the high accuracy of direct power measurements is limited by the current sensing capabilities. The article [22] reviews different techniques for current sensing. According to the article, an appropriate technology for the required frequency and amplitude range is based on coaxial current shunt resistors. Other technologies like open loop hall effect current probes suffer from accuracy while closed loop probes do not provide sufficient bandwidth. Although, a current shunt is well suited in terms of bandwidth and accuracy, the measurement of the shunt's voltage drop involves measurement issues within the setup of an automotive drive. For the phase current measurement between motor and inverter, the shunt is typically designed such that its voltage drop at full scale is in the range of 1 mV to 100 mV for keeping the shunt's power loss low. For the measurement of the shunt voltage drop a differential measurement is required, as the

inverter switches the phases from positive to negative supply and both connections of the shunt can be on the low and high side. The common mode rejection ratio (CMRR) of the differential stage becomes therefore an important parameter. Although, single operational amplifier provide CMRRs up to 130 dB, full differential voltage probes offer CMRRs in the range of some 70 dB (see [60, see Table I]). For current shunt measurements with the common mode voltage up to 1000 V and voltage drops in the mV range, a CMRR of at least 100 dB would be required to obtain a common mode influence smaller than 0.1 %. Up to now, such CMRR's are not commercially available within MHz bandwidth, kV common mode voltage and mV voltage drop.

As the direct sampling measurement of the power is not suitable for reference measurements a further approach is presented. Besides the digital sampling approach, a calorimetric approach for power measurements of electric drives is proposed [104], [105]. The calorimetric method measures directly heat losses independently of their origin like mechanic friction losses or electric power losses. However, calorimeters are either bulky or suffer from accuracy if large output power from an inverter is measured directly. Therefore, a combined method for determining the ac power is proposed in this chapter.

This chapter proposes a novel method for providing a reference power result for the ac power to overcome the drawback of the power analyzer's limited bandwidth as well as the limited power measurement range of the calorimetric approach. The reference result for the ac power is determined by combining a dc power measurement with a calorimetric heat loss measurement. As the proposed method does not require to measure ac quantities, the reference result provides the important feature, that it is not affected by a bandwidth limitation. This desirable property is achieved as the proposed method provides inherently dc quantities. However, the calorimetric approach needs a stationary operating point of the motor.

5.2. Measurement Principle

For understanding the measurement principle, the topology of an electric drive is depicted in Figure 5.2 with focus on power flows. The aim is to measure the power

on the ac side, denoted as P_{ac}. Instead of measuring the ac side power P_{ac} directly by voltage and current measurements it is determined by the relation

$$P_{dc} - P_{ac} - P_L = 0. \tag{5.1}$$

Equation (5.1) states that all powers entering and leaving the inverter sums up to zero, which is true if the system is in thermal equilibrium. By rearranging Equation (5.1), it is possible to compute the ac output power P_{ac} by means of the dc input power P_{dc} and the inverter losses P_L:

$$P_{ac} = P_{dc} - P_L. \tag{5.2}$$

For implementing Equation (5.2), the dc input power P_{dc} and the loss power P_L have to be measured.

The dc input power P_{dc} is measured straightforward: measurements of voltage and current are multiplied and result in the active power P_{dc} supplied by the source. As depicted in Figure 5.2, an optional LC filter stage supports the dc link capacitor in decoupling the switching actions of the inverter from the ac side to the dc side. This filter minimizes ac content in the signals on the dc side and allows for computing the dc power with a simple product

$$P_{dc} = U_{dc} \cdot I_{dc}. \tag{5.3}$$

The simple computation is only allowed, if current *and* voltage do not include ac content, which is guaranteed by the additional *LC* filter stage.

The loss power P_L of the inverter is measured directly with a calorimeter. In comparison to a direct calorimetric measurement of the ac output power P_{ac}, the calorimeter can be constructed much smaller for measurements of the loss power P_L, as the heat losses of the inverter are much smaller than the ac output power P_{ac}. The heat losses P_L lie typically in the range of 10 % of the dc input power P_{dc}.

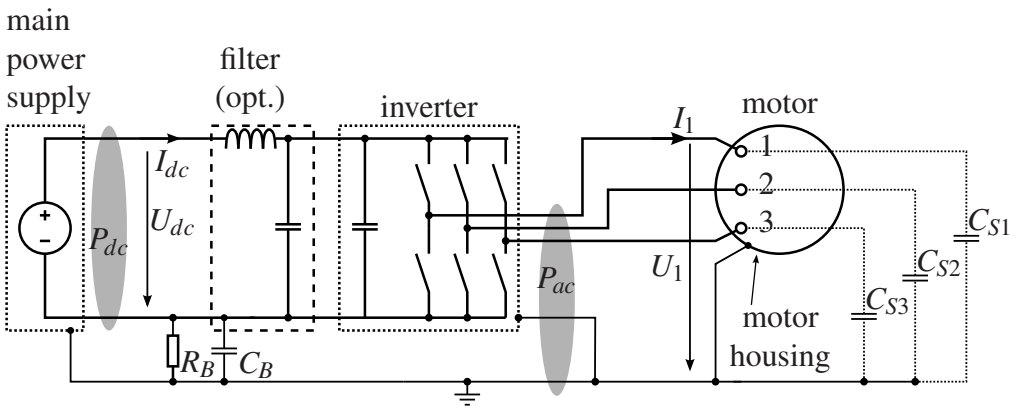

Figure 5.2.: Electric drive with a three-phase inverter and a motor in an automotive application. All housings are bonded to ground via chassis. The negative power supply output is connected to ground for safety reasons with a bonding resistor $R_B = 370\,\mathrm{k\Omega}$ and a bonding capacitor $C_B = 3\,\mu\mathrm{F}$. The capacities C_{S1}, C_{S2} and C_{S3} represent the stray capacitance of cabling, inverter and motor winding for each motor phase. The LC filter stage minimizes ac content of the current I_{dc} and the voltage U_{dc}.

5.3. Calorimetric Power Measurement

The working principle is based on the fact that the rise of temperature in an arbitrary ac or dc load relies exclusively on active power. Through this principle, the calorimeter gives a measurement result exclusively as a function of the active power, and independent of the spectral composition of voltage and current signals. Further details on the different variants of calorimeters, their properties and a classification is given in the review article [105].

Based on the classification in [105], a closed and balanced type calorimeter is utilized to determine the electric power on the ac side of the inverter. For this type of calorimeter, the temperature difference δ between the inside temperature T_i and the outside temperature T_o is utilized for computing the loss power P_L inside the calorimeter. To obtain low levels of uncertainty of the measured loss power P_L, it is important that the temperature difference δ is constant after an initial transient. The constant value of the temperature difference δ requires that the transfer function from the loss power P_L to the inside temperature t_i has lowpass character with a longer time constant τ_{th} than the common signal period T_{Sig} (corresponds to the slowest thermal dynamics of the device under test). The time constant τ_{th} is a function of the thermal transfer resistance R_{th} and the

thermal mass C_{th} of the calorimeter. The realized calorimeter is illustrated in Figure 5.3 and consists of a wooden box serving as thermal insulator, two temperature sensors for determining the temperature difference between in- and outside the wooden box, an electric heating unit and a fan inside the box securing a homogeneous temperature distribution. The picked temperature sensors provide an absolute accuracy of $\pm 0.5\,^{\circ}\text{C}$. For balanced type calorimeters, a small hysteresis error is more important than a high accuracy. For the picked temperature sensor the hysteresis error is $\pm 2 \cdot 10^{-3}$ K.

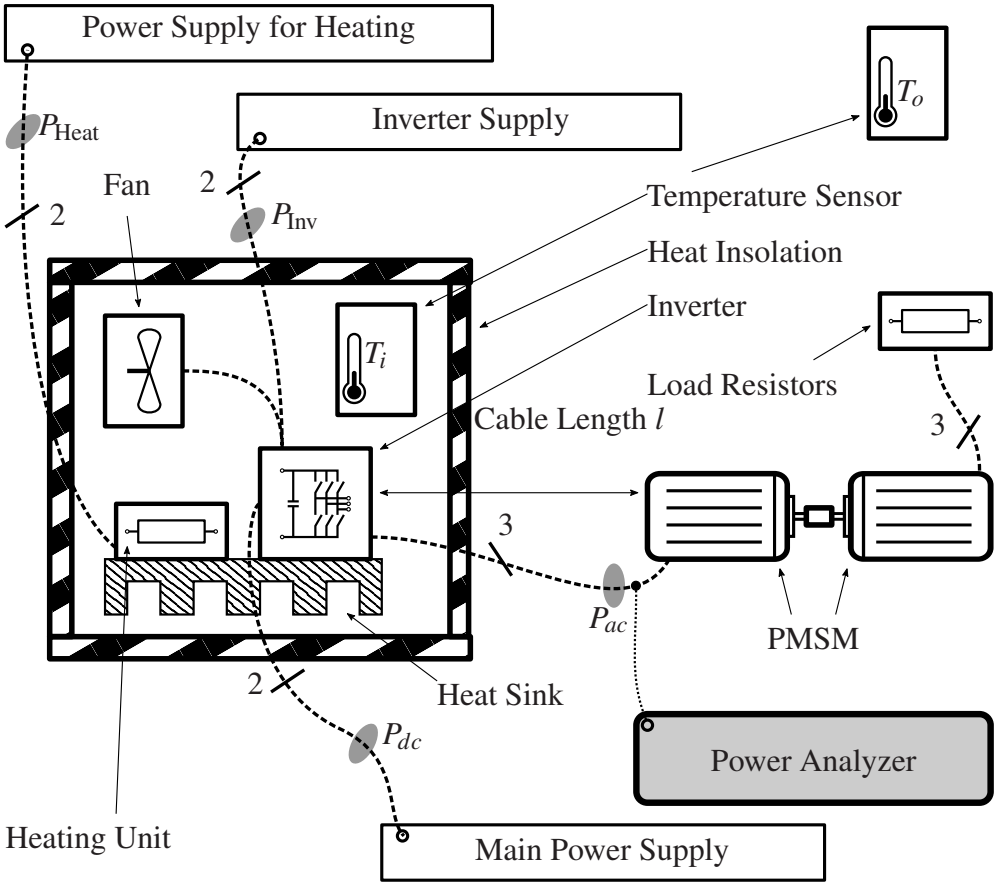

Figure 5.3.: Components for calorimetric ac power measurements. The complete setup is placed in a climate camber for having constant ambient temperature T_o. In the first stage, the inverter drives the motor and rises the interior temperature T_i of the box. In the second stage, the inverter is in standby and the heating unit is controlled such that the same temperature rise prevails.

5.3.1. Calorimeter Design

Power measurements with closed and balanced type calorimeter transfer power measurements to temperature difference measurements. The principle of operation is, that in a first step the inverter is placed in the calorimeter and drives the motor in a stationary operating mode. Because of the heat losses of the inverter P_L, the temperature inside the calorimeter T_i raises. The temperature rise relies exclusively on the active power in the calorimeter. For determining the loss power, this temperature rise is compared to the temperature rise resulting from a dc power source. If the rate of temperature change is equal for the ac and dc case, both power losses have to be identical and independent of the spectral composition of voltage and current signals as long as their common signal period is much shorter than the time constant τ_{th} of the calorimeter.

For designing a calorimeter, relevant parameters are

1. the heat loss inside the calorimeter P_L,
2. the maximum allowed temperature inside the calorimeter T_i,
3. the thermal mass C_{th} of the calorimeter.

The first two parameters determine the thermal resistance of the calorimeter R_{th} ($[R_{\text{th}}] = \text{K}/\text{W}$) with the following relation:

$$R_{\text{th}} = \frac{T_i - T_o}{P_L} = \frac{\delta}{P_L}, \tag{5.4}$$

where T_o denotes the temperature outside the calorimeter and δ the temperature difference between in- and outside. The aim is to provide a reference result for the active power on the ac side of the inverter P_{cac} by measuring the dc input power P_{dc} and the inverter losses. Therefore the inverter has to be placed in the calorimeter. By embedding the inverter in the calorimeter, three boundary conditions become effective for the utilized electric drive:

1. The calorimeter's interior edge length l_{cal} must be larger than 0.3 m, such that the inverter fits in the calorimeter.
2. The heat loss in the calorimeter P_L is approximately 10 % of the motor power, resulting in 200 W for a motor load of 2 kW.

3. The maximum allowed temperature inside the calorimeter T_i is limited by standard electronic components and integrated circuits to 85 °C.

The following design procedure gives a rough estimate of the calorimeter design. A more precise design would require a comprehensive simulation of all heat transfer processes including material properties and environmental conditions. Within the scope of this work, however, a rough design is sufficient, as the focus is on the measurement uncertainty. The measurement uncertainty of the calorimeter mainly depends on the temperature and power measurement accuracy and not on the calorimeter design.

The calorimeter structure is cubic for keeping the construction effort low. From the cubic design follows the thermal resistance R_{th} which is composed by the material's heat conduction and the thermal transmission [133, Ch. 2.2.]:

$$R_{\text{th}} = \underbrace{\frac{d_{\text{cal}}}{6 \cdot l_{\text{cal}}^2 \cdot \kappa}}_{\text{conduction}} + \underbrace{\frac{R_t}{6 \cdot l_{\text{cal}}^2}}_{\text{thermal transmission}} \qquad [\kappa] = \text{W}/(\text{m K}) \qquad [R_t] = \text{m}^2\,\text{K}/\text{W}, \tag{5.5}$$

with κ as the thermal conductivity of the insulation material and d_{cal} as the insulation material thickness. The thermal transmission coefficient R_t considers the thermal resistance due to convection and radiation. The actual value of the transmission coefficient R_t can be computed on basis of the geometric structure, the temperature difference δ, the thermodynamic properties of air, the roughness of the surface and the convection situation in terms of natural or forced velocity profiles [133]. As the aim is to roughly estimate the thermal resistance R_{th}, the thermal transmission coefficient R_t is approximated by consulting norms for energy efficient construction of buildings, as for example [134]. An air velocity of 1 m/s results in a thermal transmission coefficient R_t of 0.08 $\text{m}^2\,\text{K}/\text{W}$ for the transmission from outer air to the thermal insulator. The transmission from the inner air to the insulator is much smaller and it is therefore neglected, as a fan inside the calorimeter provides a much high air velocity than 1 m/s. The air velocity of 1 m/s is a rough estimation for the air speed around the calorimeter placed in a climate chamber.

The three design variables namely the insulation material with a specific thermal conductivity κ, the insulation material thickness d_{cal} and edge length l_{cal} , have to be chosen such that the inner temperature T_i does not exceed the limit of 85 °C at the maximum loss power P_L of 200 W and the edge length larger than 0.3 m. Figure 5.4(a) illustrates

the relation between loss power P_L and temperature difference δ for different thermal resistances R_{th}. If the outer temperature T_o is assumed to be 20 °C, the maximum temperature difference δ is 65 K. This temperature difference is met for all depicted values of R_{th} in Figure 5.4(a) for the considered maximum losses of 200 W. Therefore, a thermal resistance R_{th} smaller than approximately 0.3 K/W is desirable for the calorimeter design. The smaller the thermal resistance R_{th} becomes, the more loss power can be measured with the calorimeter without violating the boundary condition of a maximum interior temperature T_i of 85 °C. An upper bound for the thermal resistance is therefore 0.3 K/W and in the following design stage the realization of this thermal resistance is discussed.

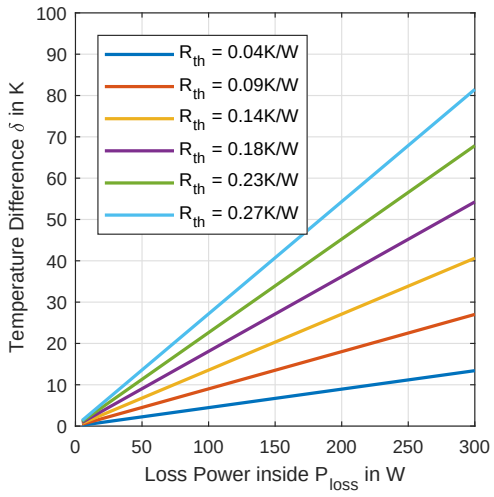

(a) Temperature difference δ as a function of the loss power P_L according to Equation (5.4) for different values of the thermal resistance R_{th}.

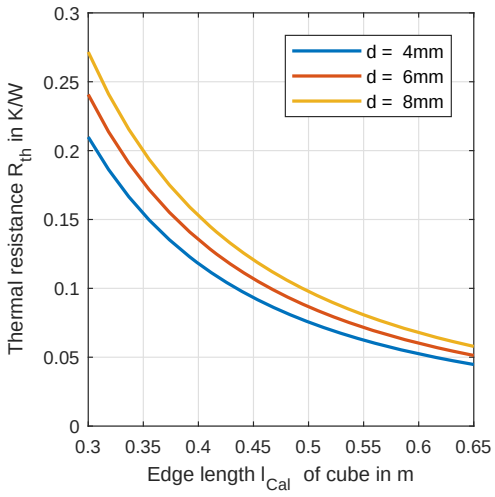

(b) Thermal resistance R_{th} given as a function of the calorimeter box's edgle length l_{cal} and the insulation material thickness d_{cal} according to Equation (5.5).

Figure 5.4.: Computed values of the calorimeter with an assumed thermal transmission value R_t of 0.08 $\text{m}^2\text{K/W}$. The insulation material is poplar plywood with a thermal conductance κ of 0.12 W/(mK).

In Figure 5.4(b), the thermal resistance R_{th} is shown as a function of the edge length of the box l_{cal} for three available insulation material thickness values d_{cal}. The insulation material is plywood with a thermal conductance κ of 0.12 W/(mK) [133, tab. A.2]. An insulation material with a lower thermal conductance κ (e.g. expanded polystyrene κ = 0.033 W/(mK)) would result in two undesirable calorimeter design constraints for a thermal resistance R_{th} smaller than 0.3 K/W. Either the calorimeter's edge length

l_{cal} would be large, making the calorimeter bulky or another design possibility would be the usage of thin walled insulation material making the calorimeter mechanically fragile. All depicted material thicknesses d_{cal} and edge lengths l_{cal} in Figure 5.4(b) are suitable for the calorimeter design, as they result in a thermal resistance R_{th} smaller than $0.3\,\text{K/W}$.

For a convenient construction, an edge lengths l_{cal} of 0.5 m and a material thicknesses d_{cal} of 8 mm is selected. This design parameters result in a calculated thermal resistance R_{th} of $0.1\,\text{K/W}$ and a temperature difference δ of approximately 20 K at 200 W loss power P_L.

The thermal time constant τ_{th} of the calorimeter describes the time to cool down the calorimeter to 37 % of its initial inner temperature T_i or to heat the calorimeter to 63 % of its final temperature [133, eq. 1.23]. The thermal time constant τ_{th} of the calorimeter can be computed from the heat capacity of the air inside the calorimeter, the thermal heat capacity of all components inside the calorimeter and the thermal resistance R_{th}.

The heat capacity of the air can be computed from the design parameters of the calorimeter. The heat capacity of all components inside the calorimeter can not be computed straight forward, as the cabling, the additional fan, the heating unit and the inverter consist of a broad material mix. Therefore the heat capacity of all components C_{th} is roughly approximated by a solid aluminum (Al) cube with the same volume V_{inv} as the inverter's IGBT modules and heat sink:

$$\tau_{\text{th}} = R_{\text{th}} \cdot \underbrace{\left(\underbrace{\rho_{\text{Air}} \cdot l_{\text{cal}}^3 \cdot c_{p\,\text{Air}}}_{\text{heat capacity of air}} + \underbrace{\rho_{\text{Al}} \cdot V_{\text{inv}} \cdot c_{p\,\text{Al}}}_{\text{heat capacity of components}} \right)}_{\text{heat capacity } C_{\text{th}}}, \tag{5.6}$$

with the material density ρ, and the specific heat capacity c_p.

For an inner air temperature T_i of 27 °C, the thermal time constant τ_{th} of the calorimeter

evaluates to

$$\tau_{\text{th}} = 0.1\,\frac{\text{K}}{\text{W}}\cdot \left(\underbrace{1.177\,\frac{\text{kg}}{\text{m}^3}\cdot 0.125\,\text{m}^3\cdot 1007\,\frac{\text{W s}}{\text{kg K}}}_{\text{air}} + \underbrace{2700\,\frac{\text{kg}}{\text{m}^3}\cdot 3\cdot 10^{-3}\,\text{m}^3\cdot 896\,\frac{\text{W s}}{\text{kg K}}}_{\text{aluminum}} \right) = 740\,\text{s} = 12.4\,\text{min}, \quad (5.7)$$

where the non-air volume of the inner components V_{inv} (i.e. mainly the inverter) is approximated by $3\,\text{dm}^3$. As will be shown later in the experimental section, the actual thermal time constant τ_{th} of the calorimeter *plus* all components is approximately three times larger. The heat capacity of the air inside the calorimeter is well known. Therefore it can be concluded, that the computation of the heat capacity of all remaining components inside the calorimeter is over simplified. The inverter consists of a broad material mix with an unknown mass distribution. Therefore, it is not possible to predict the thermal time constant τ_{th} of the calorimeter accurately by such a simple formula as Equation (5.6).

The measured thermal resistance R_{th} of the constructed calorimeter is shown in Figure 5.5 for different operating points between 60 W to 180 W loss power P_L. As can be seen, the measured thermal resistance R_{th} varies and therefore the temperature and loss power relationship is not perfectly linear. The nonlinear behavior can be explained by thermal convection and radiation. Although the behavior is not perfectly linear, a least-squares fit of the thermal resistance R_{th} with $123\cdot 10^{-3}\,\text{K/W}$ approximates the behavior over a wide operation range well. The nonlinear behavior of the calorimeter does not have an influence on the measurement result as the balanced measurement procedure corresponds to a calibration at each operating point. Further details on the measurement procedure are given in the next section.

Differences between the predicted value of R_{th}=$100\cdot 10^{-3}\,\text{K/W}$ (Equation (5.5)) and the measured value of R_{th}=$123\cdot 10^{-3}\,\text{K/W}$ can be explained by two influences: Firstly, the cubic design requires additional square timber elements beside the rectangular plywood boards for bonding and screwing the boards together. This square timber elements

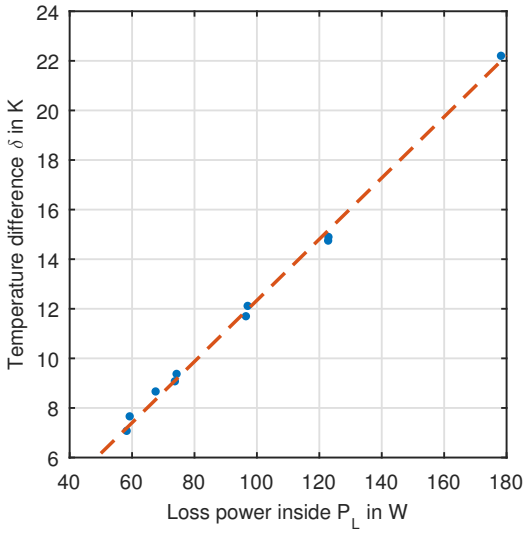

Figure 5.5.: Measured values of the calorimter with the design parameters thickness d=8 mm and an edge length l_{cal} = 0.5 m. The dots denote measured steady-state operating points. The dashed line represents the linear least squares fit of the thermal resistance R_{th} resulting in $123 \cdot 10^{-3}$ K/W.

increase the effective thickness d_{cal} of the surface volume resulting in a higher thermal resistance R_{th}. Secondly, the thermal transmission is roughly modeled with a single transmission coefficient R_t, although complex heat transfer processes like radiation and convection are covered.

5.3.2. Measurement Procedure

The calorimeter determines the power on the ac side of the inverter $P_{c\,ac}$ in two stages: in the first stage the drive is in normal operation mode and the temperature inside the box T_i rises due to heat loss. The temperature rise results from the sum of all electric power entering the insulated box, the heat capacity C_{th} of the components in the box and the heat transfer rate to the outside of the box described by the thermal resistance R_{th} ($[R_{\mathrm{th}}] = \mathrm{K/W}$). After an initial transient time t_{th}, the temperature difference δ_{I} between the inside temperature of the box T_i and outside temperature of the box T_o is steady. The transient time t_{th} depends on the time constant of the calorimeter τ_{th}. For the constructed calorimeter, the time constant τ_{th} to obtain 63 % of the final value is approximately 30 min resulting in a transient time t_{th} of 3 h. The steady state temperature

difference δ_1 results from :

$$\delta_1 = (T_i - T_o)|_{\text{motor running}} = R_{\text{th}} \cdot (P_{dc} - P_{cac} + P_{\text{inv1}}) . \tag{5.8}$$

In Equation (5.8), P_{inv1} denotes the auxiliary power of the inverter and the fan inside the box. The ac power P_{cac} is subtracted from the dc power P_{dc} as it channels through the thermally insulated box. After the initial transient temperature rise t_{th}, the drive is deactivated and the temperature difference δ_1 is saved for the next measurement stage.

The second stage of the measurement process is the heating stage, which follows immediately the first stage. In this stage, the heating unit inside the box is powered by a temperature controlled dc source such that the temperature difference δ_2 prevails the same temperature difference δ_1 as during the first running-motor stage:

$$\delta_2 = (T_i - T_o)|_{\text{heating}} = R_{\text{th}} \cdot (P_{\text{heat}} + P_{\text{inv2}}) . \tag{5.9}$$

The power P_{inv2} describes the power consumption of the fan and the inverter with disabled electronic power switches and P_{heat} denotes the power of the heating unit.

The ac power P_{cac} results from subtracting Equation (5.8) from Equation (5.9):

$$P_{cac} = P_{dc} + P_{\text{inv1}} - P_{\text{heat}} - P_{\text{inv2}} - \frac{\delta_1 - \delta_2}{R_{\text{th}}} . \tag{5.10}$$

Under ideal conditions the last term $\delta_1 - \delta_2 / R_{\text{th}}$ will cancel out; in reality, the magnitude of $\delta_1 - \delta_2 / R_{\text{th}}$ is at least very small. Hence, it is sufficient to measure dc power and temperatures for determining the active ac power on the ac side of the inverter P_{cac} as can be seen from Equation (5.10). For precise measurements, it is important that the ambient conditions and the setup of the calorimeter do not change between the two stages. Therefore, the complete setup is housed in a climate chamber with a constant temperature T_o of 18 °C and the wooden box and its cabling is not modified between the two measurement stages.

5.3.3. Uncertainty Evaluation

Calorimetry

In order to compare the calorimetric ac power measurement with the result of the power analyzer, the upper bound for the uncertainty of the calorimetric ac power ΔP_{cac} is derived by error propagation:

$$\Delta P_{cac} = \Delta P_{dc} + \underbrace{\Delta P_{\text{inv1}} + \Delta P_{\text{inv2}} + \Delta P_{\text{heat}} + \frac{\Delta\delta}{R_{\text{th}}}}_{\Delta P_{\text{cal}}} + \frac{\delta_1 - \delta_2}{R_{\text{th}}^2}\Delta R_{\text{th}}. \tag{5.11}$$

The terms ΔP_{dc} and ΔP_{heat} denote the worst case measurement uncertainty of the dc power P_{dc} and the heating power P_{heat}. The measurement uncertainty of the inverter supply P_{inv} is denoted by ΔP_{inv1} for the first measurement stage and ΔP_{inv2} for the second measurement stage. Nonideal steady state temperature conditions and measurement uncertainties of the temperature sensor are expressed by $\Delta\delta$. The term ΔR_{th} denotes a possible change of the thermal resistance R_{th} of the calorimeter. In Equation (5.11), the uncertainty can be split into two parts.

The first part is the uncertainty of the dc power measurement ΔP_{dc}. The measurement of the inverter's dc input power P_{dc} is realized by means of measuring the dc voltage U_{dc} and the voltage drop U_{s} across a high precision current shunt R_{s}. Hence, the dc input power P_{dc} evaluates to

$$P_{dc} = U_{dc} \cdot \underbrace{\frac{U_{\text{s}}}{R_{\text{s}}}}_{I_{dc}}. \tag{5.12}$$

The measurement of P_{dc} is realized by two *Keithley 2100* 6.5 *digit* voltmeters. As the voltmeters are specified for dc signals, no ac ripple is allowed. Therefore, the additional *LC* filter stage supports the dc link capacitor of the utilized inverter. This filter stage minimizes ac content of the voltage and current signals. The measurement uncertainty of the dc power measurement ΔP_{dc} incorporates:

1. the uncertainty of the voltage measurement ΔU_{dc},
2. the current shunt's uncertainty ΔR_{s},

3. and the uncertainty of the current shunts voltage drop measurement ΔU_s.

The dc power measurements uncertainty can in general be computed by two methods: by the GUM [75] or by error propagation. In terms of computational complexity both methods are approximately equivalent. The main difference is, that within the GUM framework a uncertainty coverage factor smaller than 100 % is considered, whereas error propagation is based on an uncertainty coverage factor of 100 % and thus corresponds to the worst case uncertainty [135]. Error propagation therefore leads to more conservative estimates of the measurement uncertainty. But the main advantage of error propagation is that no detailed knowledge about the uncertainty distributions of the physical measurement process has to be known. Most measurement devices state their uncertainty in terms of a guaranteed maximum deviation which is equivalent to a 100 % coverage factor. Therefore, a comparison with such a measurement device has to be performed on basis of the worst case measurement uncertainty. Considering the three uncertainties ΔU_{dc}, ΔR_s and ΔU_s, the dc power measurement's worst case uncertainty ΔP_{dc} calculates to

$$\Delta P_{dc} = \left|\frac{\partial P_{dc}}{\partial U_{dc}} \cdot \Delta U_{dc}\right| + \left|\frac{\partial P_{dc}}{\partial U_s} \cdot \Delta U_s\right| + \left|\frac{\partial P_{dc}}{\partial R_s} \cdot \Delta R_s\right| \tag{5.13}$$

$$\Delta P_{dc} = P_{dc} \cdot \left(\left|\frac{\Delta U_{dc}}{U_{dc}}\right| + \left|\frac{\Delta U_\mathrm{s}}{U_\mathrm{s}}\right| + \left|-\frac{\Delta R_\mathrm{s}}{R_\mathrm{s}}\right|\right). \tag{5.14}$$

The second part in Equation (5.11), ΔP_cal results from the calorimetric measurement. The uncertainty of the inverter supply power during the two measurement phases ΔP_inv1 and ΔP_inv2 and the uncertainty of the heating power ΔP_heat results from the measurement hardware on an individual microcontroller board and two further *Keithley 2100* 6.5 *digit* multimeters. The microcontroller board measures the inverter supply voltage U_inv and the heating current I_heat with two 24 bit sigma-delta ADCs at a sampling rate of 640 Hz. The data sampling rate of 640 Hz is averaged to the time basis of the temperature controller of 1 s. The worst case uncertainty of the measurement chain of the inverter supply voltage U_inv and the heating current I_heat is approximately $\frac{\Delta U_\mathrm{inv}}{U_\mathrm{inv}} = 183 \cdot 10^{-6}$ and $\frac{\Delta I_\mathrm{heat}}{I_\mathrm{heat}} = 14 \cdot 10^{-3}$ for the relevant measuring range. The temperature difference is measured with two digital temperature sensors providing a hysteresis error of 2 mK. For an improved overall uncertainty, the inverter supply current I_inv and the heating voltage U_heat are measured with the *Keithley 2100* multimeters providing a range dependent uncertainty. For the relevant range, the worst case uncertainty is approxi-

mately $\frac{\Delta I_{\text{inv}}}{I_{\text{inv}}}=1.8\cdot 10^{-3}$ for the inverter supply current I_{inv} and $\frac{\Delta U_{\text{heat}}}{U_{\text{heat}}}=60\cdot 10^{-6}$ for the heating voltage U_{heat}. The uncertainty of the resulting power of these terms computes to

$$P_x = U_x \cdot I_x \tag{5.15}$$

$$\Delta P_x = \left|\frac{\partial P_x}{\partial U_x}\cdot \Delta U_x\right| + \left|\frac{\partial P_x}{\partial I_x}\cdot \Delta I_x\right| \tag{5.16}$$

$$\Delta P_x = P_x \cdot \left(\frac{\Delta U_x}{U_x} + \frac{\Delta I_{\text{x}}}{I_{\text{x}}}\right), \tag{5.17}$$

where the subindex x stands for inv1 (inverter supply during normal motor operation), inv2 (inverter supply during deactivated drive) and heat (heating unit).

By evaluating Equation (5.11), uncertainties of the thermal resistance R_{th} are not considered, as the influence of ΔR_{th} on $P_{c\,ac}$ is almost negligible. Additionally, the thermal resistance R_{th} is constant during one measurement because of the balanced calorimetric measurement principle.

Power Analyzer

In the experimental section the calorimetric ac power $P_{c\,ac}$ measurement is compared with the result of an commercial power analyzer P_{ac}. The uncertainty bounds of the power analyzer's result ΔP_{ac} are usually a function of the effective voltage and current, the frequency range of the signals and the power factor. Because of the non-sinusoidal waveforms a further issue arises on the ac side: neither the ac current nor the ac voltage are pure sine waves in an inverter application. Both signals result from the switching operation and are composed by multiple spectral components.

For computing the uncertainty of the power analyzer it is *not* defined which frequency (e.g. switching frequency, fundamental frequency or bandwidth) has to be considered for inserting into the power analyzer's uncertainty equations from the users's manual (see Equation (5.18)). An obvious possibility for defining a frequency is to consider the signal component with the highest spectral contribution. Therefore the fundamental frequency is utilized for the current's and the active power's uncertainty and the inverter's switching frequency determines the voltage uncertainty.

5.4. Experiments

In this chapter, the measurement results of the ac power of the calorimetric method P_{cac} are compared with the power analyzers results P_{ac}.

5.4.1. Constructed Electric Drive

In this section, the investigated electric drive is described and details concerning the construction are presented.

The components of the electric drive are: a dc power source, a three-phase inverter driving a permanent magnet synchronous motor (PMSM) connected via a jaw-type coupling with a second PMSM acting as generator. The generator is connected to load resistors converting the generator's torque into heat energy. These components are wired according to Figure 5.3 and Figure 5.2.

The negative power supply output is connected to ground via a resistor R_B and a capacitor C_B as shown in Figure 5.2. By doing so, the grounding scheme of the drive in Figure 5.2 complies with automotive safety guidelines.

The main power supply is realized by a dc power source providing an isolated dc output voltage U_{dc} directly wired to the LC filter at the inverter. The supply operates in regulated voltage source mode. An individual microcontroller board based on an *ARM Cortex-M4* chip provides the control signals for the inverter. The microcontroller implements a field oriented control (FOC) algorithm for the PMSM with current and speed control. The design details of the FOC are as follows:

Control operation region The FOC control algorithm is configured to work without flux weakening and with a constant angle of 90° between the current and flux space vector. Therefore the machine's current in the flux direction is controlled to zero.

Current measurement The current is determined by measuring the phase current with closed loop Hall effect sensors. The sensors provide a galvanic insulation from the measured circuit current. The current output is captured by the microcontroller's ADC via a precision Surface Mounted Devic (SMD) shunt.

Digital controller The digital control is realized by a proportional-integral controller with an anti-windup structure. The controller parameters are designed by the design rules of symmetrical[1] and amplitude optimum.[2]

Rotor position measurement Within FOC, the current space vector has to be aligned with respect to the flux space vector, as the torque is the vector product of current space vector and flux space vector . The flux space vector is directly aligned with the rotor position because of the rotor's permanent magnets. Although methods exist to estimate the alignment without a position sensor, the more precise and more robust method is to measure the rotor position with a sensor. The rotor position is determined with an incremental encoder with 4096 square-wave impulses per turn. The incremental encoder provides two output channels with a 90° square-wave signal offset for direction detection and a separate zero channel for determining the absolute position. As the microcontroller provides an encoder interface mode for a counter unit, the position determination is fully automatic without interrupt and event handlers.

Space-vector generation The voltage space vector provided by the control algorithm in direct and quadrature machine coordinates are realized by the classical space-vector PWM (SVPWM) scheme [19] with a symmetrical switching pattern for the first and second half of the switching period (f_{Sw}=15 kHz).

Speed measurement The speed is determined by digital differentiation of the position measurement. The differentiation is evaluated on a constant time basis of 1 ms.

Software organization The timing of the control algorithm has to be synchronous with the switching cycle of the space-vector generation. Therefore, the switching pattern generating timer unit triggers the ADC's to convert the motor currents and the dc bus voltage. After the conversion is finished, an interrupt is triggered for running the FOC algorithm. The FOC algorithm computes new values for the subsequent switching sequence with all current regulators and coordinate transformations. The communication with the host computer is realized via a command line interface. For this communication task, a real-time operating system

[1] In German: *Symmetrisches Optimum*
[2] In German: *Betragsoptimum*

provides the underlying communication firmware. The soft- and firmware was partly developed within the master's thesis published in [136].

5.4.2. Investigated Experiments

The experiments include a parameter variation of the brake motor's load and the activation of the power analyzer's anti-aliasing filter (AAF). For all experiments the main power supply dc voltage U_{dc} is constant at 250 V and the motor speed control is set to a mechanical speed of 1050 rpm, resulting in a fundamental frequency of the motor current of 70 Hz (4 pole pairs). The assembly of the test stand results in a cable length of 1.25 m between inverter and motor and the inverter uses a switching frequency of 15 kHz.

5.4.3. Utilized Power Analyzer

The power analyzer utilized is a *Fluke Norma 5000* [31]. It is equipped with power phase channels type PP50 providing a sampling frequency of 1.024 MHz with a bandwidth of 10 MHz. Additionally the power analyzer has activatable AAFs with a cutoff frequency of 100 kHz. The anti-aliasing filter (AAF) allows for artificially reducing the analyzer's bandwidth, such that the sampling theorem is fulfilled and harmonic analysis can be carried out. The last calibration of the power analyzer was performed in 2012. Because of the out-of-date calibration, all following results should be taken on a relative scale, such that the results are comparable among each other rather than absolutely.

According to the power analyzer's reference manual [31, sec. 11], the ac uncertainty for voltage and current signals is specified as a function of the signal RMS range (rng), the RMS reading (rdg) and the signal frequency. Within this thesis, the frequency of the spectral component with the largest amplitude is used as signal frequency for determining the uncertainty. According to the user's manual, the relative current uncertainty F_i in the frequency range from 10 Hz to 1000 Hz has an uncertainty of $\pm(0.05\,\% + 0.05\,\%\ \mathrm{rng_i}/\mathrm{rdg_i})$. In contrast to the current signal, most signal power of the voltage signal is located at the spectral component of the inverter's switching frequency. Therefore the relative voltage measurement uncertainty F_v is determined for a frequency of 15 kHz and it is $\pm(0.235\,\% + 0.235\,\%\ \mathrm{rng_u}/\mathrm{rdg_u})$.

The uncertainty per motor phase ΔP_n is computed according to the formula given in the power analyzer's reference manual [31, p. 11–5]. The reference manual's formula sums the relative voltage and current uncertainty and a further expression incorporating the phase uncertainty k_a, the range to reading ratio $\frac{\text{rng}}{\text{rdg}}$ and the power factor λ:

$$\Delta P_n = P_n \cdot \left(F_v + F_i + \underbrace{\frac{\pi \cdot k_a}{180} \cdot \sqrt{\max\left(1; \frac{\text{rng}_v}{\text{rdg}_v}; \frac{\text{rng}_i}{\text{rdg}_i}\right) \cdot \frac{1-\lambda^2}{\lambda^2}}}_{\text{phase and power factor dependency}} \right) \qquad n \in \{1,2,3\}\,. \tag{5.18}$$

In Equation (5.18), P_n denotes the power analyzer's active power per phase n and the phase uncertainty k_a is frequency dependent. As the largest contribution to the active power is the spectral component of the fundamental, the phase uncertainty k_a is determined with a frequency of 70 Hz and equates to k_a =$5.35 \cdot 10^{-3\circ}$. The maximum operator max in Equation (5.18) gives the maximum value of its three arguments. The power factor λ is for all experiments approximately constant with $\lambda = 0.3$. The low power factor λ results from the relatively high dc voltage U_{dc} set at the power supply. The dc voltage was chosen relatively high such that in turn the power analyzers voltage uncertainty is low. Summing up the power measurement uncertainty ΔP_n of each motor phase results in the measurement uncertainty of the power analyzer ΔP_{ac}:

$$\Delta P_{ac} = \sum_{n=1}^{3} \Delta P_n. \tag{5.19}$$

5.4.4. Results

The settings and results of the experiments are listed in Table 5.1 and illustrated in Figure 5.6(a) and Figure 5.6(b). The magenta color stands for the ac power P_{ac} directly determined by the power analyzer, and the blue lines stand for the ac power obtained by the calorimetric method $P_{c\,ac}$. For both measurement results, the corresponding worst case uncertainty bound is shown. The first half of experiments shown in Figure 5.6(a) cover a high power brake load with approximately 1.6 kW inverter ac power. The experiments in Figure 5.6(b) illustrate the results of the low power operating point with approximately 480 W.

A common result of all experiments is, that the uncertainty bounds of the calorimetrically

Table 5.1.: Experiments for evaluating the ac power measurements with the power analyzer and the calorimetric measurement.

Nr.	AAF	Calorimetry $P_{cac} \pm \Delta P_{cac}$ W	ΔP_{dc} W	ΔP_{cal} W	Power Analyzer $P_{ac} \pm \Delta P_{ac}$ W
1	off	1584.98 ± 2.18	1.39	0.79	1583.86 ± 12.29
2	on	1584.77 ± 2.18	1.39	0.79	1581.43 ± 12.42
3	off	483.43 ± 1.25	0.46	0.79	482.97 ± 3.74
4	on	483.33 ± 1.25	0.46	0.79	480.45 ± 3.76

determined ac power P_{cac} are smaller than those directly obtained from the power analyzer, as shown in Table 5.1. By comparing the high power operating points from experiment number 1 and 2 with the low power experiments it turns out that the uncertainty bounds of both methods increase differently: a four times higher ac power results in a four times higher uncertainty bound of the power analyzer ΔP_{ac}. In contrast, the calorimetric uncertainty just increases by a factor of around two. The smaller increase can be explained by analyzing Equation (5.11). The uncertainty bounds of the calorimetric ac power ΔP_{cac} calculates from the error bounds of the dc power measurement ΔP_{dc} plus the lumped expressions ΔP_{cal} resulting from the calorimetric measurement principle. The uncertainty of the dc power measurement ΔP_{dc} comes from the voltmeters and the current shunt inaccuracy. Depending on the dc current range, the dc power measurement uncertainty ΔP_{dc} scales with approximately 0.085 %. The calorimetric uncertainty ΔP_{cal} (see Equation (5.11)) comes from the inverter supply measurement uncertainty ΔP_{inv1} and ΔP_{inv2}, the uncertainty of the dc heat power ΔP_{heat} and imperfections of the temperature compensation $\frac{\Delta\delta}{R_{\text{th}}}$. The largest contribution to the uncertainty ΔP_{cal} comes from imperfections of the temperature compensation $\frac{\Delta\delta}{R_{\text{th}}}$. A proportional–integral controller compensates for the temperature rise independently of the operating point, resulting in an almost constant uncertainty ΔP_{cal} of 790 mW. The design of the proportional–integral controller requires precise tuning, as the control process is nonlinear, due to the lacking of a cooling mechanism. Summing up, the calorimetric method provides high accuracy over a wide measurement range as long as the constant error term is sufficiently small compared to the ac power.

As can be seen from Figure 5.6(b), the results from the calorimetric method and the power analyzer do overlap for all experiments. Therefore, it can be concluded, that both

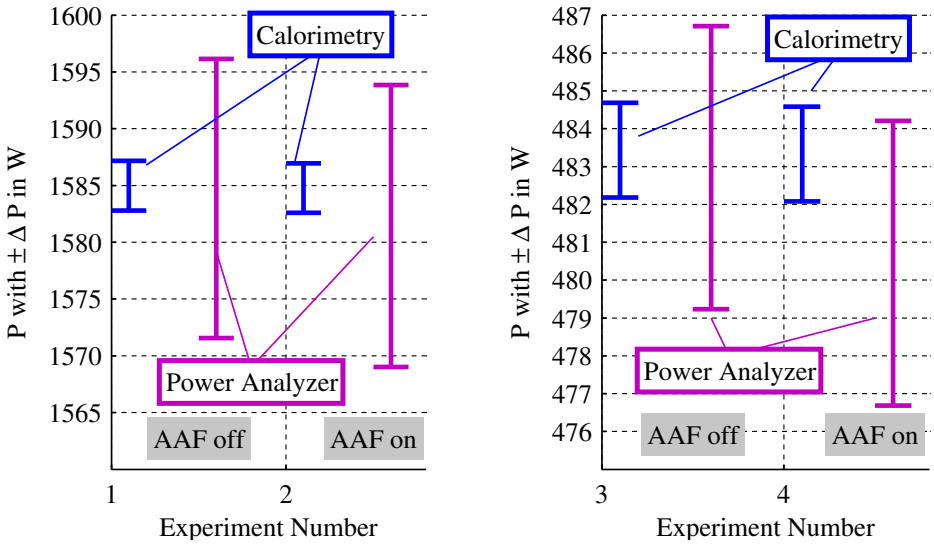

(a) High power operating point.

(b) Low power operating point.

Figure 5.6.: Results for two operating points at 250 V dc voltage. The two colors denote the ac power obtained by the calorimetric method P_{cac} and the ac power directly determined by the power analyzer P_{ac}.

methods produce, within their uncertainty bound, correct results. However, a difference of 2.5 W in the power analyzer's result can be observed by comparing experiment number 1 with 2. The same difference in P_{ac} can be found by comparing the low power operating point in experiment number 3 with 4. The only difference between experiment number 1 and 2 and experiment number 3 and 4 is the activation of the power power analyzer's AAF. Hence, the most reasonable interpretation is, that the AAF with its 100 kHz cutoff frequency attenuates high frequency signal components which contribute to the ac power. The finding is consistent with the simulations of the previous chapter. Both, the simulation and the measurements show that a limited measurement bandwidth can result in a power measurement error in the range of some watt.

In order to evaluate the effect of activating the power analyzer's AAF in the current setup, the ac signals of the test stand are further analyzed. A spectral analysis with an oscilloscope and careful suppression of electromagnetic interference showed ringing of the ac signals. The dominant frequency of the overshoot depicted in Figure 5.1(b) is 1.7 MHz. The power dissipated in this frequency range is only recognized by the power analyzer if the AAF is deactivated.

Basically, the power analyzer's bandwidth should not be reduced by activating the AAF,

if accurate power measurements are required. The utilization of a wide bandwidth is additionally recommended in the article [82]. Deactivating the power analyzers AAF allows for measuring broadband signals from an inverter with the widest bandwidth available. A deactivated AAF will result in aliasing, as the power analyzer samples with a rate of 1 MHz and its bandwidth is 10 MHz. Therefore, it can be essential to activate the AAF for measurements like harmonic analysis of voltage and current signals for example. The results show however, that the aliasing error of the power analyzer has a smaller influence on power measurements as a bandwidth limitation. Therefore, it is recommended to utilize the full measurement bandwidth of a power analyzer, if accurate power measurements are required.

5.5. Summary

The objectives of this section are first to, present a method providing a reference power result and second, to evaluate the simulation from Chapter 4 with real measurements from an actual drivetrain.

The key strength of the presented calorimetric method is, that the active ac power $P_{\mathrm{c\,ac}}$ is obtained without measuring ac signals. Instead the dc supply power reduced by the measured power losses of inverter plus auxiliaries are measured. The power loss measurement uses a calorimetric method which is inherently independent of the signal's bandwidth and shape. An error caused by the bandwidth limitation can therefore be excluded. As shown in the experimental section, the uncertainty bounds of the presented method are smaller than the power analyzer's bounds. Although the realized calorimetric measurement provides already high accuracy, it can be further improved by optimizing the temperature controller and the dc power measurement. Because of the provided accuracy and the exclusion of a bandwidth limitation by principle, the combined calorimetric method is well suited for providing a reference result for the active power. The trade-off for the high accuracy is however the longer measurement time.

Furthermore, the experiments showed the influence of an activation of the power analyzer's AAF. The change in the power analyzer's result coincides with the investigation from Chapter 4 and it can be stated that resonances have to be acquired accurately for

obtaining a power measurement result with a low level of uncertainty. Therefore it is important to inspect voltage and current signals with a high speed acquisition device prior to measurements with a power analyzer.

Although the calorimetric method offers desirable properties in terms of the achievable measurement uncertainty and unlimited bandwidth, it has a drawback in terms of measurement time. The measuring time depends on the thermal time constant τ_{th} which is approximately $\tau_{\mathrm{th}} \approx 30\,\mathrm{min}$ for the constructed calorimeter. The measuring time is therefore in the range of some hours. All faster changes of the ac power are attenuated and averaged in the measurement result. Therefore it is not possible to evaluate transient operating points of the drive with the presented closed, balanced type calorimeter. There exist other types of calorimeter with faster measurement times. For example open type calorimeter evaluate the temperature rise of a coolant for measuring the loss power. Therefore the time constant τ_{th} can be much shorter mainly due to a reduced thermal resistance R_{th} from the inverter to the coolant. Open type calorimeter require however measurements of the mass flow rate. Depending on the coolant medium, liquids or gases, accurate mass flow measurements can be a complex topic with numerous sources of measurement uncertainties.

6

Summary and Outlook

This thesis deals with power measurement of electric drives with the focus on power measurement on the ac side of the inverter. Power measurement with high accuracy on the ac side is challenging for two reasons. Firstly, the measurement chain must provide sufficient bandwidth for the acquisition of the inverter's switching signals and must have a flat frequency response, high sampling rate and high amplitude resolution. Secondly, in order to achieve the required measurement accuracy, a reference measurement with high accuracy is required for comparison. It is not possible to obtain a reference for the power on the ac side by direct measurements, as no sensors are available for measuring the current with high accuracy and wide bandwidth. The present thesis therefore answers the questions which spectral signal components must be included in the measurement bandwidth, how a bandwidth limitation can be avoided and how a

reference power measurement can be carried out with high accuracy on the ac side of an inverter.

A secondary measurement problem in calculating the active power is the noise from the measurement chain and the detection of an integration interval. Although uncorrelated measurement noise can increase the fluctuation of the measured active power, it will cancel out in the mean. Similarly, a nonoptimal determination of an integration interval increases the measurement uncertainty. The determination of an integration interval is inherently prone to sub optimal results because of the possibly asynchronous run of the motor's fundamental frequency and the inverter's switching frequency. A situation with an asynchronous run of inverter switching and motor fundamental is for example the utilization of a randomized inverter switching frequency or DTC. However, the error due to a nonoptimal averaging interval can be made sufficiently small by increasing the averaging interval. Therefore, beside the accuracy of voltage and current sensors, the resulting accuracy of a power measurement is limited by the bandwidth limitation of the measurement chain.

The main question of this thesis is which bandwidth is actually required for achieving a desired measurement accuracy. On one side, it seems to be clear that the contribution to the overall power decreases with an increasing bandwidth because of the rectangular voltage waveform and the overall resistive inductive load behavior of the motor. On the other side it is unclear whether this assessment is an oversimplification of the real measurement. Therefore this thesis analyzes the bandwidth requirement in detail on basis of simulations and measurements. Firstly, a impedance model is developed such that the effect of a bandwidth limitation can be evaluated on basis of simulations. Then the simulation of the bandwidth limitation is carried out in the frequency domain for obtaining exact results. Finally, the simulation-based results are verified by comparing a power analyzer's measurement with a calorimetric reference result of an actual drive.

The required bandwidth results from the spectral composition of voltage and current. To evaluate the spectral contribution to the overall power, the interaction between voltage and current is analyzed. The load impedance and the inverter's switching pattern govern this interaction. Therefore, a drive circuit model is developed for simulation-based investigations concerning the bandwidth limitation. The model consists of three phases and it includes cabling and motor. The developed model contains the low as well as the high frequency behavior of an electric drive. At higher frequencies, effects like

overshoots and ringing can be present at electric drives. An analysis of the model reveals that motor and cabling can form a resonance circuit. The resonance frequency can range up to some 10 MHz and the circuit is excited by the switching voltage signal from the inverter. The verification of the model is carried out by comparing simulated model data with measurements in the time domain. The comparison shows agreement between simulation and measurement data. In further investigations, the model can be further improved concerning the damping resistor R_{MH}. The damping resistor R_{MH} summarizes all physical damping effects of the circuit at the resonance frequency. As discussed in Chapter 3, the proximity and skin effect are supposed to be the main cause for the damping resistor R_{MH}. This suggestion can be further investigated and additionally the frequency dependence can be included in the model. Furthermore, further research can include a change of the circuit topology with the objective of a more physical representation.

The impedance model of the drive is utilized to simulate the voltage and current signals of an electric drive for evaluating the bandwidth limitation. The switching voltage waveform is modeled as rectangularly shaped pulses and the interaction with the impedance model is computed in the frequency domain. The bandwidth limitation is evaluated by increasing the measurement bandwidth and computing the difference to a reference power determined at a considerably higher bandwidth. Since the evaluation in the frequency domain corresponds to filtering with an ideal but unfeasible low pass, further studies could incorporate the utilization of practical low-pass filters. For insightful interpretations, the model is analyzed in three stages ranging from the low frequency behavior over the high frequency behavior up to the complete impedance model. These investigations show that in case of no resonance, a bandwidth of some hundreds of kHz is sufficient for accurate power measurements with uncertainties within the ppm range.

The high frequency part of the model generates losses in the range of some Watt. The evaluation of the complete impedance reveals that the resonance circuit has to be considered in the measurement bandwidth. If the bandwidth does not cover the resonance frequency, the measurement result has an error in the Watt range. An interesting point for further contributions would be the question, how the drive topology influences the loss power in the resonance circuit. In the research carried out, the shielding of the cable is connected to the inverter and to the motor side. This shielding scheme minimizes electromagnetic interference radiation but it is prone to ground loops.

An open question is, how this connection scheme influences the losses and if there are simple rules for a rough evaluation in terms of required measurement bandwidth and resulting uncertainty. A further open question is the influence of other inverter circuit designs and topologies on the power measurement's uncertainty. Further work needs to find out whether a different switching characteristic of for example silicon carbide (SiC) semiconductors or multilevel inverter topologies have a considerable influence on the results of this thesis.

To verify the results of the simulation, power measurements are carried out on an actual electric drive. Since manufacturers of commercial drives do not provide all implemented software and hardware details, it is possible that the drive control is highly optimized and the signal waveforms cannot be classified as *typical* and *representative*. Therefore, the experiments are carried out on a self-built electric drive, such that unexpected behavior can be excluded. The electric drive consists of a three-phase inverter based on IGBT with a control board designed for the application. The inverter drives a PMSM with the vector control algorithm FOC and SVPWM. For evaluating the required bandwidth for accurate measurements, a combined calorimetric and dc based power measurement is used and serves as reference result on the ac side. The calorimetric approach guarantees the independence of any bandwidth limitation, as calorimeter operate on thermal principles. The comparison of the calorimetric measurement with the power analyzer supports the simulation-based findings. In the experiment, the power analyzer is configured to cover the resonance frequency in one case and not in the other. All experiments show, that the power analyzer's result for the ac power is too small if its bandwidth does not cover the resonant frequency. In the experiment, the resonance frequency is 1.7 MHz and the associated losses are approximately 2.5 W. Therefore, practitioners as well as measurement equipment manufacturers have to bear in mind, that power measurements of the ac side can be corrupted by a bandwidth limitation in the range of some Watt because of high frequency resonance circuits.

To reduce this measurement uncertainty, damping circuits and chokes can be applied to the drive for attenuating the resonance effects. However, such damping methods are not always applicable because of additional cost and power losses. Therefore, the power analyzer and measurement probes should provide a bandwidth such that high frequency losses can be determined. A practical solution is to check the signals of the drive for resonance effects with a high-speed acquisition device such as an oscilloscope.

If resonances are present but the frequency is not covered by the power analyzer's bandwidth, a possible solution could be to estimate the energy in the resonance circuit by evaluating the peak values of the high frequency signal parts of voltage and current with the oscilloscope. This energy can then be used to correct the result of the power analyzer by adding the additional electrical power of the resonance circuit, taking into account the switching frequency of the inverter. However, the uncertainty of this practical approach is hardly assessable and could also be a topic for further research.

A improvement of the reference measurement can be obtained by optimizing the calorimetric measurement. The constructed calorimeter suffers from a long measurement time in the range of some hours. Therefore, further research could include the reduction of the calorimetric measurement time. This research can yield in the direction of other types of calorimeters and advanced measurement techniques. For example, liquid or gas cooled calorimeter can be constructed with a smaller time constant resulting in a faster temperature step response. A further method for reducing the measurement time could be the evaluation of a temperature rises instead of an absolute level. However, the construction and especially the uncertainty evaluation is then a challenging task.

Appendix

A

Symbols and Acronyms

A.1. Table of Symbols

Symbol	Description
$c_{p\,\mathrm{Air}}$	Specific heat capacity of air
$c_{p\,\mathrm{Al}}$	Specific heat capacity of aluminum
C_{th}	Thermal heat capacity
k	Frequency index variable for Fourier Series representation or depending on context integer variable
d	Distance between motor cables
d_{cal}	Insulation material thickness of the calorimeter

δ	Temperature difference between inside and outside the calorimeter
$\Delta\eta$	Measurement uncertainty of the device efficiency η
δP_{in}	Measurement uncertainty of the active input power of a device
δP_{out}	Measurement uncertainty of the active output power of a device
ΔP_{cal}	Measurement uncertainty of the calorimetric measurement; the dc power measurement is not included
ΔP_{in}	Upper bound of the measurement uncertainty of the active input power of a device. This expression can be also referred to as *measurement uncertainty of the input power*
$\frac{\Delta P_{\text{in}}}{P_{\text{in}}}$	Relative measurement uncertainty of the active input power
ΔP_{out}	Upper bound of the measurement uncertainty of the active output power of a device. This expression can be also referred to as *measurement uncertainty of the output power*
$\frac{\Delta P_{\text{out}}}{P_{\text{out}}}$	Relative measurement uncertainty of the active output power
ΔP	Measurement uncertainty of the active power
$\frac{\Delta P}{P}$	Relative measurement uncertainty of the active power
E_{abs}	Absolute error
e_{rel}	Relative error
e_{tar}	Target measurement uncertainty
ε_0	Vacuum permittivity
η	Computed efficiency of a device
η_{inv}	Efficiency of an inverter
η_{true}	True efficiency of a device
f_{a}	Analog bandwidth of analog measurement path
$f_{\text{a,ref}}$	Reference bandwidth of analog measurement path for computations
f_D	Oscillation frequency of a damped RLS series circuit
F_i	Relative current measurement uncertainty of the power analyzer
f_{M}	Fundamental electric frequency of motor current and voltage
f_{res}	Resonance frequency of motor's cabling and winding
f_{S}	Sampling rate
f_{Sw}	Switching frequency of inverter with PWM-Strategy
F_v	Relative voltage measurement uncertainty of the power analyzer
$i(t)$, $i[n]$	Current signal in the continuous and discrete domains
k_a	Phase uncertainty of the power analyzer

λ	Power factor
M	Integer variable
μ_0	Vacuum permeability
N	Period of a discrete signal in samples or integer variable
ρ	Electrical resistivity of copper
ρ_{Air}	Density of air
ρ_{Al}	Density of aluminum
P	True active power
$\bar{P}$	Computed active power
P_{ac}	Power on the ac side, i.e., between the motor and inverter. Unless otherwise noted this power is measured with a power analyzer
P_{cac}	Power on the ac side, i.e., between motor and inverter measured determined with the combined calorimetric method
P_{dc}	Power on the dc side, i.e., between the power supply and inverter
P_{heat}	Power of heating unit
P_{in}	Measured active input power of a device
$P_{\mathrm{in,true}}$	True active input power of a device
P_{inv1}	Inverter supply power and fan power during normal operation
P_{inv2}	Inverter supply power and fan power during heating phase
P_L	Loss power of the inverter
P_{out}	Measured active output power of a device
$P_{\mathrm{out,true}}$	True active output power of a device
P_{ref}	Computed power at the reference bandwidth $f_{\mathrm{a,ref}}$
Q	Quality factor of a resonance circuit
R_s	Current shunt
T	Period of a continuous signal or the common period of switching frequency f_{Sw} and fundamental frequency f_{M}
T_i	Inside temperature of the calorimeter
T_o	Outside temperature of the calorimeter
t_{th}	Transient time with a changing temperature inside the calorimeter
τ_{th}	Thermal time constant of a calorimeter, i.e., the required time to reach 63 % of its finial temperature value for a constant power
$u(t)$, $u[n]$	Voltage signal in the continuous and discrete domains
U_s	Voltage drop across the current shunt

V_{inv}	Volume of the inverters IGBT modules plus heat sink
W	Energy
z	Number of pole pairs of an electric motor

A.2. Table of Acronyms

Acronym	Description
AAF	Anti-Aliasing filter.
ADC	Analog-to-Digital Converter.
CEMF	Counter-electromotive force.
CMRR	Common Mode Rejection Ratio.
DTC	Direct Torque Control.
EMI	Electromagnetic interference.
EMC	Electromagnetic compatibility.
FIR	Finite impulse response.
FOC	Field-oriented control.
FS	Fourier series.
GUM	Guide to the Expression of Uncertainty in Measurement.
IIR	Infinite impulse response.
MOSFET	Metal–oxide–semiconductor field-effect transistor.
PI	Proportional–integral controller.
PLL	Phase locked loop.
PWM	Pulse-width modulation.
RMS	Root Mean Square.
SiC	Silicon carbide.
SMD	Surface Mounted Devices.
SVPWM	Space-vector pulse-width modulation.

B

Series RLC Circuit

Description

A series RLC circuit consists of an inductor L, a capacitor C and a resistor R, as shown in Figure B.1. The differential equation of the inductor L is given by:

$$u_l(t) = L \cdot \frac{\mathrm{d}i(t)}{\mathrm{d}t}, \tag{B.1}$$

with the inductor voltage $u_l(t)$, the inductance L and the current $i(t)$. The capacitor current $i(t)$ results from

$$i(t) = C \cdot \frac{\mathrm{d}u_c(t)}{\mathrm{d}t}, \tag{B.2}$$

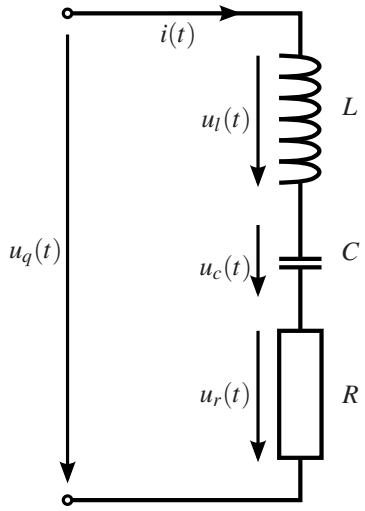

Figure B.1.: series RLC circuit with an inductor L, a capacitor C and a resistor R.

with the capacity C and the capacitor voltage $u_c(t)$. The voltage drop $u_r(t)$ at the resistor is the product of the current $i(t)$ times the resistance R:

$$u_r(t) = R \cdot i(t)\,. \tag{B.3}$$

The second order differential equation of the RLC series circuit can be derived by applying Kirchhoff's second law, which states that the sum of all voltages in a loop is the source voltage $u_q(t)$:

$$u_l(t) + u_c(t) + u_r(t) = u_q(t)\,. \tag{B.4}$$

Substituting Equation (B.1), Equation (B.2) and Equation (B.3) in Equation (B.4) yields to

$$L \cdot \frac{\mathrm{d}i(t)}{\mathrm{d}t} + u_c(t) + R \cdot i(t) = u_q(t) \tag{B.5}$$

$$L \cdot C \cdot \frac{\mathrm{d}^2 u_c(t)}{\mathrm{d}t^2} + R \cdot C \cdot \frac{\mathrm{d}u_c(t)}{\mathrm{d}t} + u_c(t) = u_q(t) \tag{B.6}$$

$$\frac{\mathrm{d}^2 u_c(t)}{\mathrm{d}t^2} + \frac{R}{L} \cdot \frac{\mathrm{d}u_c(t)}{\mathrm{d}t} + \frac{1}{L \cdot C} \cdot u_c(t) = \frac{1}{L \cdot C} u_q(t)\,. \tag{B.7}$$

The second order differential equation Equation (B.7) is rewritten in a more general

form using the angular resonance frequency ω_{res} and the attenuation α [137, p. 282]:

$$\frac{R}{L} = 2 \cdot \alpha \tag{B.8}$$

$$\frac{1}{L \cdot C} = \omega_{\text{res}}^2 \tag{B.9}$$

$$\frac{\mathrm{d}^2 u_c(t)}{\mathrm{d}t^2} + 2 \cdot \alpha \cdot \frac{\mathrm{d}u_c(t)}{\mathrm{d}t} + \omega_{\text{res}}^2 \cdot u_c(t) = \omega_{\text{res}}^2 \cdot u_q(t)\,. \tag{B.10}$$

Step Response

The step response of the RLC circuit depends on the zeros of the characteristic polynomial $\lambda^2 + 2 \cdot \alpha \cdot \lambda + \omega_{\text{res}}^2$. In case of a weak damping $\alpha^2 < \omega_{\text{res}}^2$ (corresponds to $R < 2 \cdot \sqrt{\frac{L}{C}}$), and zero initial conditions, i.e.

$$u_c(0) = 0\,\text{V} \qquad\qquad \left.\frac{\mathrm{d}u_c(t)}{\mathrm{d}t}\right|_{t=0} = 0\,\text{V},$$

the step response computes to [138, Tab. 3.5-5]

$$\begin{aligned}
u_q(t) &= \begin{cases} 0 & t < 0 \\ U_q & t \geq 0 \end{cases} \\
u_c(t) &= U_q \cdot \left(1 - \frac{\omega_{\text{res}}}{\omega_D} \cdot \mathrm{e}^{-\alpha \cdot t} \cdot \sin(\omega_D \cdot t + \phi)\right) \\
\omega_D &= \sqrt{\omega_{\text{res}}^2 - \alpha^2} \\
\phi &= \arccos \frac{\alpha}{\omega_{\text{res}}}
\end{aligned}$$

with the angular oscillation frequency ω_D. For small values of the attenuation α the angular oscillation frequency ω_D is approximately the angular resonance frequency ω_{res}.

The quality factor Q is a function of the damping α and the angular resonant frequency ω_{res}:

$$Q = \frac{\omega_{\text{res}}}{2 \cdot \alpha} = \frac{1}{R} \cdot \sqrt{\frac{L}{C}}. \tag{B.11}$$

A typical step response and the corresponding envelope is shown in Figure B.2.

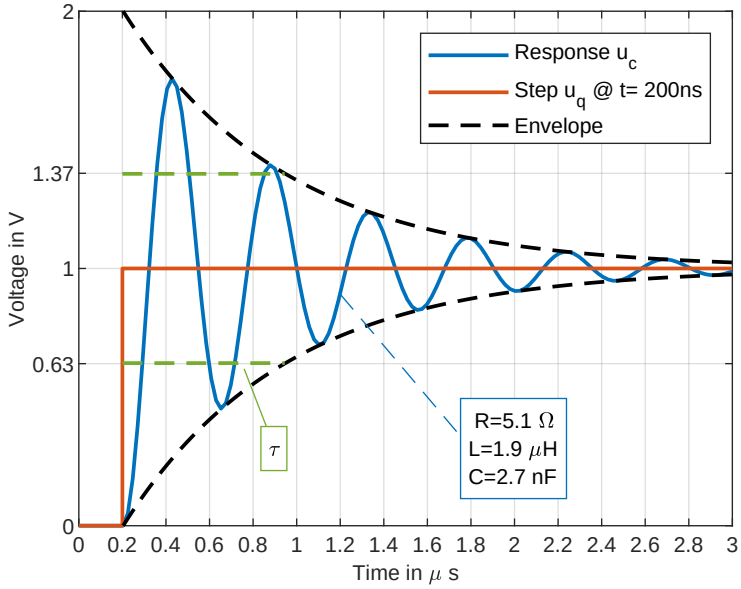

Figure B.2.: Simulated step response with the parameters of Chapter 3.

Parameter Determination of Step Response

The attenuation α can be determined from the step response, as it corresponds to the 63 % time constant of the amplitude decay, denoted by $\tau = \alpha^{-1}$, as shown in Figure B.2. For small deviation between the oscillating angular frequency ω_D and the angular resonance frequency ω_{res}, i.e. $\omega_D \approx \omega_{\text{res}}$ or $\alpha^2 \ll \omega_{\text{res}}^2$, the envelope of the oscillation is

$$U_q \cdot \left(1 - \mathrm{e}^{-\alpha \cdot t}\right) \leq u_c(t) \leq U_q \cdot \left(1 + \mathrm{e}^{-\alpha \cdot t}\right). \qquad \text{for} \quad \omega_D \approx \omega_{\text{res}} \tag{B.12}$$

Equation (B.12) can be expressed with the 63 % time constant τ of the amplitude decay of the envelope

$$U_q \cdot \left(1 - \mathrm{e}^{-\frac{t}{\tau}}\right) \leq u_c(t) \leq U_q \cdot \left(1 + \mathrm{e}^{-\frac{t}{\tau}}\right) \qquad \text{for} \quad \omega_D \approx \omega_{\text{res}}. \tag{B.13}$$

With Equation (B.13), the time constant τ can be computed from the envelope with

$$\tau = -\frac{t}{\ln\left(\pm\left(1 - \frac{u_c(t)}{U_q}\right)\right)} \qquad \text{for} \quad \omega_D \approx \omega_{\text{res}}. \tag{B.14}$$

It should be noted that Equation (B.14) must be evaluated for the peak values when the oscillation touches the envelope, as illustrated in Figure B.2.

The measurable time constant τ can be related to the damping α, to the parameters L and R and with Equation (B.11) to the quality factor Q:

$$\tau = \frac{1}{\alpha} = \frac{2 \cdot L}{R} \tag{B.15}$$

$$\tau = \frac{2 \cdot Q}{\omega_{\text{res}}} \tag{B.16}$$

The measurable angular oscillation frequency ω_D can be used to determine the resonance frequency ω_{res} if the attenuation α or the quality factor Q is already known:

$$\omega_D = \sqrt{\omega_{\text{res}}^2 - \alpha^2} = \omega_{\text{res}} \cdot \sqrt{1 - \frac{1}{(2 \cdot Q)^2}} \quad \rightarrow \qquad \omega_{\text{res}} = \sqrt{\omega_D^2 + \alpha^2} = \sqrt{\omega_D^2 + \frac{1}{\tau^2}}. \tag{B.17}$$

If the inductance L is additionally known, the capacity C can be calculated from ω_D, τ and L by applying Equation (B.17) to Equation (B.9):

$$C = \frac{1}{L \cdot \left(\omega_D^2 + \frac{1}{\tau^2} \right)}. \tag{B.18}$$

C

Measurement Uncertainty of Efficiency

Definition of Efficiency

The efficiency of a device η is defined as the ratio of the active output power P_{out} to the active input power P_{in}:

$$\eta = \frac{P_{\text{out}}}{P_{\text{in}}}. \tag{C.1}$$

Worst Case Uncertainty

The worst case uncertainty of the efficiency $\Delta\eta$ is computed by uncertainty propagation from its definition in Equation (C.1). Therefore the efficiency η from Equation (C.1) is derived with respect to the input power P_{in} and output power P_{out}. The absolute values of the partial derivatives are weighted with the upper bound of the measurement uncertainty of the input ΔP_{in} and output ΔP_{out} power defined in Equation (1.3). The sum of the weighted partial derivatives yields the worst case measurement uncertainty of the efficiency $\Delta\eta$:

$$\Delta\eta = \left|\frac{\partial\eta}{\partial P_{\text{out}}}\right| \cdot \Delta P_{\text{out}} + \left|\frac{\partial\eta}{\partial P_{\text{in}}}\right| \cdot \Delta P_{\text{in}} \tag{C.2}$$

$$= \left|\frac{1}{P_{\text{in}}}\right| \cdot \Delta P_{\text{out}} + \left|-\frac{P_{\text{out}}}{P_{\text{in}}^2}\right| \cdot \Delta P_{\text{in}}. \tag{C.3}$$

The general definition of the worst case uncertainty of the efficiency $\Delta\eta$ in Equation (C.3) can be further simplified for the case of positive input power P_{in} and output power P_{out}:

$$\Delta\eta = \frac{1}{P_{\text{in}}} \cdot \Delta P_{\text{out}} + \frac{P_{\text{out}}}{P_{\text{in}}^2} \cdot \Delta P_{\text{in}}. \tag{C.4}$$

The expression from Equation (C.4) is further simplified such that the *relative* worst case measurement uncertainty of the input power $\frac{\Delta P_{\text{in}}}{P_{\text{in}}}$ and the output power $\frac{\Delta P_{\text{out}}}{P_{\text{out}}}$ can be inserted directly. Therefore, the first term is expanded by $\frac{P_{\text{out}}}{P_{\text{out}}} = 1$ and afterwards the definition of the efficiency η from Equation (C.1) is reapplied:

$$\Delta\eta = \frac{1}{P_{\text{in}}} \cdot \underbrace{\frac{P_{\text{out}}}{P_{\text{out}}}}_{=1} \cdot \Delta P_{\text{out}} + \frac{P_{\text{out}}}{P_{\text{in}}^2} \cdot \Delta P_{\text{in}} \tag{C.5}$$

$$= \underbrace{\frac{P_{\text{out}}}{P_{\text{in}}}}_{=\eta} \cdot \frac{\Delta P_{\text{out}}}{P_{\text{out}}} + \underbrace{\frac{P_{\text{out}}}{P_{\text{in}}}}_{=\eta} \cdot \frac{\Delta P_{\text{in}}}{P_{\text{in}}} \tag{C.6}$$

$$= \eta \cdot \left(\frac{\Delta P_{\text{out}}}{P_{\text{out}}} + \frac{\Delta P_{\text{in}}}{P_{\text{in}}}\right). \tag{C.7}$$

In Equation (C.7) the expression $\frac{\Delta P_{\text{out}}}{P_{\text{out}}}$ corresponds to the *relative* worst case measurement uncertainty of the output power and $\frac{\Delta P_{\text{in}}}{P_{\text{in}}}$ to the *relative* worst case measurement uncertainty of the input power respectively.

Equation (C.7) can be interpreted such that the worst case uncertainty $\Delta\eta$ of the efficiency η is the sum of the relative measurement uncertainties of input and output power $\frac{\Delta P_{\text{in}}}{P_{\text{in}}}$ and $\frac{\Delta P_{\text{out}}}{P_{\text{out}}}$ weighted by the true efficiency η.

D

Quasi Synchronous Sampling

Periodic Signals

Periodic signals in continuous domain:

$$u(t) = u(t + k \cdot T) \qquad i(t) = i(t + k \cdot T) \qquad \forall k \in \mathbb{Z}. \tag{D.1}$$

Sampling with sampling frequency f_S:

$$u[n] = u\left(\frac{n}{f_S}\right) \qquad i[n] = i\left(\frac{n}{f_S}\right) \tag{D.2}$$

In case of synchronous sampling, the product of sampling frequency f_S and signal period T has to be an integer number. A more practical measurement scenario is,

that the sampled signals $u[n]$ and $i[n]$ are periodic with period M, but the sampling frequency f_S matches the signal period T after more than one signal period. This case is called quasi-synchronous sampling. Quasi-synchronous sampling relaxes the synchronous sampling requirement such that the product of sampling frequency f_S and signal period T is a rational number

$$T \cdot N = \frac{M}{f_S} \quad \rightarrow \quad T \cdot f_S = \frac{M}{N} \qquad \frac{M}{N} \in \mathbb{Q} \qquad \text{with} \qquad M,N \in \mathbb{Z} \tag{D.3}$$

In more specific terms, this means that N integer multiples of the continuous signal period T is the span of time as M integer multiples of the sampling frequency f_S. Therefore, the discrete signals are periodic with

$$u[n] = u[n+M] = u\left(\frac{n+M}{f_S}\right) = u\left(\frac{n}{f_S} + N \cdot T\right) \tag{D.4}$$

$$i[n] = i[n+M] = i\left(\frac{n+M}{f_S}\right) = i\left(\frac{n}{f_S} + N \cdot T\right) \tag{D.5}$$

Within quasi-synchronous sampling, subharmonic signal parts are generated in the sampled signal, but they are unavoidable as the signal period T is typically not synchronized with the sampling frequency f_S

Power in Discrete Case

For continuous signals $u(t)$ and $i(t)$, the active power is defined by

$$P = \lim_{T \to \infty} \frac{1}{2T} \int_{-T}^{T} u(t) \cdot i(t) \, \mathrm{d}t. \tag{D.6}$$

In Equation (D.6), the integration interval is chosen to be symmetrical $t \in (-\infty, \infty)$, because then the signal definition range of $u(t)$ and $i(t)$ is the same as the integration range. If the signal definition and integration range are equal, the following derivation is less complex, but the same derivation result is obtained.

Because of the sampling theorem, the continuous signals can be represented with an

infinite series of sinc functions:

$$u(t) = \lim_{K\to\infty} \sum_{n_u=-K}^{K} u[n_u] \cdot \operatorname{sinc}(t \cdot f_S - n_u) \tag{D.7}$$

$$i(t) = \lim_{K\to\infty} \sum_{n_i=-K}^{K} i[n_i] \cdot \operatorname{sinc}(t \cdot f_S - n_i) \tag{D.8}$$

The active power P from Equation (D.6) computes then to

$$P = \lim_{T\to\infty} \frac{1}{2T} \int_{-T}^{T} u(t) \cdot i(t)\,\mathrm{d}t \tag{D.9}$$

$$= \lim_{T\to\infty} \frac{1}{2T} \int_{-T}^{T} \lim_{K\to\infty} \left(\sum_{n_u=-K}^{K} u[n_u] \cdot \operatorname{sinc}(t \cdot f_S - n_u) \right) \left(\sum_{n_i=-K}^{K} i[n_i] \cdot \operatorname{sinc}(t \cdot f_S - n_i) \right) \mathrm{d}t \tag{D.10}$$

The product of the two sums results in expressions in the form of

$$u[n_u] \cdot i[n_i] \cdot \operatorname{sinc}(t \cdot f_S - n_u) \cdot \operatorname{sinc}(t \cdot f_S - n_i)\,. \tag{D.11}$$

The integral of two sinc functions evaluates to

$$I = \lim_{T\to\infty} \int_{-T}^{T} \operatorname{sinc}(t \cdot f_S - n_u) \cdot \operatorname{sinc}(t \cdot f_S - n_i)\,\mathrm{d}t = \begin{cases} 0 & n_u \neq n_i \\ \frac{1}{f_S} & n_u = n_i \end{cases}. \tag{D.12}$$

Therefore, the active power from Equation (D.10) computes to a infinite summation, where a change of variables $T = \frac{M}{f_S}$ is applied:

$$P = \lim_{M\to\infty} \frac{f_S}{2M} \sum_{n=-M}^{M} u[n] \cdot i[n] \cdot \frac{1}{f_S} \tag{D.13}$$

$$= \lim_{M\to\infty} \frac{1}{2M} \sum_{n=-M}^{M} u[n] \cdot i[n]\,. \tag{D.14}$$

As the discrete signals are periodic with period M, the infinite summation gives the

same result as the sum over an integer multiple of the periods M:

$$P = \frac{1}{k \cdot M} \sum_{n=0}^{k \cdot M - 1} u[n] \cdot i[n] \tag{D.15}$$

E

Integration Time Error

The true active power P is computed by integrating and averaging the instantaneous power over one signal period T. In practice, the integration interval is typically chosen to be an integer multiple of the signal period T, as the same result can be obtained and additionally a possible integration time error has a smaller effect on the computed power P. The difference between the true active power P and the power obtained by integrating over an arbitrary time span is evaluated.

The Fourier Series of voltage and current are defined as follows:

$$u(t) = \sum_{k=-\infty}^{\infty} \underline{U}_k \cdot \mathrm{e}^{\mathrm{j}\cdot\frac{2\pi}{T}\cdot t\cdot k} \qquad i(t) = \sum_{k=-\infty}^{\infty} \underline{I}_k \cdot \mathrm{e}^{\mathrm{j}\cdot\frac{2\pi}{T}\cdot t\cdot k} \tag{E.1}$$

$$= \underline{U}_0 + \sum_{k=1}^{\infty} 2\cdot \mathrm{Re}\left(\underline{U}_k \cdot \mathrm{e}^{\mathrm{j}\cdot\frac{2\pi}{T}\cdot t\cdot k}\right) \qquad = \underline{I}_0 + \sum_{k=1}^{\infty} 2\cdot \mathrm{Re}\left(\underline{I}_k \cdot \mathrm{e}^{\mathrm{j}\cdot\frac{2\pi}{T}\cdot t\cdot k}\right) \tag{E.2}$$

Fourier Series coefficients of real signals have the following properties

$$\underline{U}_k = \underline{U}^*_{-k} \qquad \underline{U}^*_k = \underline{U}_{-k} \qquad |\underline{U}_k| = \left|\underline{U}_{-k}\right| \qquad \underline{U}^*_0 = \underline{U}_0 \tag{E.3}$$

$$\underline{I}_k = \underline{I}^*_{-k} \qquad \underline{I}^*_k = \underline{I}_{-k} \qquad |\underline{I}_k| = |\underline{I}_{-k}| \qquad \underline{I}^*_0 = \underline{I}_0 \tag{E.4}$$

The instantaneous power $p(t)$ is then

$$p(t) = u(t) \cdot i(t) \tag{E.5}$$

$$= \lim_{K\to\infty} \left(\sum_{l=-K}^{K} \underline{U}_l \cdot \mathrm{e}^{\mathrm{j}\cdot\frac{2\pi}{T}\cdot t\cdot l} \right) \cdot \left(\sum_{n=-K}^{K} \underline{I}_n \cdot \mathrm{e}^{\mathrm{j}\cdot\frac{2\pi}{T}\cdot t\cdot n} \right) \tag{E.6}$$

$$= \lim_{K\to\infty} \sum_{l=-K}^{K} \sum_{n=-K}^{K} \underline{U}_l \cdot \underline{I}_n \cdot \mathrm{e}^{\mathrm{j}\cdot\frac{2\pi}{T}\cdot t\cdot (l+n)} = \lim_{K\to\infty} \sum_{l=-K}^{K} \sum_{k=-2K}^{2K} \underline{U}_l \cdot \underline{I}_{k-l} \cdot \mathrm{e}^{\mathrm{j}\cdot\frac{2\pi}{T}\cdot t\cdot k} \tag{E.7}$$

$$= \lim_{K\to\infty} \sum_{k=-2K}^{2K} \left(\sum_{l=-K}^{K} \underline{U}_l \cdot \underline{I}_{k-l} \right) \cdot \mathrm{e}^{\mathrm{j}\cdot\frac{2\pi}{T}\cdot t\cdot k} \tag{E.8}$$

The Fourier series coefficients $\underline{P}_k$ of the instantaneous power $p(t)$ are thus

$$\underline{P}_k = \sum_{l=-K}^{K} \underline{U}_l \cdot \underline{I}_{k-l}. \tag{E.9}$$

The true active power P is the integral of the instantaneous power $p(t)$ over a full period T:

$$P = \frac{1}{T} \int_0^T p(t)\,\mathrm{d}t \tag{E.10}$$

$$P = \frac{1}{T} \int_0^T \sum_{k=-\infty}^{\infty} \underline{P}_k \cdot \mathrm{e}^{\mathrm{j}\cdot\frac{2\pi}{T}\cdot t\cdot k} \mathrm{d}t \tag{E.11}$$

For evaluating the integral of Equation (E.11), the integral of the exponential function is

required:

$$b \in \mathbb{Z} \tag{E.12}$$

$$\underline{\varepsilon}(t_0,t,b) = \int_{t_0}^{t_0+t} \mathrm{e}^{\mathrm{j}\frac{2\pi}{T}\cdot b\cdot\tau}\mathrm{d}\tau = \begin{cases} t & b=0 \\ \frac{1}{\mathrm{j}\frac{2\pi}{T}\cdot b}\cdot \mathrm{e}^{\mathrm{j}\frac{2\pi}{T}\cdot b\cdot t_0}\cdot\left(\mathrm{e}^{\mathrm{j}\frac{2\pi}{T}\cdot b\cdot t}-1\right) & b\neq 0 \end{cases} \tag{E.13}$$

$$\underline{\varepsilon}(t_0,t,-b) = \int_{t_0}^{t_0+t} \mathrm{e}^{-\mathrm{j}\frac{2\pi}{T}\cdot b\cdot\tau}\mathrm{d}\tau = \begin{cases} t & b=0 \\ -\frac{1}{\mathrm{j}\cdot\frac{2\pi}{T}\cdot b}\cdot \mathrm{e}^{-\mathrm{j}\cdot\frac{2\pi}{T}\cdot b\cdot t_0}\cdot\left(\mathrm{e}^{-\mathrm{j}\cdot\frac{2\pi}{T}\cdot b\cdot t}-1\right) & b\neq 0 \end{cases} \tag{E.14}$$

$$\underline{\varepsilon}^*(t_0,t,b) = \underline{\varepsilon}(t_0,t,-b) \tag{E.15}$$

The integral of the exponential over a full period T evaluates to

$$\underline{\varepsilon}(t_0,T,b) = \begin{cases} T & b=0 \\ 0 & b\neq 0 \end{cases} \tag{E.16}$$

Therefore the true active power P from Equation (E.11) results in

$$P = \frac{1}{T}\sum_{k=-\infty}^{\infty} \underline{P}_k\cdot\underline{\varepsilon}(0,T,k) = \underline{P}_0 \tag{E.17}$$

$$= \sum_{l=-\infty}^{\infty} \underline{U}_l\cdot\underline{I}_{-l} \tag{E.18}$$

If the instantaneous power is not averaged over an integer number of periods T, the computed power denoted as $P(t)$ is given by

$$P(t) = \frac{1}{t}\int_0^t p(\tau)\,\mathrm{d}\tau = \frac{1}{t}\sum_{k=-\infty}^{\infty} \underline{P}_k\cdot\underline{\varepsilon}(0,t,k) \tag{E.19}$$

The difference between true power P and $P(t)$ is now simplified:

$$P(t)-P = \frac{1}{t}\sum_{k=-\infty}^{\infty} \underline{P}_k\cdot\underline{\varepsilon}(0,t,k) - \underline{P}_0 \tag{E.20}$$

$$= \frac{1}{t}\sum_{k=1}^{\infty} \underline{P}_k\cdot\underline{\varepsilon}(0,t,k) + \underline{P}_{-k}\cdot\underline{\varepsilon}(0,t,-k) + \underline{P}_0 - \underline{P}_0 \tag{E.21}$$

$$= \frac{1}{t} \sum_{k=1}^{\infty} \underline{P}_k \cdot \underline{\varepsilon}(0,t,k) + \underline{P}_k^* \cdot \underline{\varepsilon}^*(0,t,k) \tag{E.22}$$

$$= \frac{1}{t} \sum_{k=1}^{\infty} 2 \cdot \mathrm{Re}(\underline{P}_k \cdot \underline{\varepsilon}(0,t,k)) \tag{E.23}$$

$$= \frac{1}{t} \sum_{k=1}^{\infty} 2 \cdot \mathrm{Re}\left(|\underline{P}_k| \, \mathrm{e}^{\mathrm{j}\varphi_k} \cdot \frac{1}{\mathrm{j}\frac{2\pi}{T} \cdot k} \cdot \left(\mathrm{e}^{\mathrm{j}\frac{2\pi}{T} \cdot k \cdot t} - 1 \right) \right) \tag{E.24}$$

$$= \frac{2}{t} \sum_{k=1}^{\infty} \frac{|\underline{P}_k|}{\frac{2\pi}{T} \cdot k} \cdot \mathrm{Re}\left(\mathrm{e}^{\mathrm{j}\varphi_k} \cdot \mathrm{e}^{-\mathrm{j}\frac{\pi}{2}} \cdot \left(\mathrm{e}^{\mathrm{j}\frac{2\pi}{T} \cdot k \cdot t} - 1 \right) \right) \tag{E.25}$$

$$= \frac{2}{t} \sum_{k=1}^{\infty} \frac{|\underline{P}_k|}{\frac{2\pi}{T} \cdot k} \cdot \mathrm{Re}\left(\mathrm{e}^{\mathrm{j}\left(\frac{2\pi}{T} \cdot k \cdot t + \varphi_k - \frac{\pi}{2}\right)} - \mathrm{e}^{\mathrm{j}\left(\varphi_k - \frac{\pi}{2}\right)} \right) \tag{E.26}$$

$$= \frac{2}{t} \sum_{k=1}^{\infty} \frac{|\underline{P}_k|}{\frac{2\pi}{T} \cdot k} \left(\cos\left(\frac{2\pi}{T} \cdot k \cdot t + \varphi_k - \frac{\pi}{2} \right) - \cos\left(\varphi_k - \frac{\pi}{2} \right) \right) \tag{E.27}$$

$$= \frac{2}{t} \sum_{k=1}^{\infty} \frac{|\underline{P}_k|}{\frac{2\pi}{T} \cdot k} \left(\sin\left(\frac{2\pi}{T} \cdot k \cdot t + \varphi_k \right) - \sin(\varphi_k) \right) \tag{E.28}$$

$$= \frac{2}{t} \sum_{k=1}^{\infty} \frac{|\underline{P}_k|}{\frac{2\pi}{T} \cdot k} \cdot 2 \cdot \sin\left(\frac{\pi}{T} \cdot k \cdot t \right) \cdot \cos\left(\frac{\pi}{T} \cdot k \cdot t + \varphi_k \right) \tag{E.29}$$

$$= 2 \sum_{k=1}^{\infty} |\underline{P}_k| \cdot \frac{\sin\left(\frac{\pi}{T} \cdot k \cdot t\right)}{\frac{\pi}{T} \cdot k \cdot t} \cdot \cos\left(\frac{\pi}{T} \cdot k \cdot t + \varphi_k \right) \tag{E.30}$$

$$= 2 \sum_{k=1}^{\infty} |\underline{P}_k| \cdot \mathrm{sinc}\left(\frac{k \cdot t}{T} \right) \cdot \cos\left(\frac{\pi}{T} \cdot k \cdot t + \varphi_k \right) \tag{E.31}$$

The statement of Equation (E.31) is, that the error caused by a noninteger integration time decreases proportional to $\frac{1}{t}$. Higher frequency portions of the instantaneous power $p(t)$ decrease faster. Because of the error decrease with time, the error caused by an noninteger integration interval can be made sufficiently small by choosing the actual integration interval t large.

Bibliography

[1] P. Waide and C. Brunner, "Energy-efficiency policy opportunities for electric motor-driven systems," *IEA Energy Papers*, p. 132, Jul. 2011.

[2] "The authoritative dictionary of ieee standards terms, seventh edition," *IEEE Std 100-2000*, pp. 1–1362, Dec. 2000.

[3] J. Dannehl, "Regelung von Netzpulsstromrichtern mit LCL-Filter für Antriebe mit kleiner Kapazität im Zwischenkreis," PhD thesis, Christian-Albrechts-Universität zu Kiel, 2012.

[**4**] **D. Lindenthaler** and M. Neumayer, "Improved load modelling for switching power supplies in electrified vehicles," in *Industrial Electronics (ISIE), 2014 IEEE 23rd International Symposium on*, Jun. 2014, pp. 824–829.

[**5**] **D. Lindenthaler**, "Signal-bandwidth evaluation for electric power calculation in PWM driven motors," in *Precision Electromagnetic Measurements (CPEM), 2014 Conference on*, Aug. 2014, p. 2.

[**6**] **D. Lindenthaler** and G. Brasseur, "Signal-bandwidth evaluation for power measurements in electric automotive drives," *IEEE Transactions on Instrumentation and Measurement*, vol. 64, no. 6, pp. 1336–1343, Jun. 2015.

[**7**] **D. Lindenthaler** and G. Brasseur, "Ac power measurements of electric drives: A method incorporating calorimetry and dc measurements only," *E & i Elektrotechnik und Informationstechnik*, vol. 134, no. 2, pp. 197–202, 2017.

[**8**] **D. Lindenthaler** and H. Zangl, "Evaluation of uncertainty in ac power calculation with asynchronously sampled data," *Journal of Physics: Conference Series*, vol. 450, no. 1, p. 012 043, 2013.

[9] M. Ehsani, Y. Gao, and J. M. Miller, "Hybrid electric vehicles: Architecture and motor drives," *Proceedings of the IEEE*, vol. 95, no. 4, pp. 719–728, Apr. 2007.

[10] J. Santiago, H. Bernhoff, B. Ekergård, S. Eriksson, S. Ferhatovic, R. Waters, and M. Leijon, "Electrical motor drivelines in commercial all-electric vehicles: A review," *IEEE Transactions on Vehicular Technology*, vol. 61, no. 2, pp. 475–484, Feb. 2012.

[11] *ISO 6469-3:2011*, Electrically propelled road vehicles – Safety specifications – Part 3: Protection of persons against electric shock, Dec. 2011.

[12] *FIA regulation - appendix J - article 253*, Safety Equipment (Groups N, A, R-GT), Dec. 2017.

[13] F. Zach, *Leistungselektronik*, 5. Aufl. Springer Vieweg, Berlin, Heidelberg, 2015.

[14] R. Krishnan, *Electric Motor Drives: Modeling, Analysis, and Control*. Pearson, 2001.

[15] I. Boldea and S. Nasar, *Electric drives*. Boca Raton: CRC Press/Taylor & Francis, 2017.

[16] J. I. Itoh, N. Nomura, and H. Ohsawa, "A comparison between v/f control and position-sensorless vector control for the permanent magnet synchronous motor," in *Proceedings of the Power Conversion Conference-Osaka 2002 (Cat. No.02TH8579)*, vol. 3, 2002, 1310–1315 vol.3.

[17] D. Casadei, F. Profumo, G. Serra, and A. Tani, "Foc and dtc: Two viable schemes for induction motors torque control," *IEEE Transactions on Power Electronics*, vol. 17, no. 5, pp. 779–787, Sep. 2002.

[18] J. Holtz, "Pulsewidth modulation-a survey," *IEEE Transactions on Industrial Electronics*, vol. 39, no. 5, pp. 410–420, Oct. 1992.

[19] A. M. Hava, R. J. Kerkman, and T. A. Lipo, "Simple analytical and graphical methods for carrier-based PWM-VSI drives," *IEEE Transactions on Power Electronics*, vol. 14, no. 1, pp. 49–61, Jan. 1999.

[20] I. of Electrical and E. Engineers, "Standard definitions for the measurement of electric power quantities under sinusoidal, nonsinusoidal, balanced, or unbalanced conditions," *IEEE Std 1459-2010 (Revision of IEEE Std 1459-2000)*, pp. 1–50, Mar. 2010.

[21] F. Clarke and J. Stockton, "Principles and theory of wattmeters operating on the basis of regularly spaced sample pairs," *Journal of Physics E: Scientific Instruments*, vol. 15, no. 6, p. 645, 1982.

[22] S. Ziegler, R. C. Woodward, H. H. C. Iu, and L. J. Borle, "Current sensing techniques: A review," *IEEE Sensors Journal*, vol. 9, no. 4, pp. 354–376, Apr. 2009.

[23] P. Ripka, "Electric current sensors: A review," *Measurement Science and Technology*, vol. 21, no. 11, p. 112 001, 2010.

[24] M. S. Kim, W. S. Kim, Y. G. Kim, Y. Chong, K. T. Kim, and P. G. Park, "Power calibration system based on josephson sampling voltmeter," in *29th Conference on Precision Electromagnetic Measurements (CPEM 2014)*, Aug. 2014, pp. 738–739.

[25] B. V. Djokić, "Low-frequency quantum-based ac power standard at NRC canada," *IEEE Transactions on Instrumentation and Measurement*, vol. 62, no. 6, pp. 1699–1703, Jun. 2013.

[26] G. Ramm, H. Moser, R. Bergeest, and W. G. K. Ihlenfeld, "PTB standard measuring devices for electric ac power," in *PTB Mitteilungen*, vol. 112, Physikalisch-Technischen Bundesanstalt Braunschweig und Berlin, 2002, pp. 17–22.

[27] J. C. Y. Poon, A. Y. K. Yan, W. K. Sin, D. W. K. Lee, and H. S. Lam, "Setting up of a primary power standard at the standards and calibration laboratory (SCL)," in *2012 Conference on Precision electromagnetic Measurements*, Jul. 2012, pp. 122–123.

[28] *LMG670 precision power analyzer*, ZES Zimmer Electronic Systems GmbH, Sep. 2014.

[29] *WT3000 precision power analyzer - user's manual*, IM 760301-01E, Yokogawa Meters & Instruments Corporation, Feb. 2014.

[30] *PPA5500 kinetiQ user manual*, v2.169, Newtons 4th Ltd, Nov. 2017.

[31] *NORMA 4000/5000 power analyzer operators manual*, Rev.2, 5/12, Fluke Corporation, Jun. 2007.

[32] *IntegraVision PA2200 series power analyzers - data sheet*, 5992-0324EN, Keysight Technologies, Dec. 2017.

[33] *PA3000 power analyzer user manual*, 077-1152-01, Tektronix Inc., Jul. 2017.

[34] *SIRIUS technical reference manual*, Version 1.5.3, Dewesoft GmbH, Dec. 2017.

[35] K. Lang, *Perception eDrive option - data sheet*, b4290-3.0 en, Höttinger Baldwin Messtechnik GmbH, Jul. 2017.

[36] C. E. Shannon, "Communication in the presence of noise," *Proceedings of the IRE*, vol. 37, no. 1, pp. 10–21, 1949.

[37] *Perception eDrive option - data sheet*, PW6001E9-7XB, Hioki E.E. Corporation, Oct. 2017.

[38] R. Friedl and G. Wolf, "Precision measuring equipment for electrical power in the range of audio frequencies," *IEEE Transactions on Instrumentation and Measurement*, vol. 15, no. 4, pp. 227–233, Dec. 1966.

[39] M. Tomota, T. Sugiyama, and K. Yamaguchi, "An electronic multiplier for accurate power measurements," *IEEE Transactions on Instrumentation and Measurement*, vol. 17, no. 4, pp. 245–251, Dec. 1968.

[40] G. Bucci, E. Fiorucci, F. Ciancetta, D. Gallo, C. Landi, and M. Luiso, "Embedded power and energy measurement system based on an analog multiplier," *IEEE Transactions on Instrumentation and Measurement*, vol. 62, no. 8, pp. 2248–2257, Aug. 2013.

[41] L. D. Jovanović, "A novel tdm-based high-precision wattmeter," *IEEE Transactions on Instrumentation and Measurement*, vol. 66, no. 6, pp. 1083–1088, Jun. 2017.

[42] R. S. Turgel, "Digital using a sampling method," *IEEE Transactions on Instrumentation and Measurement*, vol. 23, no. 4, pp. 337–341, Dec. 1974.

[43] M. F. Matouka, "A wide-range digital power/energy meter for systems with nonsinusoidal waveforms," *IEEE Transactions on Industrial Electronics*, vol. IE-29, no. 1, pp. 18–31, Feb. 1982.

[44] R. S. Turgel, "Sampling techniques for electric power measurement," *NBS Technical Note 870*, vol. 76, p. 35, 1975.

[45] A. C. Corney and R. T. Pullman, "Digital sampling laboratory wattmeter," *IEEE Transactions on Instrumentation and Measurement*, vol. IM-36, no. 1, pp. 54–59, Mar. 1987.

[46] G. N. Stenbakken, "A wideband sampling wattmeter," *IEEE Transactions on Power Apparatus and Systems*, vol. PAS-103, no. 10, pp. 2919–2926, Oct. 1984.

[47] G. N. Stenbakken and A. Dolev, "High-accuracy sampling wattmeter," *IEEE Transactions on Instrumentation and Measurement*, vol. 41, no. 6, pp. 974–978, Dec. 1992.

[48] S. Svensson and K.-E. Rydler, "A measuring system for the calibration of power analyzers," *Instrumentation and Measurement, IEEE Transactions on*, vol. 44, no. 2, pp. 316–317, Apr. 1995.

[49] P. Simonson, S. Svensson, and K.-E. Rydler, "A comparison of power measuring systems," *Instrumentation and Measurement, IEEE Transactions on*, vol. 46, no. 2, pp. 423–425, Apr. 1997.

[50] S. Svensson, "A wattmeter standard for the audio frequency range," *IEEE Transactions on Instrumentation and Measurement*, vol. 48, no. 2, pp. 431–433, Apr. 1999.

[51] A. Cataliotti, V. Cosentino, D. D. Cara, A. Lipari, S. Nuccio, and C. Spataro, "A pc-based wattmeter for accurate measurements in sinusoidal and distorted conditions: Setup and experimental characterization," *IEEE Transactions on Instrumentation and Measurement*, vol. 61, no. 5, pp. 1426–1434, May 2012.

[52] E. Houtzager, G. Rietveld, and H. van den Brom, "Switching sampling power meter for frequencies up to 1 MHz," *Instrumentation and Measurement, IEEE Transactions on*, vol. 62, no. 6, pp. 1423–1427, Jun. 2013.

[53] S. Svensson, *Power measurement techniques for nonsinusoidal conditions. The significance of harmonics for the measurement of power and other ac quantities*. Chalmers University of Technology, 1999.

[54] T. Bergsten, V. Tarasso, and K. E. Rydler, "An electrical power reference system up to 1 mhz," in *2016 Conference on Precision Electromagnetic Measurements (CPEM 2016)*, Jul. 2016, pp. 1–2.

[55] A. Cataliotti, V. Cosentino, D. D. Cara, A. Lipari, and S. Nuccio, "A daq-based sampling wattmeter for {ieee} std. 1459-2010 powers measurements. uncertainty evaluation in nonsinusoidal conditions," *Measurement*, vol. 61, pp. 27–38, 2015.

[56] G. Bucci, C. D. Capua, and C. Landi, "Power measurements on high distorted signals: Experimental comparison between two alternative developed device solutions," *Measurement*, vol. 23, no. 3, pp. 151–158, 1998.

[57] P. Arpaia, F. Avallone, A. Baccigalupi, and C. De Capua, "Real-time algorithms for active power measurements on pwm-based electric drives," *Instrumentation and Measurement, IEEE Transactions on*, vol. 45, no. 2, pp. 462–466, Apr. 1996.

[58] J. Maisel, "Error analysis in the measurement of average power with application to switching controllers," NASA, Tech. Rep., 1980.

[59] U. Pogliano, B. Trinchera, M. Lanzillotti, and D. Serazio, "Characterization of resistive dividers for a wideband power analyzer," in *Precision Electromagnetic Measurements (CPEM 2014), 2014 Conference on*, Aug. 2014, pp. 130–131.

[60] M. Grubmüller, B. Schweighofer, and H. Wegleiter, "Development of a differential voltage probe for measurements in automotive electric drives," *IEEE Transactions on Industrial Electronics*, vol. 64, no. 3, pp. 2335–2343, Mar. 2017.

[61] B. Voljc, M. Lindic, and R. Lapuh, "Direct measurement of ac current by measuring the voltage drop on the coaxial current shunt," *Instrumentation and Measurement, IEEE Transactions on*, vol. 58, no. 4, pp. 863–867, Apr. 2009.

[62] A. Delle Femine, D. Gallo, C. Landi, and M. Luiso, "Power-quality monitoring instrument with fpga transducer compensation," *Instrumentation and Measurement, IEEE Transactions on*, vol. 58, no. 9, pp. 3149–3158, Sep. 2009.

[63] G. Crotti, D. Gallo, D. Giordano, C. Landi, and M. Luiso, "A characterized method for the real-time compensation of power system measurement transducers," *IEEE Transactions on Instrumentation and Measurement*, vol. 64, no. 6, pp. 1398–1404, Jun. 2015.

[64] K. Loudière, A. Bréard, C. Vollaire, F. Costa, H. Moussa, and R. Meuret, "Wide band measurements in time domain with current and voltage probes for power losses evaluation and emc measurements on power converters," in *2015 IEEE International Symposium on Electromagnetic Compatibility (EMC)*, Aug. 2015, pp. 1266–1271.

[65] P. Mlejnek and P. Kaspar, "Calibrations of phase and ratio errors of current and voltage channels of energy meter," *Journal of Physics: Conference Series*, vol. 450, no. 1, p. 012 046, 2013.

[66] P. Wen, "A fast and high-precision measurement of distorted power based on digital filtering techniques," *IEEE Transactions on Instrumentation and Measurement*, vol. 41, no. 3, pp. 403–406, Jun. 1992.

[67] C. Gherasim, J. V. den Keybus, J. Driesen, and R. Belmans, "Dsp implementation of power measurements according to the ieee trial-use standard 1459," *IEEE Transactions on Instrumentation and Measurement*, vol. 53, no. 4, pp. 1086–1092, Aug. 2004.

[68] M. Novotny and M. Sedlacek, "Measurement of active power by time domain digital signal processing," *Measurement*, vol. 42, no. 8, pp. 1139–1152, 2009.

[69] L. Zu-Liang, "An error estimate for quasi-integer-period sampling and an approach for improving its accuracy," *IEEE Transactions on Instrumentation and Measurement*, vol. 37, no. 2, pp. 219–222, Jun. 1988.

[70] A. Sarkar and S. Sengupta, "Design and implementation of a high accuracy sampling wattmeter under non-sinusoidal and off-nominal frequency conditions," *Measurement*, vol. 43, no. 3, pp. 312–319, 2010.

[71] V. Backmutsky, V. Zmudikov, A. Agizim, and G. Vaisman, "A new dsp method for precise dynamic measurement of the actual power-line frequency and its data acquisition applications," *Measurement*, vol. 18, no. 3, pp. 169–176, 1996.

[72] M. B. Djurić and Ž. R. Djurišić, "Frequency measurement of distorted signals using fourier and zero crossing techniques," *Electric Power Systems Research*, vol. 78, no. 8, pp. 1407–1415, 2008.

[73] P. B. Petrovic, "Modified formula for calculation of active power and root-mean-square value of band-limited alternating current signals," *IET Science, Measurement Technology*, vol. 6, no. 6, pp. 510–518, Nov. 2012.

[74] F. Leferink, C. Keyer, and A. Melentjev, "Static energy meter errors caused by conducted electromagnetic interference," *IEEE Electromagnetic Compatibility Magazine*, vol. 5, no. 4, pp. 49–55, Apr. 2016.

[75] JCGM, “Evaluation of measurement data - guide to the expression of uncertainty in measurement,” Joint Committee for Guides in Metrology 100, Tech. Rep., 2008.

[76] F. Filicori, D. Mirri, and M. Rinaldi, “Error estimation in sampling digital wattmeters,” *IEE Proceedings A - Physical Science, Measurement and Instrumentation, Management and Education - Reviews*, vol. 132, no. 3, pp. 122–128, May 1985.

[77] C. De Capua and C. Landi, “Measurement station performance optimization for testing of high efficiency variable speed drives,” *Instrumentation and Measurement, IEEE Transactions on*, vol. 48, no. 6, pp. 1149–1154, Dec. 1999.

[78] F. Avallone, C. D. Capua, and C. Landi, “A digital technique based on real-time error compensation for high accuracy power measurement on variable speed drives,” in *IEEE Instrumentation and Measurement Technology Conference Sensing, Processing, Networking. IMTC Proceedings*, vol. 1, May 1997, 201–206 vol.1.

[79] F. Avallone, C. De Capua, and C. Landi, “Metrological performance improvement for power measurements on variable speed drives,” *Measurement*, vol. 21, no. 1–2, pp. 17–24, 1997.

[80] G. Pasini, L. Peretto, and R. Tinarelli, “Study of the accuracy requirements of the instrumentation for efficiency measurements in power conversion systems,” *Instrumentation and Measurement, IEEE Transactions on*, vol. 62, no. 8, pp. 2154–2160, Aug. 2013.

[81] S. M. Schneider, J. Sayago, M. Centner, R. Plath, and U. Schäfer, “Messunsicherheit der leistungsmessung von umrichtergespeisten antrieben im mittelspannungsbereich,” *E & i Elektrotechnik und Informationstechnik*, pp. 1–9, 2017.

[82] E. B. Agamloh, “Power and efficiency measurement of motor-variable-frequency drive systems,” *IEEE Transactions on Industry Applications*, vol. 53, no. 1, pp. 766–773, Jan. 2017.

[83] Z. Song and D. V. Sarwate, “The frequency spectrum of pulse width modulated signals,” *Signal Processing*, vol. 83, no. 10, pp. 2227–2258, 2003.

[84] G. R. Ainslie-Malik, “Mathematical analysis of PWM processes,” PhD thesis, University of Nottingham, 2013.

[85] P. Pillay and R. Krishnan, "Modeling, simulation, and analysis of permanent-magnet motor drives. i. the permanent-magnet synchronous motor drive," *IEEE Transactions on Industry Applications*, vol. 25, no. 2, pp. 265–273, Mar. 1989.

[86] L. Liu, W. Liu, and D. A. Cartes, "Particle swarm optimization-based parameter identification applied to permanent magnet synchronous motors," *Engineering Applications of Artificial Intelligence*, vol. 21, no. 7, pp. 1092–1100, 2008.

[87] S. Bolognani, L. Tubiana, and M. Zigliotto, "Extended kalman filter tuning in sensorless pmsm drives," *IEEE Transactions on Industry Applications*, vol. 39, no. 6, pp. 1741–1747, Nov. 2003.

[88] L. Ran, S. Gokani, J. Clare, K. J. Bradley, and C. Christopoulos, "Conducted electromagnetic emissions in induction motor drive systems. i. time domain analysis and identification of dominant modes," *IEEE Transactions on Power Electronics*, vol. 13, no. 4, pp. 757–767, Jul. 1998.

[89] A. Boglietti and E. Carpaneto, "Induction motor high frequency model," in *Conference Record of the 1999 IEEE Industry Applications Conference. Thirty-Forth IAS Annual Meeting (Cat. No.99CH36370)*, vol. 3, 1999, 1551–1558 vol.3.

[90] A. Boglietti, A. Cavagnino, and M. Lazzari, "Experimental high-frequency parameter identification of ac electrical motors," *Industry Applications, IEEE Transactions on*, vol. 43, no. 1, pp. 23–29, Jan. 2007.

[91] G. L. Skibinski, R. J. Kerkman, and D. Schlegel, "Emi emissions of modern pwm ac drives," *IEEE Industry Applications Magazine*, vol. 5, no. 6, pp. 47–80, Nov. 1999.

[92] S. Chen, T. A. Lipo, and D. Fitzgerald, "Modeling of motor bearing currents in pwm inverter drives," *IEEE Transactions on Industry Applications*, vol. 32, no. 6, pp. 1365–1370, Nov. 1996.

[93] J. M. Erdman, R. J. Kerkman, D. W. Schlegel, and G. L. Skibinski, "Effect of pwm inverters on ac motor bearing currents and shaft voltages," *IEEE Transactions on Industry Applications*, vol. 32, no. 2, pp. 250–259, Mar. 1996.

[94] A. Moreira, T. Lipo, G. Venkataramanan, and S. Bernet, "High-frequency modeling for cable and induction motor overvoltage studies in long cable drives," *Industry Applications, IEEE Transactions on*, vol. 38, no. 5, pp. 1297–1306, Sep. 2002.

[95] S. L. Capitaneanu, B. De Fornel, M. Fadel, F. Jadot, and F. Malrait, "Modelling and identification for reduction of overvoltage transients," *Electric Power Applications, IEE Proceedings* -, vol. 150, no. 2, pp. 175–184, Mar. 2003, HF und LF model von Motor.

[96] O. A. Mohammed, S. Ganu, Z. Liu, N. Abed, and S. Liu, "High frequency modeling of permanent magnet synchronous motor drive," in *2007 IEEE International Electric Machines Drives Conference*, vol. 1, May 2007, pp. 318–321.

[97] S. Ogasawara and H. Akagi, "Modeling and damping of high-frequency leakage currents in PWM inverter-fed ac motor drive systems," *Industry Applications, IEEE Transactions on*, vol. 32, no. 5, pp. 1105–1114, Sep. 1996.

[98] N. Aoki, K. Satoh, and A. Nabae, "Damping circuit to suppress motor terminal overvoltage and ringing in pwm inverter-fed ac motor drive systems with long motor leads," *IEEE Transactions on Industry Applications*, vol. 35, no. 5, pp. 1014–1020, Sep. 1999.

[99] A. Hassan, S. Schulze, M. Al-Hamid, and R. Vick, "Prediction of the resonance effect of the common mode noise of smps," in *10th International Symposium on Electromagnetic Compatibility*, Sep. 2011, pp. 707–711.

[100] X. Pan, R. Ehrhard, and R. Vick, "An extended high frequency model of permanent magnet synchronous motors in hybrid vehicles," in *10th International Symposium on Electromagnetic Compatibility*, Sep. 2011, pp. 690–694.

[101] A. Domijan, D. Carkowski, and J. H. Johnson, "Nonsinusoidal electrical measurement accuracy in adjustable-speed motors and drives," *IEEE Transactions on Industry Applications*, vol. 34, no. 6, pp. 1225–1233, Nov. 1998.

[102] L. G. Durnte and P. K. Ghosh, "Active power measurement in nonsinusoidal environments," *IEEE Transactions on Power Systems*, vol. 15, no. 3, pp. 1142–1147, Aug. 2000.

[103] A. Marinov and V. Valchev, "Improved methodology for power loss measurements in power electronic switches using digital oscilloscope and matlab," in *Proceedings of 14th International Power Electronics and Motion Control Conference EPE-PEMC 2010*, Sep. 2010.

[104] S. Weier, M. A. Shafi, and R. McMahon, "Precision calorimetry for the accurate measurement of losses in power electronic devices," *IEEE Transactions on Industry Applications*, vol. 46, no. 1, pp. 278–284, Jan. 2010.

[105] W. Cao, G. M. Asher, X. Huang, H. Zhang, I. French, J. Zhang, and M. Short, "Calorimeters and techniques used for power loss measurements in electrical machines," *IEEE Instrumentation Measurement Magazine*, vol. 13, no. 6, pp. 26–33, Dec. 2010.

[106] F. Avallone, C. D. Capua, and C. Landi, "Measurement station performance optimization for testing on high efficiency variable speed drives," in *Quality Measurement: The Indispensable Bridge between Theory and Reality (No Measurements? No Science! Joint Conference - 1996: IEEE Instrumentation and Measurement Technology Conference and IMEKO Tec*, vol. 2, 1996, 1098–1103 vol.2.

[107] Y. Liu, L. Shi, and Y. Li, "Comparison analysis of loss calculation methods and measurement techniques in power electronics and motor systems," in *Electrical Machines and Systems (ICEMS), 2013 International Conference on*, Oct. 2013, pp. 530–534.

[108] D. Christen, U. Badstuebner, J. Biela, and J. Kolar, "Calorimetric power loss measurement for highly efficient converters," in *Power Electronics Conference (IPEC), 2010 International*, Jun. 2010, pp. 1438–1445.

[109] L. Aarniovuori, A. Kosonen, P. Sillanpää, and M. Niemelä, "High-power solar inverter efficiency measurements by calorimetric and electric methods," *IEEE Transactions on Power Electronics*, vol. 28, no. 6, pp. 2798–2805, Jun. 2013.

[110] D. Kuebrich, J. Goettle, and T. Duerbaum, "Power loss measurement based on transient temperature rise," in *2012 Twenty-Seventh Annual IEEE Applied Power Electronics Conference and Exposition (APEC)*, Feb. 2012, pp. 1797–1801.

[111] D. F. Frost and D. A. Howey, "High-speed peltier calorimeter for the calibration of high-bandwidth power measurement equipment," *IEEE Transactions on Instrumentation and Measurement*, vol. 65, no. 1, pp. 155–163, Jan. 2016.

[112] M. Schinkel, S. Weber, S. Guttowski, W. John, and H. Reichl, "Efficient HF modeling and model parameterization of induction machines for time and frequency domain simulations," in *Applied Power Electronics Conference and Exposition, 2006. APEC '06. Twenty-First Annual IEEE*, Mar. 2006, p. 6.

[113] K. Gulez and A. A. Adam, "High-frequency common-mode modeling of permanent magnet synchronous motors," *IEEE Transactions on Electromagnetic Compatibility*, vol. 50, no. 2, pp. 423–426, May 2008.

[114] T. Dhaene and D. de Zutter, “Selection of lumped element models for coupled lossy transmission lines,” *IEEE Transactions on Computer-Aided Design of Integrated Circuits and Systems*, vol. 11, no. 7, pp. 805–815, Jul. 1992.

[115] S.-P. Weber, A. Linde, E. Hoene, S. Guttowski, W. John, and H. Reichl, “Modellierung geschirmter Leistungskabel im Frequenzbereich der EMV,” German, *EMV 2006*, 2006.

[116] M. Marinescu, *Elektrische und magnetische Felder*, 3. Aufl. Springer, Berlin, Heidelberg, 2012.

[117] M. Heiss, “Berechnung von Leiterbahn-Induktivitäten,” *Elektronik*, no. 19, pp. 103–104, Sep. 1988.

[118] S. Schelkunoff, “The electromagnetic theory of coaxial transmission lines and cylindrical shields,” *Bell System Technical Journal, The*, vol. 13, no. 4, pp. 532–579, Oct. 1934.

[119] J. Benecke and S. Dickmann, “Inductive and capacitive couplings in dc motors with built-in damping chokes,” in *2006 17th International Zurich Symposium on Electromagnetic Compatibility*, Feb. 2006, pp. 69–72.

[120] *Technical information*, FS200R07A1E3, HybridPACK^{TM}1 module with Trenchstop/Fieldstop IGBT3 and Emitter Controlled 3 diode and NTC, Infineon, Nov. 2013.

[121] *Technical information*, FGA180N33ATD, 330V, 180A PDP Trench IGBT, Fairchild, Apr. 2008.

[122] F. Costa, C. Vollaire, and R. Meuret, “Modeling of conducted common mode perturbations in variable-speed drive systems,” *IEEE Transactions on Electromagnetic Compatibility*, vol. 47, no. 4, pp. 1012–1021, Nov. 2005.

[123] *ECE 324 regulation no. 100, rev. 2*, UN Vehicle Regulations, Aug. 2013.

[124] W. Mathis and A. Reibiger, *Theoretische Elektrotechnik*, 20 th. Springer, Berlin, Heidelberg, 2017.

[125] R. Langella and A. Testa, “The effects of integration intervals on recursive rms value and power measurement in nonsinusoidal conditions,” *Instrumentation and Measurement, IEEE Transactions on*, vol. 60, no. 9, pp. 3047–3057, Sep. 2011.

[126] O. Mohammed, S. Ganu, N. Abed, S. Liu, and Z. Liu, "High frequency pm synchronous motor model determined by fe analysis," *Magnetics, IEEE Transactions on*, vol. 42, no. 4, pp. 1291–1294, Apr. 2006.

[127] S. Bowes and Y.-S. Lai, "The relationship between space-vector modulation and regular-sampled PWM," *Industrial Electronics, IEEE Transactions on*, vol. 44, no. 5, pp. 670–679, Oct. 1997.

[128] H. S. Black, *Modulation Theory*. Cambridge, MA.: Literary Licensing, LLC, 2013, reprint of 1953.

[129] F. Jenni and D. Wüest, *Steuerverfahren für selbstgeführte Stromrichter*. vdf Hochschulverlag AG, 1995.

[130] *Brochure*, Precision Power Meter LMG95, ZES Zimmer.

[131] B. Voljc, M. Lindic, B. Pinter, M. Kokalj, Z. Svetik, and R. Lapuh, "Evaluation of a 100 a current shunt for the direct measurement of ac current," *Instrumentation and Measurement, IEEE Transactions on*, vol. 62, no. 6, pp. 1675–1680, Jun. 2013.

[132] A. V. den Bossche and D. Bozalakov, "Two channel high voltage differential probe for power electronics applications," in *2013 15th European Conference on Power Electronics and Applications (EPE)*, Sep. 2013, pp. 1–6.

[133] J. Lienhard IV and J. Lienhard V, *A Heat Transfer Textbook*, 4th. Cambridge, MA: Phlogiston Press, 2017, Version 2.11.

[134] *DIN EN ISO 6946:1996-11*, Building components - Thermal resistance and thermal transmittance - Calculation method, Nov. 1996.

[135] L. Fabbiano, N. Giaquinto, M. Savino, and G. Vacca, "On the worst case uncertainty and its evaluation," *Journal of Instrumentation*, vol. 11, no. 02, P02001, 2016.

[136] G. Gruber, "Gekoppelte Regelung zweier Synchronmaschinen mit Hilfe frei programmierbarer Umrichter," Master's thesis, Graz University of Technology, 2017.

[137] S. Paul and R. Paul, *Grundlagen der Elektrotechnik und Elektronik 3*. Springer Vieweg, Berlin, Heidelberg, 2017.

[138] H. Lutz and W. Wendt, *Taschenbuch der Regelungstechnik*, 10. Aufl. Europa-Lehrmittel, 2014.